

Anchoring of Dye Molecules on a Nickel Oxide Surface

-An Atomic Force Microscopy Study-

INAUGURALDISSERTATION

zur

Erlangung der Würde eines Doktors der Philosophie

vorgelegt der

Philosophisch-Naturwissenschaftlichen Fakultät

der Universität Basel

von

Sara Freund

aus Frankreich

Basel, 2019

Genehmigt von der Philosophisch-Naturwissenschaftlichen Fakultät
auf Antrag von:

Prof. Dr. Ernst Meyer
Prof. Dr. Sabine Maier

Basel, 18. September 2018

Prof. Dr. Martin Spiess, Dekan

“Through the Force, things you will see.”
Yoda – Star Wars Episode V: The Empire Strikes Back

To S. K., whose memory gave me,
so many times, the strength not to give up.

Abstract

THE properties of metal oxides, such as NiO, can be modified when functionalized with organic molecules. This kind of organic/inorganic interfaces are nowadays highly regarded, in particular, for the design of hybrid devices such as p-type dye sensitized solar cells (DSSCs). A key parameter for optimized interfaces relies not only in the choice of the compounds but also on their adsorption properties. The latter predicates fundamental studies of surface/molecules interactions at the nanoscale.

In this thesis, non-contact atomic force microscopy (nc-AFM) is first of all used at room temperature (RT) to investigate the surface of NiO(001). Following a well defined preparation process, atomically clean and flat surfaces are obtained. The adsorption of a set of different organic molecules, involving several deposition methods, on these surfaces is studied. The first strategy relies on thermal evaporation of molecules. Using this technique, two standard dye molecules, which are normally used for the design of n- and p-type DSSCs are compared. Kelvin probe force microscopy (KPFM) is used to quantify and observe the direction of the charge transfer between the metal oxide surface and the molecules, which appears to occur in opposite directions depending on the studied molecule. The second strategy used for functionalization is on-surface synthesis, where the dye molecules are assembled directly on the surface of NiO(001). RT nc-AFM as well as low temperature (LT) scanning tunnelling microscopy (STM)/AFM are used in order to follow this assembly process not only on NiO(001) but also on Au(111), highlighting that the reaction is surface independent. On both surfaces, the adsorption of the dye precursor, which occurs in a transoid geometry, as well as the formation of the corresponding metal complex, resulting in a cisoid conformation, are observed with submolecular resolution. The last sensitization strategy investigated in this work involves electro spray deposition (ESD). In order to test the good functioning of this method it is first applied to the well known C₆₀ organic molecule, resulting in interfaces that are not accessible via other preparation methods but fulfilling the cleanliness prerequisite of nc-AFM imaging. Finally, ESD is used to study three different dye molecules and their structure is resolved with submolecular accuracy.

Contents

Abstract	v
Introduction	1
1 Experimental Methods: Principles	5
1.1 Scanning Tunnelling Microscopy	5
1.2 Non-Contact Atomic Force Microscopy	6
1.2.1 Interaction forces	7
1.2.2 Multimodal AFM	10
1.2.3 Multipass AFM	11
1.2.4 Contact potential compensation	12
1.3 Kelvin Probe Force Microscopy	13
1.4 Summary	15
2 Experimental Methods: Realisation	17
2.1 The experimental set-up	17
2.1.1 The UHV system	17
2.1.2 The microscope	18
2.1.3 Measurement control	19
2.2 Cantilever preparation	21
2.3 Surface preparation	22
2.3.1 Preparation of NiO(001)	22
2.3.2 Preparation of Au(111)	23
2.4 Surface functionalization	23
2.4.1 Molecule evaporation	24
2.4.2 E-beam evaporation	25
2.4.3 Electrospray deposition	25
2.5 Summary	26
3 Introduction to Surfaces of Metal Oxides	29

Contents

3.1	Application fields of metal oxides	29
3.2	Preparing a clean metal oxide surface	30
3.2.1	State of the art	30
3.2.2	The case of NiO	31
3.3	Characterization of metal oxide surfaces by SPM	32
3.3.1	The surface of TiO ₂ (110)	32
3.3.2	The surface of MgO(001)	33
3.3.3	The surface of NiO(001)	34
3.4	Surfaces functionalization of metal oxides	35
3.4.1	Molecules and nanoparticles adsorbed on TiO ₂ (110)	35
3.4.2	Metal atoms deposited on MgO(001)	36
3.4.3	Functionalization of NiO(001)	37
3.5	Summary	38
4	Surface Characterization of NiO	39
4.1	Large scale imaging of the NiO surface	39
4.2	Atomic resolution on the surface of NiO(001)	40
4.3	Line defects	42
4.4	Summary	45
5	Comparing Standard n- and p-Type Dyes	47
5.1	Motivation	47
5.2	Interface morphologies imaged by nc-AFM	48
5.2.1	Cu-TCPP islands formed on NiO(001)	48
5.2.2	C343 islands formed on NiO(001)	52
5.3	Charge transfer direction studied by KPFM	55
5.4	Summary	57
6	Sensitization via On-Surface Synthesis	59
6.1	Motivation	59
6.2	On-surface synthesis on NiO(001)	60
6.2.1	Dye precursor anchoring on NiO(001)	60
6.2.2	Metal complex formation on NiO(001)	66
6.3	On-surface synthesis on Au(111)	67
6.3.1	Dye precursor anchoring on Au(111)	67
6.3.2	Metal complex formation on Au(111)	69
6.3.3	The role of Fe adatoms for the reaction	70
6.4	Summary	72
7	Functionalization through Spray Deposition	73
7.1	Motivation	73
7.2	C ₆₀ as a reference molecule	74
7.3	Complex dye molecules imaging	77
7.3.1	The reference P1 dye molecule	77
7.3.2	The prototypical Ruthenium dyes	79

7.4 Summary	81
Conclusion	83
Bibliography	87
Nomenclature	113
Acknowledgements	117
List of publications & communications	121
Curriculum Vitae	125

Introduction

THE question of energy conversion is a central topic in nowadays lives. In 2000, the global annual energy consumption was about 13 TW per year [1]. Considering the population growth and the increasing energy demand, one can expect this number to reach 28 TW in 2050 [2, 3]. Currently, 80% of the consumed energy is originating from fossil fuels [4], which has dramatical geopolitical and environmental consequences. Because the carbon based resources of our planet are limited, it is evident that this problem will lead to an even more tense worldwide situation in a near future, if nothing is done to find a renewable alternative to fossil energies. Given that the practical terrestrial global solar potential value has been estimated to be roughly 600 TW [1], solar power establishes itself as one of the most promising carbon-free solutions [5].

As for now, the best conventional silicon based solar cells are reported to have an efficiency lying around 22% [6]. However, the high production cost as well as the rather long energy payback time of this type of cells, is still limiting the popularization of this kind of technology. Dye sensitized solar cells (DSSCs), which were developed by O'Regan *et al.* as from 1991, are an encouraging option for the replacement of less cost effective devices. Indeed, using this type of hybrid solar cells, the production costs can be divided by six and the energy payback time by two [1]. On the other hand, nowadays, the best DSSCs deliver an efficiency of only about 11% [6], which is still far away for what can be achieved with silicon based solar cells, emphasizing that intensive research are still needed in this field in order to equal the performance of standard cells.

The principle of DSSCs, which is depicted in figure i.1a relies on a photoactive anode consisting in a n-type semiconductor TiO_2 sensitized with organic dye molecules. Once these molecules are adsorbed on the surface of the semiconductor, they can adsorb incoming photons leading to the excitation of electrons from their highest occupied molecular orbital (HOMO) to their lowest unoccupied molecular orbital (LUMO). From there, electrons are then injected in the conduction band (CB) of TiO_2 and can be collected in form of an electron current. The main problem of this kind

Introduction

of n-type cells, is that their conversion efficiency is restricted by a theoretical limit of 30% [7]. To overcome this issue, He *et al.* exposed the concept of tandem DSSCs [8,9], resulting in an increase up to 43% of the theoretical efficiency limit [7]. In essence, the idea behind this concept is to build a cell where both electrodes are photoactive. This can be achieved by coupling a standard n-type DSSC to a p-type cell, based on a photoactive cathode where the electron flow occurs in an opposite direction (see figure i.1b).

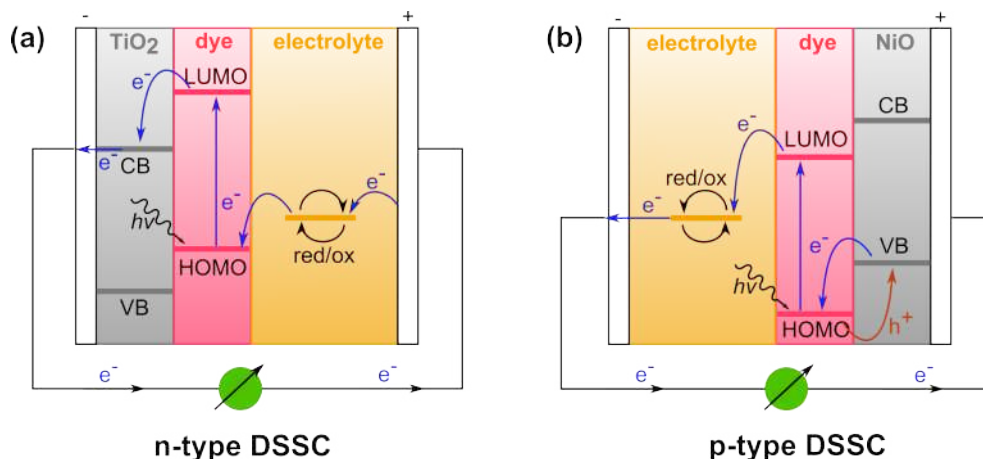


Figure i.1: Principle of DSSCs. *a*, n-type DSSC relying on a photoactive anode. *b*, p-type DSSC based on a photoactive cathode.

In the past years, several promising materials, such as Cu(I)-based delafossite compounds: CuMO_2 ($M = \text{Al, Ga or Cr}$), with p-type semiconductor properties have been intensively investigated [10–12]. Nonetheless, NiO is known to be the first reported wide band gap p-type metal oxide [13] and is therefore also the most studied material for the application in p-type DSSCs [14–16].

As for n-type cells, one of the key parameters for the proper functioning of optimized p-type devices is the adsorption configuration of the dye molecules on the surface of the semiconductor. However, contrary to TiO_2 /sensitizer interfaces that have been intensively investigated on the macro- as well as on the nanoscale [17–25], the anchoring of molecules on NiO surfaces have mainly been studied by fabrication of prototypical devices [26, 27]. Thus, there is a lack of information concerning the NiO/sensitizer interfaces at the level of single molecules.

Consequently, the following work focuses on the probing of these type of interfaces using non-contact atomic force microscopy (nc-AFM) in order to reach submolecular resolution. First the probing techniques, which were used for the realisation of this study are described from a theoretical- and experimental point of view. The historical background and the working principle of nc-AFM as well as several scanning modes are described in chapter 1, whereas the experimental set-up, materials and methods are exposed in chapter 2. Then, a brief introduction to comparable and related works also investigating the surfaces of metal oxides is given in chapter 3. The extensive application field relying on these kind of surfaces is discussed and different preparation strategies to obtain atomically flat and clean samples are reviewed. Additional to

NiO, the examples of TiO₂ and MgO are cited because of their common traits with the first material. TiO₂ due to its similar application field and MgO due to its structural resemblance with NiO. Characterization with atomic resolution as well as the functionalization of all three surfaces are discussed. In chapter 4 the surface of NiO(001) is imaged by nc-AFM at room temperature (RT). Different scanning modes are used in order to resolve the substrate with atomic scale accuracy. The defects present on the surface are also investigated and described. The three next chapters are then dedicated to the sensitization of NiO(001) with several organic molecules using different functionalization strategies. In chapter 5 a comparison between two standard dye molecules, that are designed for n- and p-type devices, respectively, is shown. Both molecules are deposited via thermal evaporation and their adsorption on NiO(001) is studied by nc-AFM and Kelvin probe force microscopy (KPFM). In chapter 6 sensitization via on-surface synthesis is discussed. There, the adsorption of a dye precursor as well as the formation of its corresponding metal complex is studied. Both are imaged with submolecular resolution and a major conformation change is observed upon metal coordination. Finally, in chapter 7, electro spray deposition (ESD) is used in order to prepare interfaces that are not accessible via other preparation methods. There, larger dye molecules are deposited on the surface of NiO(001) and their structure are resolved by nc-AFM.

Experimental Methods: Principles

THE investigation of functionalized metal oxides, and NiO in particular, at the nanoscale requires reliable investigation techniques that allow to resolve a large set of interfaces with atomic accuracy. This can be done by scanning probe microscopy (SPM) which is a field that gathers noninvasive probing techniques where a physical sensor is scanned over the surface of a sample. The development of this type of microscopy initiated a breakthrough in terms of resolution from 1983 when Binnig *et al.* imaged for the first time the atomic structure of the Si(111)-(7×7) [28]. SPM techniques, where single atoms can be imaged, are still considered nowadays as the most performing surface investigation methods regarding magnification scales. This chapter is dedicated to the presentation of different scanning probe techniques that are used in this work. Several scanning modes leading to the enhancement of the imaging resolution are described.

1.1 Scanning Tunnelling Microscopy

Since the invention of the first scanning tunnelling microscope (STM) by Binnig and Rohrer in 1981 [29], this technique has become an indispensable tool in the domain of surface science. STM was developed based on the quantum tunnelling effect which describes the property of an electron to tunnel through a potential barrier between two electrodes with a non-zero probability. This is implemented in STM where the potential barrier corresponds to the vacuum gap between the probing tip and the surface of the sample. After applying a bias voltage V_{BIAS} between the two electrodes and bringing them close enough together, the current starts to flow. This current I_t is exponentially dependent from the tip/sample distance. Thus the smaller the gap, the larger is the current. Therefore, the tip/sample distance can be regulated via a feedback loop in a way that the tunnelling current I_t is kept constant (see figure 1.1). This distance adjustment is recorded and converted into a topographic map of the studied surface. Consequently, because its principle entirely depends on the presence of current flow, the greatest limitation of STM, is that it can be performed only on electrically conductive samples.

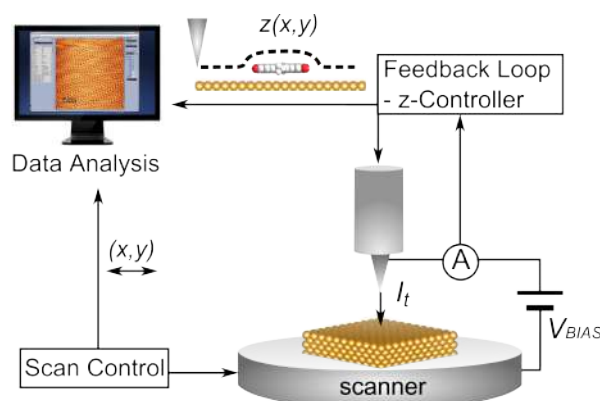


Figure 1.1: Schematic representation of a STM. *The current is kept constant via a feedback loop which consequently adjusts the tip sample distance. This is measured and converted into a topographic map of the surface of the sample.*

1.2 Non-Contact Atomic Force Microscopy

It is only from 1986 and the invention of the atomic force microscope (AFM) [30] that insulating materials could be investigated with the prospect of resolving their surface with the same accuracy than the one which could be reached on metallic samples. AFM is a mechanical based method guided by the principle of scanning the surface of a sample with a sensor which consists usually of a cantilever terminated with a sharp tip. As the tip is approached to the surface, the deflection of the cantilever is measured and converted, among others, into topographic information. AFM can be operated in different modes, where the interaction forces F_i between the tip and the sample are measured. The first mode, better known as contact mode consists of dragging the probe along the surface, whereas the dynamic mode is based on the controlled oscillation of the sensor, which can be done by means of two distinct modulation modes: amplitude modulation (AM-AFM) also called tapping mode or frequency modulation (FM-AFM) also known as non-contact AFM (nc-AFM).

The latter mode, which was introduced by Albrecht *et al.* in 1991 [31], and which is generally performed under ultrahigh vacuum (UHV) condition, is known to deliver high quality images with atomic resolution, and this starting from 1995 [32–34]. As already mentioned above, the working principle of this technique, which is sketched in figure 1.2a, relies on the measurement of the interaction forces between the tip and the surface. In essence, the cantilever is first of all excited at its eigenfrequency f_1 and the oscillation amplitude is set constant via a regulation loop. When the sensor is then brought closer to the surface, because of these interaction forces, the oscillation frequency shifts to another value f leading to a resonance change of the cantilever which can usually be measured by a laser beam that is reflected from the back of the probe into a four quadrants photo-diode detector (QPD). Comparably to what is described in section 1.1, in the nc-AFM mode, the tip/sample distance is adjusted via a feedback loop in a way that the frequency shift $\Delta f = f - f_1$ is kept constant resulting into topographic informations.

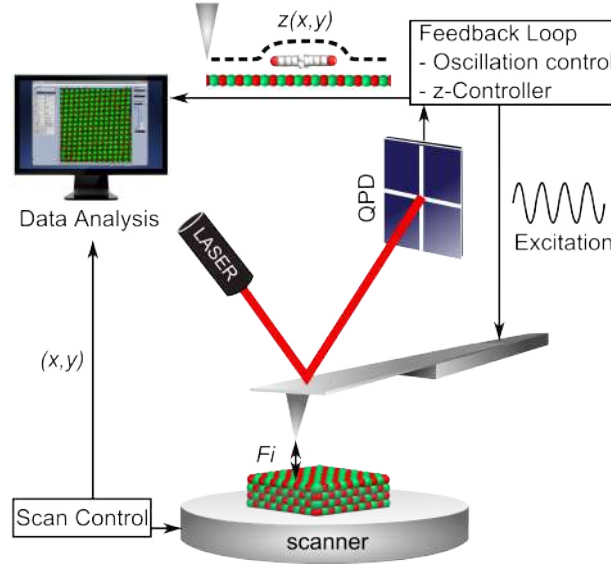


Figure 1.2: Schematic representation of a nc-AFM. In nc-AFM, the frequency shift Δf is kept constant via a feedback loop which consequently adjusts the tip sample distance. This is measured and converted into a topographic map of the sample surface.

1.2.1 Interaction forces

When the cantilever is oscillating at small amplitudes, the relation between the measured Δf and the interaction forces F_i experienced by the tip is given by [31]:

$$\Delta f(z) = -\frac{f_1}{2k} \frac{\partial F_i(z)}{\partial z} \quad (1.1)$$

where z is the separation distance between the tip and the sample, f_1 is the resonance frequency of the cantilever, k is its stiffness and $\partial F_i(z)/\partial z$ is the averaged force gradient over the tip oscillation cycle. Whereas this force gradient is considered as constant for small oscillations amplitudes ($A < 100$ pm), it can vary by several order of magnitude as the amplitude of the oscillation is increased. Thus a more general expression of the measured frequency shift is given by [35]:

$$\Delta f(z) = -\frac{f_1}{\pi k A} \int_1^{-1} F_i(z + A(1+u)) \left(\frac{u}{\sqrt{1-u^2}} \right) du \quad (1.2)$$

where $u/\sqrt{1-u^2}$ acts as a weight function describing the contribution of Δf with respect to the oscillation amplitude.

This expression 1.2 can be approximated by several methods [36–38], one of those being the one proposed by Sader and Jarvis [39], where the interaction forces between the tip and sample are described by:

$$F_i(d) = -\frac{2k}{f_1} \int_d^\infty \left(1 + \frac{A^{1/2}}{8\sqrt{\pi(z-d)}} - 1 + \frac{A^{3/2}}{\sqrt{2(z-d)}} \frac{\partial}{\partial z} \right) \Delta f(z) dz \quad (1.3)$$

where d is the closest tip/sample distance. This expression 1.3, therefore highlights that the sensed interaction forces strongly depend on the oscillation amplitude A of the sensor but also on the tip/sample distance z .

This can also be seen in figure 1.3 where the main interaction forces which can lead to a frequency shift of the cantilever are plotted with respect to z . It is worth to mention here that some interactions, such as magnetic forces, are not represented in this plot, because, in the frame of the present work, their contribution is thought to be negligible in comparison to the other forces that are described below.

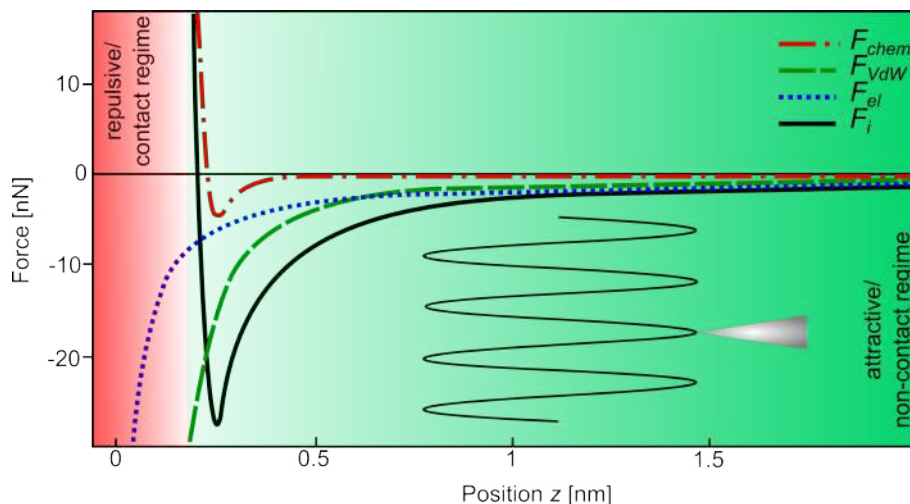


Figure 1.3: Interaction forces. Plot of typical interaction forces arising between tip and sample in function of the distance (z). The short range chemical forces, which are responsible for atomic resolution, are maximized in nc-AFM by adjusting the tip/sample distance as well as the oscillation amplitude of the tip.

As the cantilever is approached to a surface, it experiences a sum of forces (F_i) originating from short range chemical (F_{chem}) interactions, as well as long range forces such as electrostatic (F_{el}) and Van der Waals (F_{VdW}) interactions. Depending on the tip/sample separation distance, different forces are dominant and can consequently strongly influence the measurements. In figure 1.3 it is shown that, while the tip is approached to the surface, the cantilever experiences firstly attractive forces. This region (in green), where the slope of the representative curve of F_i is positive, is called the attractive or non-contact regime. Thus, when measuring nc-AFM, the tip is oscillating within this specific region.

In addition, molecular or atomic resolution, which is the ultimate aim of the nc-AFM mode, can in general, only be reached in a regime where short range forces, such as chemical forces, are dominantly sensed by the tip. Therefore, the long range force have to be minimized, which can be done by adjusting the distance between tip and sample. Indeed, as the tip is brought close to the sample, the cantilever is first dominantly sensitive to long range attractive forces such as Van der Waals or electrostatic interactions. Van der Waals forces, emerge from the fluctuation of the electron density when two atoms are brought close to each other. Assuming a spherical

1.2. Non-Contact Atomic Force Microscopy

tip with radius R in close vicinity z to a planar surface, the Van der Waals forces are given by [40–42]:

$$F_{VdW} = -A_H \frac{R}{6z} \quad (1.4)$$

where A_H is the Hamaker constant depending on the materials of tip and sample. On the other hand, electrostatic forces arise because, in general, tip and sample have different work functions (see section 1.2.4 for more details). Considering again a spherical tip over an infinite plane, both being conductive, the electrostatic forces are expressed as follows [43]:

$$F_{el} = -\pi\epsilon_0 \frac{R^2}{z(z+R)} V^2 \quad (1.5)$$

where ϵ_0 is the vacuum permittivity and V the potential difference between sample and tip.

From equations 1.4 and 1.5, it can be seen that both types of long range interactions depend on the tip radius R but are also inversely proportional (or quadratically inversely proportional) to the tip/sample distance. Consequently, long range contributions originating from these forces are less dominantly sensed when sharper tips are used, which is however difficult to control especially when measuring at room temperature (RT), or when the distance between the sample and the tip is decreased.

At smaller tip/sample separation short range forces are, consequently, dominantly sensed. These interactions consist of short range electrostatic forces, resulting from local charges or dipoles, and also chemical forces. The latter, arise when two atoms are separated only by few Angstroms [44]. In this case, the uppermost atom of the tip apex forms a temporary bond with the surface. The chemical interaction is generally associated to a Lenard–Jones potential, which depends on the bonding energy E_{bond} and the equilibrium distance σ , and is well described by [45]:

$$F_{chem,LJ} = -12 \frac{E_{bond}}{\sigma} \left[2 \left(\frac{\sigma}{z} \right)^7 - \left(\frac{\sigma}{z} \right)^{13} \right]. \quad (1.6)$$

However, in some cases, this interaction is better described by the exponential dependence of a Morse potential and the chemical force contribution is written:

$$F_{chem,Morse} = -E_{bond}(2e^{-\kappa(z-\sigma)} - e^{-2\kappa(z-\sigma)}) \quad (1.7)$$

where κ is the decay length of the bonding interaction.

When the tip/sample distance is further decreased, it is entering the repulsive or contact regime where the representative curve of F_i exhibits a negative slope (in red in figure 1.3). In this region, the detected forces are predominately repulsive, which is not desired when imaging in nc-AFM mode, because the measurement regulation is set for attractive forces, where the slope of the representative curve of F_i is positive. Thus, because the scanning cannot be regulated correctly in this region, it can lead to the fact that the tip enters violently in contact with the sample, resulting to the damaging of both of them, especially when the sensor is oscillating at large amplitudes.

In consequence, finding the optimum combination between tip/sample distance and oscillation amplitude is a fine adjustment undertaking.

In practice several methods were developed for minimization or compensation of long range forces and maximization of short range chemical interactions. These methods, which lead to the enhancement of the imaging contrast, can be applied in addition to nc-AFM measurements and are described below.

1.2.2 Multimodal AFM

Besides its eigen frequency f_1 , the cantilever can be excited to several oscillation modes which can be beneficial for the improvement of the imaging resolution. The most commonly used resonance modes are depicted in figures 1.4a–c.

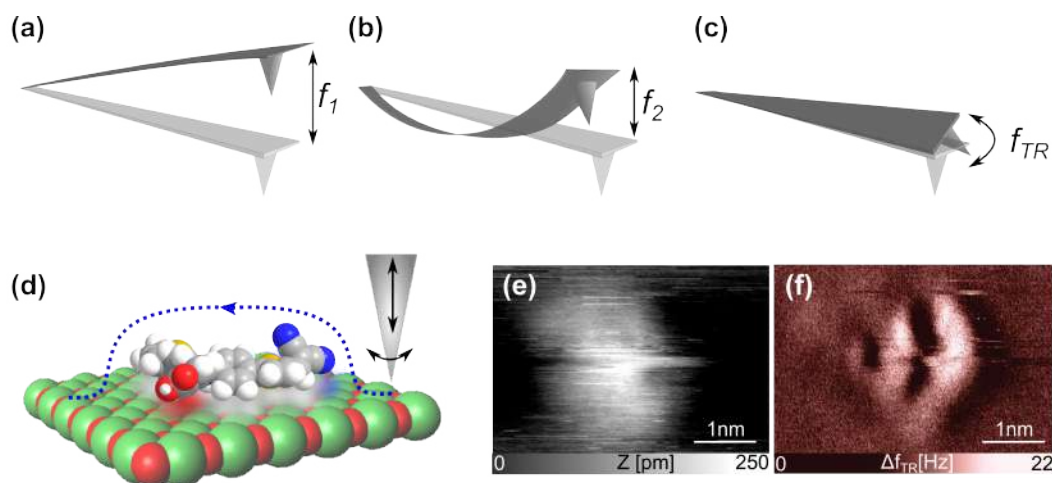


Figure 1.4: Oscillation modes and multimodal AFM. Several excitation resonances can be used in multimodal AFM. Among others: **a**, first normal (f_1); **b**, second normal (f_2) and **c**, first torsional (f_{TR}). **d**, Sketch of multimodal AFM using a normal flexural and torsional resonances in order to gain high resolution informations. **e**, Topographic image showing a single P1 dye molecule (see section 2.4.3) adsorbed on a surface. **f**, Δf_{TR} image of the same molecules, acquired simultaneously thanks to the torsional resonance, showing submolecular contrast. Scan parameters: $A_2 = 400$ pm, $A_{TR} = 80$ pm, $\Delta f_2 = -38$ Hz.

When the cantilever is excited to its second normal flexural mode ($f_2 \sim 6.28 \cdot f_1$) its stiffness is increased by about fourty times. This allows to excite the cantilever with lower oscillation amplitudes (typically between 400 and 800 pm). In other words, in comparison to the first normal mode (f_1) where the cantilever is excited at larger amplitudes (in a range that goes typically from 1 to 10 nm), the tip stays in average longer in close vicinity to the surface when it is excited to its second resonance. This allows to sense short range forces at slightly larger tip/sample distance, thus avoiding to enter the repulsive regime, resulting in more stable scan conditions [46, 47] and limiting the modification or the damaging of the tip and the sample [48].

In addition, the cantilever can be excited to several resonance modes at the same time. In this work, the excitation was limited to two simultaneous oscillations by the employed acquisition system, which is described in section 2.1.3. This superposition principle is called multimodal AFM (see figure 1.4d) and it offers the possibility to measure simultaneously different long and short range interaction forces [46, 47, 49, 50]. In this type of scanning mode, the cantilever can, for instance, be oscillated to one of its normal flexural modes, leading to topographic information, in addition to its first torsional resonance (f_{TR} in figure 1.4b) which is more sensitive to short range lateral forces. Because the oscillation amplitude of the torsional resonance is typically few tens of picometers, the measurement of its frequency shift Δf_{TR} depends directly on the local force gradient in the vertical direction. This can give access to submolecular contrast on samples where it is not possible while operating standard nc-AFM. It can be clearly seen when comparing figure 1.4e, where a single molecule is imaged with the second flexural resonance, and figure 1.4f showing submolecular contrast of the same molecule imaged with the first torsional mode. However, since the torsional mode is not a direct measurement of the topography but rather indicates the variations of the local force gradient in the vertical direction, it often results in contrasts that are difficult to interpret especially when scanning single molecules or molecular assemblies. Therefore this mode is usually used to resolve symmetric structures with a well defined periodicity, such as the atomic lattice of a crystal surface.

1.2.3 Multipass AFM

The so called multipass technique was recently introduced by Moreno *et al.* and successfully applied at temperatures up to 80 K where intramolecular bonds could be resolved [51]. This method also delivers satisfying results at RT, where submolecular resolution can be reached [52, 53]. The principle of multipass AFM is sketched in figure 1.5. In essence it consists of recording a first scan pass in a normal nc-AFM mode at a certain tip/sample distance in the attractive regime, *i.e.* while regulating this distance with a closed feedback loop which keeps Δf constant. A second scan line is then acquired with an open feedback loop following the topography recorded in the first pass and reducing the tip/sample distance by applying a constant z_{offset} . The fact that no regulation is applied to this second pass, contrary to normal nc-AFM mode, allows the tip to reach into the repulsive regime where the internal structure of a molecule can be imaged thanks to Pauli repulsion [54], without crashing. This is illustrated in figure 1.5b and 1.5c where a topographic image of a single molecule acquired at RT in the first scan line and the Δf_1 image of the same molecule, are presented, respectively. Comparing both images, emphasizes that the imaging contrast can be drastically enhanced when applying the multipass technique even at RT. In figure 1.5d, where second pass images are plotted with respect to the applied z_{offset} the passage of the tip from the attractive into the repulsive region can be seen. This is illustrated by a contrast inversion as the sensor is brought closer to the surface. In this specific example, a clear difference can already be noticed as the z_{offset} is reduced from -200 pm to -400 pm. A further resolution improvement is observed when the tip/sample distance is even further reduced.

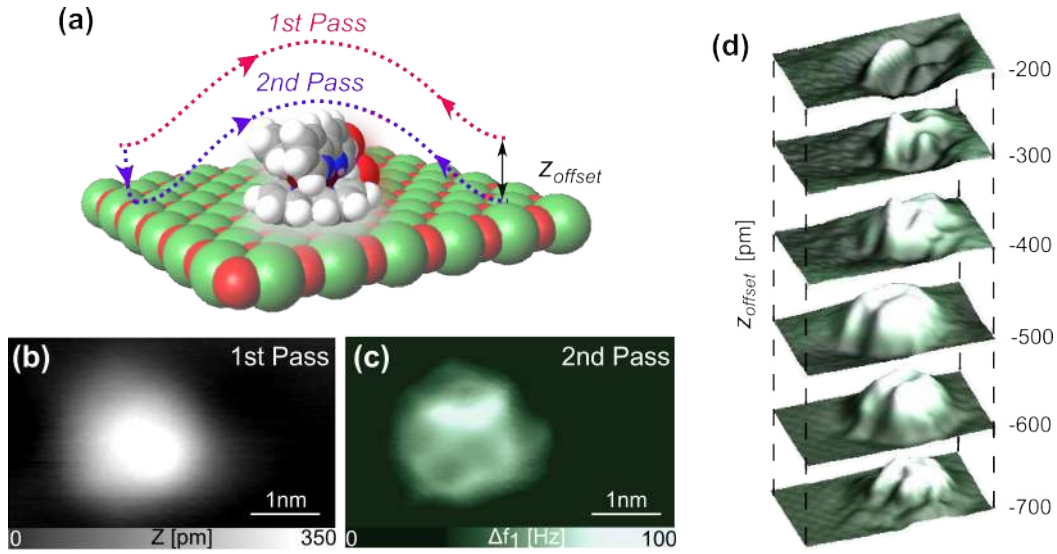


Figure 1.5: Multipass AFM. *a*, Sketch of multipass technique. *b*, Topographic image acquired in the first scan line showing a single ruthenium based dye molecule (see section 2.4.3) adsorbed on a surface. *c*, Δf_1 image of the same molecules, acquired in the second pass and applying a constant z_{offset} of -600 pm, showing submolecular contrast. *d*, 3D map showing the frequency shift images recorded in the second pass in function of the z_{offset} . Scan parameters: $A_1 = 4$ nm, $\Delta f_1 = -13$ Hz, $z_{offset} = -200$ to -600 pm.

1.2.4 Contact potential compensation

In contrast to Van der Waals forces, the electrostatic forces which arise between the tip and the sample can be compensated in nc-AFM. According to Lord Kelvin, this electrostatic interactions occur between two materials arranged in a capacitor geometry if they possess different work functions [55]. In the case of a tip and a sample spatially separated, this leads to the misalignment of their Fermi levels $E_{F,T}$ and $E_{F,S}$ (see figure 1.6a). In return, if the tip and the sample are electrically connected, their Fermi levels align resulting in the charging of both sides and therefore to the appearance of a contact potential difference (figure 1.6b):

$$V_{CPD} = \frac{1}{e} \Delta\Phi \quad (1.8)$$

where the difference in work functions is $\Delta\Phi = \Phi_S - \Phi_T$.

The resulting attractive force between both sides of the capacitor, which has already been described by equation 1.5 can also be written:

$$F_{el} = \frac{1}{2} \frac{\partial C}{\partial z} (V_{BIAS} - V_{CPD})^2 \quad (1.9)$$

and can therefore be compensated when an additional DC-voltage $V_{BIAS} = V_{CPD}$ is applied to the sample (figure 1.6c).

In practice, V_{CPD} is measured while recording the parabolic dependence of Δf via a bias sweep as the tip is oscillating over the surface. The maximum of this parabola

delivers the local CPD value which is measured at one specific spot of the surface. If this bias voltage is then applied to the tip/sample system the contribution of electrostatic forces can be minimized. Nevertheless, this implies that the CPD value should be equally distributed over the surface, which is most of the time not the case, especially if the sample consists of several materials, *e.g.* a single crystal functionalized with molecules. In that case, Kelvin probe force microscopy (KPFM), which is discussed in the section below, is the most appropriate technique for the compensation of electrostatic forces.

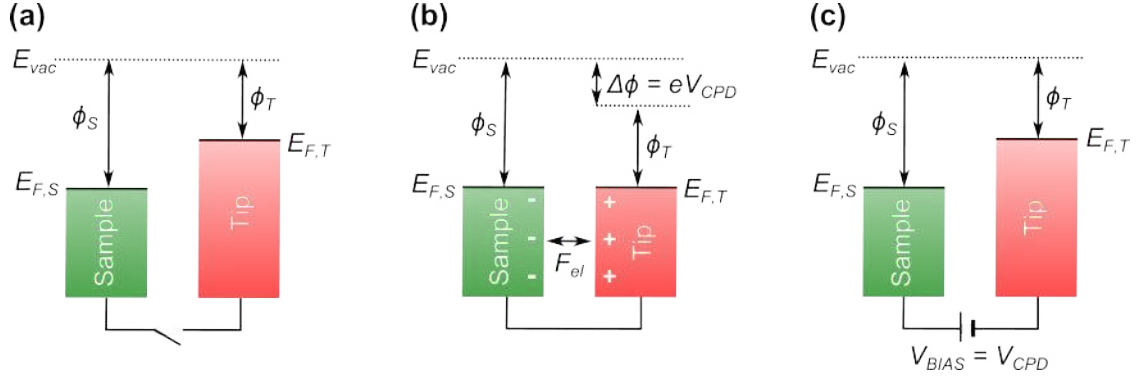


Figure 1.6: Contact potential difference. *a*, When two materials with different work functions are electrically disconnected, their Fermi levels are misaligned. *b*, They equalize after connection of both electrodes giving rise to an electric field between them. *c*, The latter can be compensated when a bias voltage ($V_{BIAS} = V_{CPD}$) is applied to the electrodes.

1.3 Kelvin Probe Force Microscopy

Kelvin probe force microscopy (KPFM), which was reported at the nanoscale level in 1991 [56,57], allows to measure the work function of a sample. The working principle of this technique relies on the same postulate which is used for the compensation of the local CPD, except that it is extended over the whole surface. Effectively, this can be done by modulating the force field between sample and tip by applying an additional AC-voltage $V_{AC}\cos(\omega t)$, where ω is the frequency of this AC-voltage. This results in an oscillating electrostatic interaction and consequently to cantilever excitation at a frequency ω . The expression 1.9 of the interaction forces between tip and sample then becomes:

$$F_{el} = \frac{1}{2} \frac{\partial C}{\partial z} [V_{DC} - V_{CPD} + V_{AC}\cos(\omega t)]^2 \quad (1.10)$$

Similarly to AFM, KPFM can be run in different modes, and the attractive forces F_{el} can be detected by two distinct lock-in techniques. In the amplitude modulation mode (AM-KPFM), the amplitude of the oscillation of the cantilever, is measured and set to zero via a feedback loop which compensates V_{CPD} by applying the adequate

V_{DC} [56]. This, consequently, results in a work function map of the sample where the contrast is given by the variation of V_{DC} . Using this method and setting ω so that it coincides with the second resonance of the cantilever, has the advantage that only very small AC-voltages are sufficient to trigger a reliable KPFM contrast [58].

Contrary to AM-KPFM, the principle of the frequency modulation mode (FM-KPFM), which is depicted in figure 1.7 relies on the force gradient rather than on force compensation [59–61]. Indeed, this method profits from the fact that, after application of additional low frequency AC bias ($\omega = 1$ kHz), the resulting oscillating electrostatic force gradient ends in a modulation of the frequency shift of the first resonance Δf_1 of the cantilever, leading to appearance of sidebands at $f_1 \pm \omega$. Therefore the oscillation at Δf_1 is tracked by a lock-in and the amplitude of this modulation is finally used in a Kelvin controller as a feedback value for the compensation of electrostatic forces. Consequently, this method gives access to a signal that is approximatively proportional to the force gradient rather than to the force itself. Hence the higher lateral sensitivity compared to the AM mode, because, contrary to the force, the force gradient is more confined to the tip apex [58].

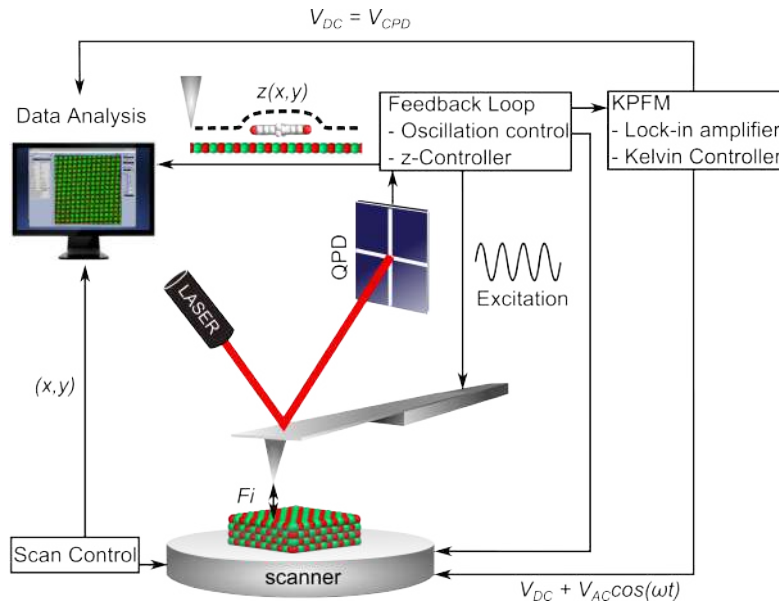


Figure 1.7: Schematic representation of an FM-KPFM. The amplitude of the modulated frequency shift Δf_1 , which is induced when an additional V_{AC} is applied, is used to adjust the value of V_{DC} to V_{CPD} , and therefore for the compensation of the electrostatic forces.

However, regardless from the mode in which it is operated, KPFM is sensitive to the local work function differences of an interface and can therefore also be used for the determination of dipole moments (p). Indeed, the latter can be determined if the molecular density, which can be deduced from high resolution imaging as well as the difference in dipole moment densities (Δp) are known. Δp can be calculated by the following formula [62, 63]:

$$\Delta p = \epsilon_0 \cdot \Delta V_{CPD} \quad (1.11)$$

where the average CPD difference ΔV_{CPD} can be easily deduced from the KPFM images. For instance, for the case of molecular islands formed on a surface, the average CPD difference ($\Delta V_{CPD} = V_{CPD,M} - V_{CPD,S}$) is measured as illustrated in Figure 1.8. This figure presents a topographic image of large molecular islands formed on the studied surface (figure 1.8a) and its corresponding KPFM image (figure 1.8b) which shows clearly that the CPD measured on the island ($V_{CPD,M}$) differs from the one measured on the bare substrate ($V_{CPD,S}$). By drawing two different masks on the topographic image; the first over the bare substrate (in orange in figure 1.8c) and the second over the molecular islands (in blue in figure 1.8e); and distributing these masks to the corresponding KPFM image (figure 1.8d and figure 1.8f), the average CPD can be measured on these specific areas. To avoid edge effects that can strongly influence the CPD, island edges and surface steps are excluded from the masks. To reduce the margin of error, this operation is then repeated on a set of several images. Because the absolute CPD is dependent on the work function of the tip, its value can slightly change from one image to another but the value of the CPD difference remains constant.

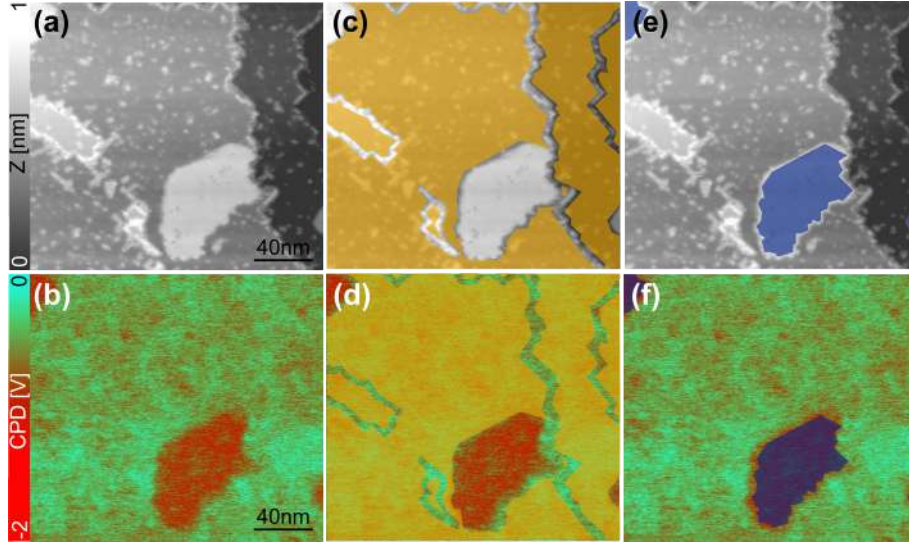


Figure 1.8: Average CPD difference determination. *a*, Topographic image of molecular islands formed on a surface and *b*, its corresponding KPFM image. A first mask (orange) is superimposed to the bare substrate in *c*, the topographic signal and distributed to *d*, the corresponding KPFM image. A second mask (blue) is drawn over the molecular island in *e*, the topographic image and *f*, the KPFM signal. Scan parameters: $A_1 = 4 \text{ nm}$, $\Delta f_1 = -13 \text{ Hz}$, $\omega = -900 \text{ Hz}$, $V_{AC} = -800 \text{ mV}$.

1.4 Summary

In this chapter the principle of SPM techniques that are used all along this thesis were discussed. It was shown that SPM methods are reliable, non invasive techniques to gain, among other, topographic informations of a surface down to the nanoscale.

Chapter 1. Experimental Methods: Principles

Atomic resolution can be reached as well with STM as with nc-AFM. Nevertheless, the latter presents the big advantage that it can be used on non conductive samples contrary to STM. A large set of different scanning modes, including multimodal AFM, multipass AFM as well as the compensation of surface potential, are available and often lead to the enhancement of the imaging contrast. The principle of KPFM was also discussed. This method can be applied to organic/inorganic interfaces for the visualization of their local work function variations or for the determination of dipole moments.

Experimental Methods: Realisation

THE following chapter is dedicated to the presentation of the experimental realisation of sample preparation and investigation. Because reaching atomic resolution is only possible under specific conditions, but more important, because the aim of this work is to study the adsorption of single molecules on atomically clean surfaces, all the experiments shown in this thesis are conducted in an ultrahigh vacuum (UHV) environment. The UHV system which was predominantly used for the present study is presented in the first part of this chapter. Second, the home build microscope operating at RT and the measurement control system which were used to investigate a large majority of the samples are discussed. Finally, the different preparation procedures for cantilevers and samples as well as the corresponding devices and materials are described.

2.1 The experimental set-up

2.1.1 The UHV system

All the samples that are described and discussed in the following work are prepared and investigated under UHV conditions. The UHV system is shown in figure 2.1. It consists of two distinct chambers that are separated with valves.

The samples and cantilevers are introduced into UHV via the load-lock chamber (blue in figure 2.1a) which is connected to a rotary pump and a large turbo pump allowing to reach a base pressure of 10^{-8} mbar. After pumping of the load-lock the sample can be transferred to the main chamber (orange in figure 2.1a) which is directly connected to the microscope located in the red chamber visible in figure 2.1a. The main chamber is pumped via an ionic pump and a titan sublimation pump in addition to the turbo pump that is also connected to the load-lock. This turbo pump can be isolated from the main chamber by a pneumatic valve while loading samples from air to the load-lock. The main chamber which has a base pressure of $\sim 10^{-10}$ mbar is also equipped with different preparation devices (green in figure 2.1a), including a heatable manipulator, a sputter gun, a quartz micro-balance (QMB), a knudsen cell, a cleaver

and an e-beam evaporator (see figure 2.1b), that can be used for the preparation of the samples. The different utilizations and the functions of these devices are described more in detail below.

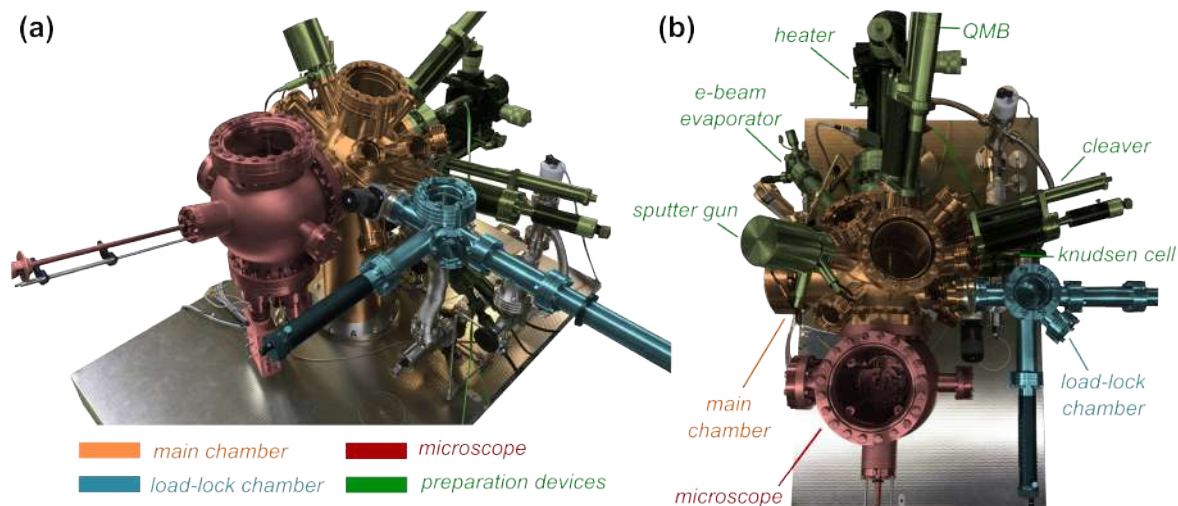


Figure 2.1: Experimental set-up. *a*, Side view of the UHV system. The main chamber (orange) is directly connected to the microscope (red) and to diverse preparation devices (green). *b*, Top view of the UHV system. A detailed insight of the different components is given.

2.1.2 The microscope

The microscope used in this study for the investigation of the vast majority of the samples is an home-build microscope operating at RT. It is the fourth generation of this type of microscope developed at the University of Basel [64].

This microscope, which is shown in figure 2.2, was mainly designed to operate in the nc-AFM mode with optical detection but can also be used as a STM. Nevertheless, in this work the use of the microscope was strictly restricted to its primary function and the STM images that are shown later were acquired with another device operating at low temperature (LT) that has been described in previous works [65, 66].

As for the RT nc-AFM microscope, it consists in a cantilever holder (red), a slider with a tube scanner and a sample holder (green) as well as an optical sensing block. The latter is composed of a fiber optics (blue), two orientable mirrors (violet) and a quadrant photo-diode (QPD) detector (orange) connected to an *in situ* current to voltage (I-V) converter with a large band width of 3 MHz.

After the light is generated by a superlum diode (SLD), with a wavelength of 678.5 nm, a current of 140.2 mA and a maximum light power of 2 mW, it is transferred to the microscope via the optical fiber. Thanks to a set of lenses and mirrors, the beam is first aligned and focused in the fiber optics and then reflected by the first mirror, that is located just below, to the backside of the cantilever. The position of the beam on the cantilever is adjusted by fine positioning of the mirror, which is done by

the means of piezo excitation, in a way that the focused light spot hits the cantilever with a maximal intensity. The light beam then travels to a second mirror where it is reflected to the QPD. Like for the first mirror, the position of the second mirror is adjusted so that the light beam is centred onto the photo-detector. In that way the deflection of the cantilever can be optimally detected while it oscillates and scans the surface of the sample. Indeed, the position of the light beam on the four quadrants of the photo-diode directly relies on the movements of the cantilever. After the light hits the detector, the motion of the beam is converted to four photo currents depending on its positioning on the four quadrants. These currents are then transformed in voltage signals which are treated by the electronics to generate a topographic mapping of the sample.

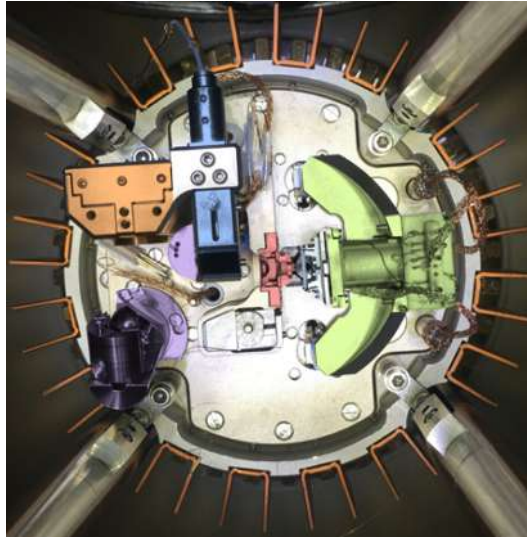


Figure 2.2: The microscope. *Top view of the UHV RT microscope wich consists of cantilever holder (red), slider with a tube scanner and sample holder (green), fiber optics (blue), two orientable mirrors (violet) and a quadrant photo-diode (QPD) detector (orange).*

2.1.3 Measurement control

The measurements are run by the means of a Nanonis RC4.5 electronics and the corresponding software (*SPECS Zurich GmbH*).

Figure 2.3a shows a diagram of the set-up when bimodal nc-AFM mode is used for the experiments. Here it can be seen that the cantilever is excited simultaneously to its first- or second flexural (f_1 or f_2) and torsional (f_{TR}) resonances via phase-locked loops (PLLs). Hence, offering the possibility to measure at the same time a topographic map and a torsional signal delivering additional information. To do so, the signal of the vertical deflection (y) detected by the QPD is transferred to a first PLL (PLL1). The measured frequency shift (Δf_1 or Δf_2) is fed to the z-controller where it is used to adjust the distance between the probe and the sample during the

Chapter 2. Experimental Methods: Realisation

approach and measurements, resulting in a topographic map (z) of the surface. In the meantime, the lateral signal (x) also coming from the QPD is fed into a second PLL (PLL2). Contrary to Δf_1 or Δf_2 which are required for the measurement control, the resulting frequency shift Δf_{TR} is only used for sensing.

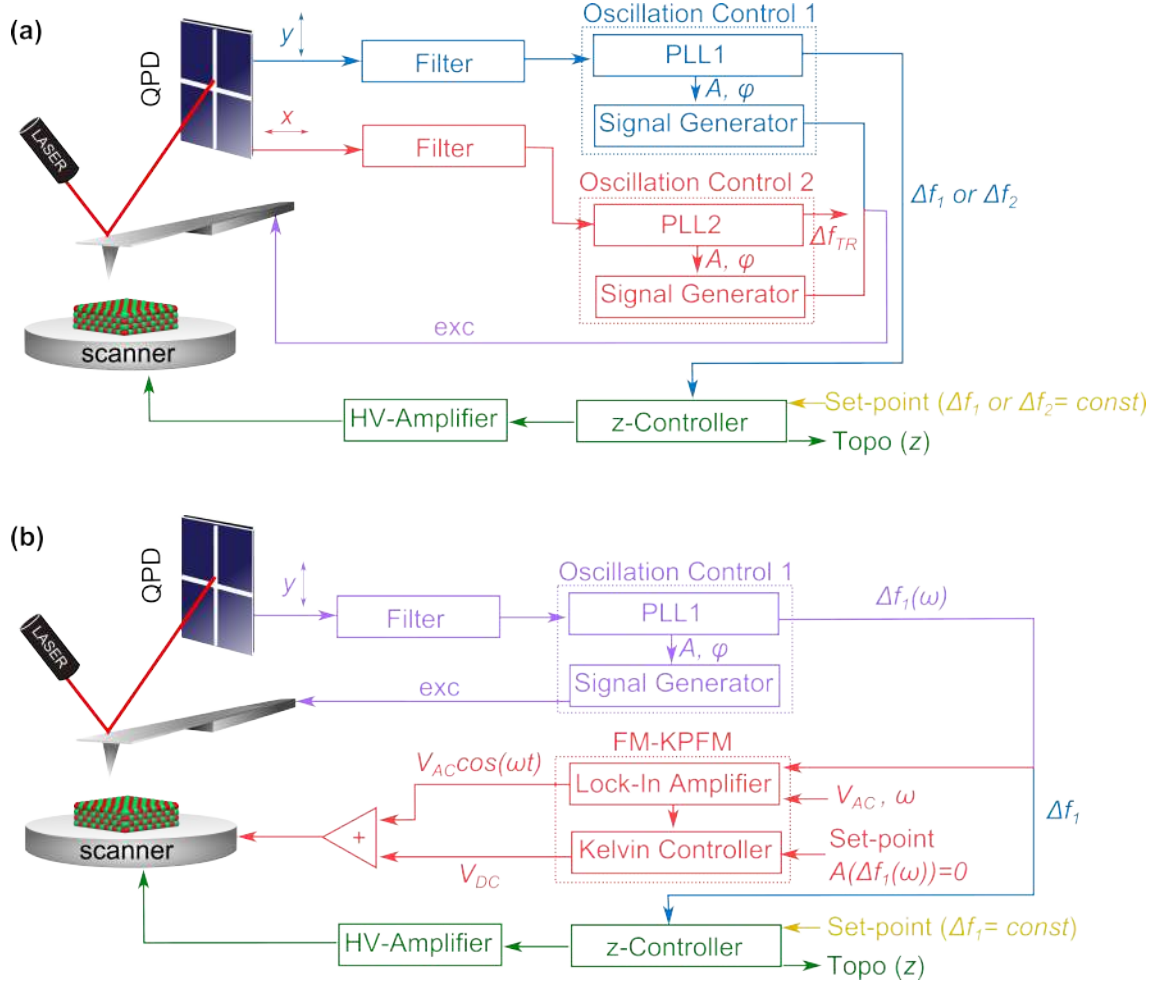


Figure 2.3: Measurement control. *a*, In bimodal nc-AFM mode, the unit oscillation control 1 is used to the measurement of topographic informations whereas the unit oscillation control 2 is used to acquire the torsional signal which delivers additional informations. *b*, in FM-KPFM mode, the Lock-In Amplifier is used to demodulate the oscillating Δf_1 signal, and the Kelvin controller is used to apply an additional DC voltage to the sample in order to minimize the modulation of Δf_1 .

Before the start of the measurement, the oscillation amplitudes A_1 or A_2 and A_{TR} , which are lying in the ranges of 4 – 9 nm, 400 – 800 pm and 40 – 80 pm, respectively, are calibrated. For the normal flexural modes, this is done by applying the constant γ procedure, where γ is the so called “normalized frequency shift” which directly depends on the oscillation amplitude A and the tip/sample distance z [40,67]. Because the torsional resonance results in the lateral- rather than normal excitation of the cantilever, the same method cannot be employed for the calibration of its oscillation.

Consequently the value of A_{TR} is calibrated so that the step edges appear sharp without any double tip features.

Figure 2.3b presents the set-up used for FM-KPFM measurements. In this mode the cantilever is excited mechanically via a PLL as it is done for standard nc-AFM but also electrostatically by application of an additional AC voltage (V_{AC}) to the sample. This voltage is typically lying in the range of 800 mV to 1 V with a low frequency ω of 250 Hz to 1 kHz. Application of V_{AC} leads to the oscillation of the frequency shift Δf_1 giving rise to a signal which is transferred into a Lock-In Amplifier where its amplitude is measured. The DC component of the total sample bias ($V_{DC} + V_{AC}\cos(\omega t)$) is then adjusted by the Kelvin Controller so that the modulation of Δf_1 is minimized.

2.2 Cantilever preparation

All the cantilevers used in this study were purchased from *Nanosensor GmbH*. They are standard non-contact Silicon cantilevers (PPP-NCL) with a spring constant k varying from 20 to 30 N·m⁻¹, a first eigenmode at $f_1 \sim 170$ kHz, a second resonance at $f_2 \sim 950$ kHz and a torsional resonance at $f_{TR} \sim 1.5$ MHz. Before they are introduced into vacuum, the cantilever chips (figure 2.4a) are glued with conductive two component epoxy glue (EPO-TEK H20S, *Epoxy Technology Inc.*) onto cantilever holders from *ScientaOmicron GmbH* and annealed in air about 1 h at 100°C. As shown in figure 2.4b, the glue is applied following a four-point-gluing technique which was proven to yield high Q -factors and thus to increase the sensitivity of the cantilever [68]. Values around 25k, 10k and 100k are measured for the Q -factors of the first, second and torsional resonance, respectively. After they are introduced to vacuum, cantilevers are outgassed 1 h at 120°C via the heatable manipulator of the main chamber to get rid of remaining contaminants. The native silicon oxide layer which is covering the tip, is removed through subsequent sputtering for 2 min at an energy of 1 keV under Argon pressure ($5 \cdot 10^{-5}$ mbar) [25].

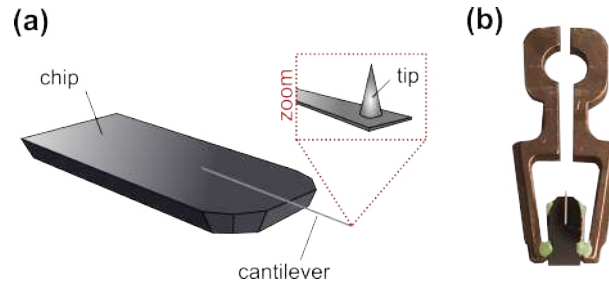


Figure 2.4: The cantilevers. *a*, Schematic representation of the cantilever chip showing that the cantilever is terminated by a sharp tip. *b*, The cantilever chip is fixed to a holder via the four-point-gluing technique, represented in green in the picture.

2.3 Surface preparation

2.3.1 Preparation of NiO(001)

Because the present study focuses on the sensitizing of NiO single crystals, the first task encountered during this thesis was to prepare clean NiO(001) surfaces in a reproducible way. Because cleavage of those specific crystals is known to be the most reliable method for the preparation of clean and atomically flat non-reconstructed stoichiometric surfaces (see section 3.2.2 in chapter 3), it was selected as method of choice for the preparation of our samples.

The NiO(001) single crystals used in this study, which are in the form of rectangular rods with the dimension of $2 \times 2 \times 7 \text{ mm}^3$ and the long axis in the [001] direction, were purchased from *SurfaceNet GmbH*. These crystals were mounted on a home build sample holder, which consist of two blocks of metals fixed onto a standard Omicron sample plate. The crystal rod is introduced into the dedicated slot of the first block and is then squeezed against the bottom of this slot thanks to the second block which can be tightly screwed into the first one (figure 2.5a). In that way, the crystal is strongly fixed, which is one of the first requirements for an efficient cleavage.

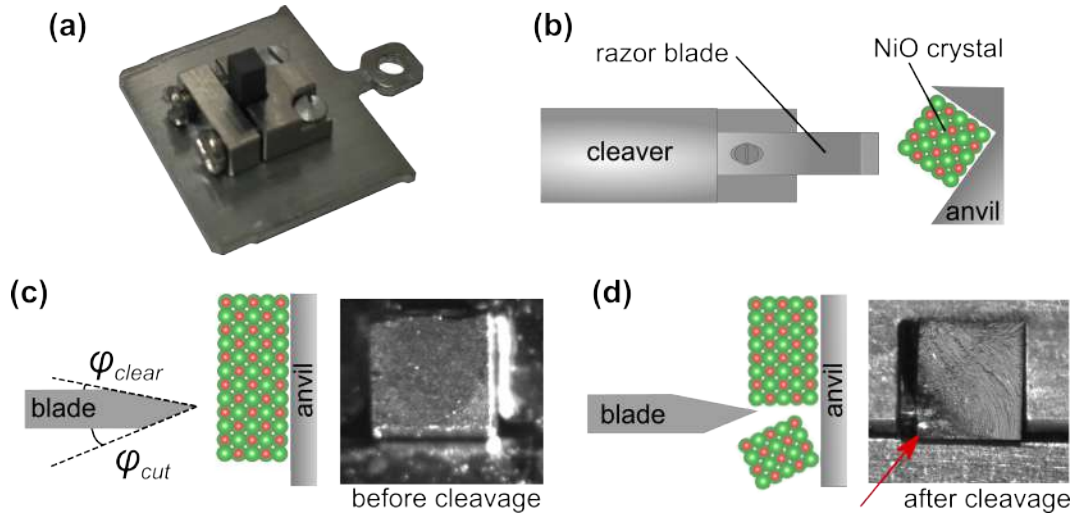


Figure 2.5: Cleaver set-up. *a*, NiO rod mounted in a home build sample holder. *b*, Top view of the NiO crystal position into the cleaver set-up. The sample is cleaved over the edge. *c–d*, Schematic side views showing the razor blade and the crystal before and after cleavage, respectively. The corresponding pictures of the NiO(001) surfaces are shown.

Because of the high reactivity of NiO, cleavage under ambient conditions is not possible, if atomically clean surfaces are desired. Therefore, once the crystal is mounted in its holder, it is introduced into UHV, where it can be cleaved *in situ*. However, prior to cleavage, the crystal is outgassed via an extended annealing step where the temperature is slowly increased from RT to 600°C. During this process, the pressure in the main chamber can be drastically increased (up to 10^{-7} mbar). Therefore high temperature is kept constant till the pressure drops to an acceptable level (in the range

of 10^{-9} mbar). Usually, the full process is setted to last roughly 5h. After the sample cooled down, it is inserted in the home-build cleaver, with the sample plate looking up whereas the crystal is pointing down, and is leaned against an anvil so that it is held firm during cleavage (figure 2.5b).

Figure 2.5b shows also that the sample is introduced in the cleaver with a certain angle with respect to the razor blade. In that way cleavage occurs over the edge of the sample, implying that the contact area of the blade and the crystal is reduced to one single spot leading to highly localized stress field which is known to facilitate cleaving, in particular for hard samples such as NiO [69, 70].

Cleavage is then initiated by fast motion of the spring-loaded blade which is mechanically crashed into the crystal edge. Figure 2.5c shows that the blade of the cleaver is designed with two distinct angles: the cutting angle (φ_{cut}) and the clearance angle (φ_{clear}) where $\varphi_{cut} > \varphi_{clear}$. These two angles are chosen so that the blade does not scratch the surface of the crystal and that the removed crystal piece falls down in a basket which is attached to the body of the cleaver.

Figures 2.5c and 2.5d present the surface of NiO crystal before and after cleavage, respectively. Before cleavage the surface appears to be pretty rough. After cleavage the edge where it occurred can be clearly recognized on the picture and is pointed with a red arrow. At this corner of the sample, the blade was literally crashed into the crystal leading to a strongly damaged area. Nevertheless, the rest of the surface is rather smooth and macroscopic step edges, indicating the presence of several flat crystal planes, can be seen.

Subsequently, to favour the discharge of the surface right after cleavage, the sample is annealed 1h at 500° .

2.3.2 Preparation of Au(111)

Even if the large majority of the experiments shown in this study are conducted on NiO(001) surfaces, some, which are discussed in chapter 6, are carried out on the surface of Au(111). The latter single crystal were purchased from *Mateck GmbH* and are cleaned by several sputtering and annealing cycles in UHV conditions.

2.4 Surface functionalization

In this work the functionalization of the NiO(001) surface with several organic molecules is presented. These molecules which are either dye precursors or dye molecules will be discussed in more details in their dedicated chapters. They are variable in size as well as in stability and can therefore not all be deposited onto the surface of NiO(001) by the means of the same methods. Figure 2.6 shows the different molecules in function of which deposition technique was employed for the preparation of their corresponding interfaces with NiO.

The molecules which are depicted in the red area were evaporated on the surface of NiO(001). The molecule that is presented in the green area, was obtained via on-surface metal-complexation of a sublimable molecule with iron atoms (Fe), which can

be evaporated from an e-beam evaporator. Because of their fragility, the molecules that are shown in the blue area could not be sublimated neither assembled on surface, but had to be sprayed directly from a solution to the surface. To finish, the C_{60} molecule that is shown in the violet area was both, sublimated similar to the molecules of the red area and also sprayed like the molecules of the blue zone. Among all this techniques, sublimation appears to be the cleanest method but presents the drawback that it can be applied to a limited class of molecules. On the other hand, spray delivers less clean surfaces, but presents the advantage that it can be used for the deposition of all kind of molecules.

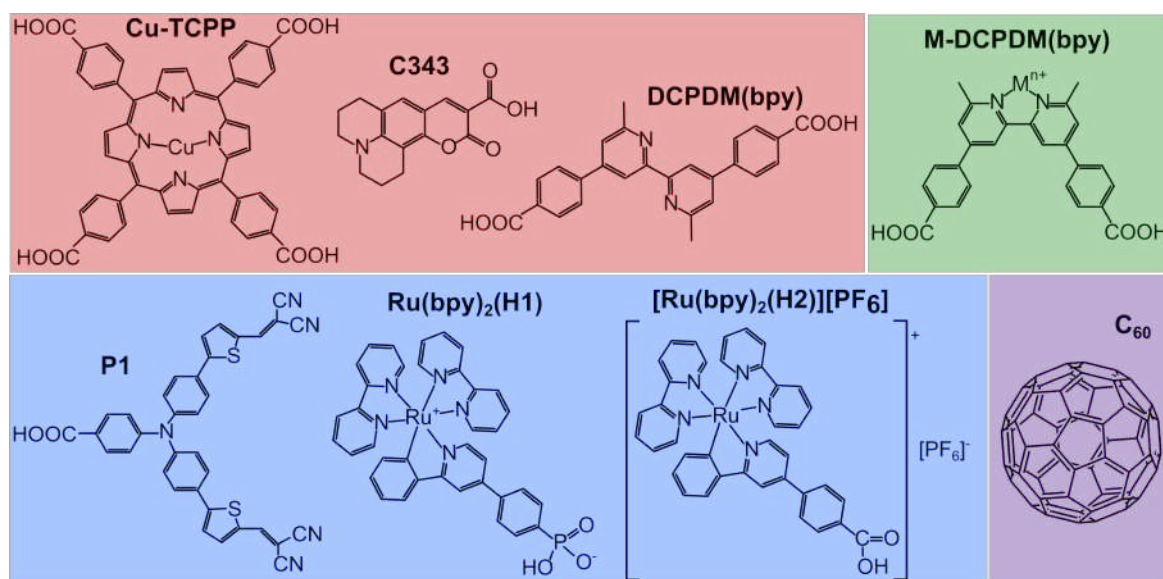


Figure 2.6: Dye precursor and dye molecules. *The molecules depicted in the red, blue and green areas were evaporated, synthesized on surface after metal evaporation or sprayed on the surface $NiO(001)$, respectively. C_{60} , which is represented in the violet area was evaporated as well as sprayed.*

2.4.1 Molecule evaporation

All the molecules discussed in this section are evaporated from a water cooled Knudsen cell. After small quantity of molecule's powder is filled into the metallic crucible of the cell, the evaporator is usually pumped over night before being introduced into the main chamber of the UHV system. The molecules are then outgassed by increasing slowly the temperature applied to the crucible while monitoring the deposition rate with a quartz micro balance (QMB). For a reliable deposition of the molecules, the rate is fixed to $0.5 \text{ \AA}/\text{min}$.

Cu-TCPP is a copper carboxyphenyl porphyrin dye with four anchoring groups (see chapter 5). The molecules were purchased from *Rare Chemicals GmbH*. They are evaporated at a temperature of 315°C for 5 min.

C343 is better known as Coumarin 343 (see chapter 5). These dye molecules were

purchased from *Sigma-Aldrich GmbH*. They are sublimated at a temperature of 150°C for 5 min.

DCPDM(bpy) is a dye precursor. It is the anchoring part of a larger dye molecule that has to be synthesized on surface (see chapter 6). This anchoring ligand that can supposedly bind to the surface through its carboxyphenyl acid groups was synthesised in the group of Prof. C.E. Housecroft and Prof. E.C. Constable from the University of Basel [71]. These molecules can be evaporated at a temperature of 255°C. Depending of the desired coverage, the deposition time is fixed to 10 s or 2 min.

C₆₀, which are also known as fullerene or Buckminsterfullerene (see chapter 7), are purchased from *Sigma-Aldrich GmbH*. They are sublimated at a temperature of 400°C for 5 min.

2.4.2 E-beam evaporation

Some molecules can not be evaporated. If this is the case, one solution is to synthesize them directly on surface. For instance, this technique is often used for the formation of metallo-complexes.

M-DCPDM(bpy) is one of those molecules which can be directly assembled on surface. It is composed of the molecule DCPDM(bpy) which is described above and an additional metal atom which is linked to the bipyridine unit of the anchoring ligand (see chapter 6). On the surface of NiO, this dye precursor is formed when Fe atoms are evaporated prior to DCPDM(bpy) evaporation. This is done using an e-beam evaporator, where high purity iron rod is heated up by electron bombardment to the point when atoms start to sublime. The iron rod was purchased from *Goodfellow GmbH*. After it is mounted in the dedicated slot of the e-beam evaporator, the latter is pumped over night before it is introduced in the main chamber. The evaporator is outgassed at a temperature close to sublimation for several hours while monitoring the pressure of the main chamber till it decreases to reach a level that is close to the base pressure of the chamber. The sublimation is then done for 40 s and controlled by the means of a flux monitor at a rate of about 0.1 monolayers(ML)/min.

2.4.3 Electrospray deposition

Because of their large sizes, and fragility, a large class of dye molecules can neither be evaporated, nor be synthesized on surfaces. To overcome this limitation, electrospray deposition (ESD) can be used. This technique, based on the electrospray ionization principle [72,73] and commonly used in biology, allows the functionalization of surfaces with large and complex dye molecules under UHV conditions with sufficient cleanliness to be compatible with nc-AFM measurements [74,75]. The ESD set-up is shown in figure 2.7. It is plugged to the UHV system, either directly onto a preparation chamber or, as shown on figure 2.7, to the load-lock to avoid contamination. A solution of molecules is first loaded in an automatically driven syringe connected to the emitter. By applying a bias voltage of roughly 2 kV to the latter, the solution is introduced to successive vacuum chambers via a capillary. These chambers are used as pumping stages to get rid of the solvent molecules before the molecular beam reaches the sample

which is kept under vacuum conditions. In order to get a homogeneous spray, the bias voltage is slightly adjusted during the deposition process and the pressure in the load-lock is around 10^{-7} mbar. The samples are then subsequently annealed up to 420 K, with the prospect of getting rid of traces of solvents.

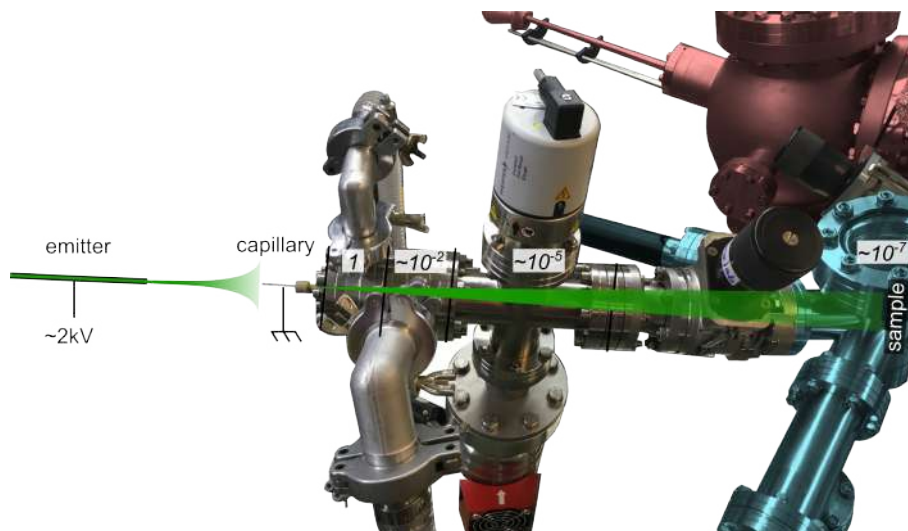


Figure 2.7: Electrospray set-up. A schematic drawing of the EDS set-up showing the different pumping stages is superimposed to a photograph of the devices mounted on the load-lock of the UHV system.

P1 is an organic dye possessing a carboxylic acid anchoring group (see chapter 7). A powder of these molecule was purchased from *Dyename AB* and dissolved in a solution of toluene and methanol with ratio (2:1) with a concentration of $0.2 \cdot 10^{-4}$ M. This solution is then sprayed for 1 h.

Ru(bpy)₂(H1) is a zwitterionic dye containing a phosphonic acid anchoring group (see chapter 7). It was synthesized in the group of Prof. C.E. Housecroft and Prof. E.C. Constable at the the University of Basel [76]. These molecules are dissolved in a solution of pure alcohol with a concentration of $0.5 \cdot 10^{-4}$ M and sprayed for 30 min.

[Ru(bpy)₂(H2)][PF₆] is a ruthenium based dye molecules with a carboxylic acid anchoring group (see chapter 7). Similar to **[Ru(bpy)₂(H1)]**, this sensitizer was synthesized following the procedure exposed in reference [76]. A solution of pure alcohol with molecular concentration of $0.3 \cdot 10^{-4}$ M was prepared and sprayed for 10 min.

C₆₀ are dissolved in a solution of toluene and methanol with ratio (4:1) and a concentration of $0.5 \cdot 10^{-4}$ M. This **C₆₀** solution is then spray for 10 min.

2.5 Summary

In this chapter it was emphasized that all the experiments conducted during this thesis were done under UHV conditions which is the first requirement if atomic resolution on the investigated sample is desired. The UHV system was described and it was shown that it is not only equipped with a microscope operating in nc-AFM mode and at RT,

but also with diverse tools that allow the preparation of reliable tips and clean samples. The microscope used in this study was developed and constructed at the University of Basel. Its working principle relies on the optical detection of a light beam that is reflected from the backside of the cantilever onto a photo detector. In that way the movements of the cantilever are converted to topographic images when scanned over the surface of the sample. These samples are previously prepared via divers procedures such as cleavage, annealing or sputtering. They are also sensitized with molecules through different deposition techniques like evaporation, metal-complexation or electrospray deposition.

Introduction to Surfaces of Metal Oxides

AMONG the class of metal oxides, NiO is only one example out of many. From the best insulators to superconductors; from inert to chemically active, this category of materials assumes interesting electronic and chemical but also magnetic as well as optical properties. Therefore, many well established but also emerging technologies, are based on this class of materials. Considering that the surfaces of metal oxides, or their interfaces with further materials, are usually the mainstay for the proper operation of the related devices, they lately became a key topic in the field of surface science. This chapter gives, therefore, a brief insight in the application fields, preparation, imaging as well as functionalization of metal oxide surfaces. The example of NiO is discussed and compared to other metal oxides such as TiO₂ or MgO, which present the same application field and structure like NiO, respectively.

3.1 Application fields of metal oxides

The growing interest of the scientific community and optoelectronic industry for the class of metal oxides finds its origin with the development of transparent conductive oxides (TCO). As its name suggests, this category of materials combines both properties, transparency and conductivity. Consequently, TCO became the cornerstone of many technological applications such as antistatic and optical coatings, flat as well as touch display panels, heaters, defroster, camera lenses and also solar cells [77–81]. Among TCOs, inorganic thin films based on indium tin oxide (ITO), fluorine doped tin oxide (FTO) or ZnO, are the most commonly used for photovoltaic applications. Indeed, because of their wide band gap n-type semiconductor character, and their related high charge injection efficiency, these materials are particularly suited for the design of solar cells [82–85].

On the other hand, some metal oxides, such as Fe₂O₃, TiO₂, SnO₂ *etc.*, are also known because they are promoters for heterogeneous catalysis and are, in consequence, also widely investigated and used in various chemical processes [86–88]. As part of those, the Fisher-Tropsch process for the production of synthetic fuels [89–91], as well as environmental applications, such as reduction of nitrogen oxide gases [92] or catalytic

oxidation of volatile organic compounds [93], which are contributing to deterioration of air quality [94,95]. In these processes, the heterogeneous catalysts are in a separated phase with respect to the reactants and have the capability to absorb gas or liquid molecules onto their surfaces. It has been shown, for example that, when deposited on a specific class of reducible metal oxide promoters, palladium, platinum and gold nanoparticles can decompose carbon monoxide [96]. In other words, metal oxides are not catalysts by themselves but can, however, promote the efficiency of the process. In essence, they act as a support which sustains the integrity of the nanoparticles and maintains them well separated [97]. It has also been demonstrated that few metal oxides are inert enough to protect metal surfaces or alloys from corrosion [98].

Consequently, considering this brought application field in addition to the fact that the surface of the metal oxides are often the key parameter for the design of optimized devices, it is easy to understand why this class of materials attracts such a great interest within the domain of surface science.

3.2 Preparing a clean metal oxide surface

Because they can present various stoichiometries and structural phases, metal oxide surfaces are, by nature, intricate materials. In their book, *The Surface Science of Metal Oxides* [99], Henrich and Cox commented: “The question of oxide preparation is central to all surface–science investigations, and herein lies what is possibly the greatest difficulty of all”, underlining the arduous character of the present task.

3.2.1 State of the art

Several methods, such as cleavage, oxidation or thin film growth, have been developed and successfully applied during the past decades for the preparation of the surfaces of metal oxides [99–102].

Among these strategies, UHV *in situ* cleavage was proven to be the most straightforward technique to prepare clean surfaces starting from single crystals. However, this method, which consists of cutting a crystallographic plane mechanically, can be applied only to certain materials, such as MgO, ZnO or NiO, with satisfactory outcomes [101]. When preparing oxides which are harder to cut, such as TiO₂, an alternative strategy is to first cleave and polish them *ex situ*, and then to expose them to several cycles of an *in situ* sputtering/annealing treatment under oxygen atmosphere, comparably to what is usually done for the preparation of metal surfaces. The advantage of the latter method compared to UHV *in situ* cleavage, is the creation of defects in the near surface region and in the bulk which supports conductivity, thus allowing the use of STM [99].

Metal oxide surfaces can also be prepared via ultrathin film growth on metallic samples. This strategy is of great interest especially when studying the structure of oxides which are known to be good insulators, such as MgO, SiO₂ or Al₂O₃. In that way, most of the experimental techniques, that require conductive samples, can also be applied to these specific materials. In addition, and contrary to cleavage,

thin film growth not only allows the preparation of non-polar surfaces, but also of polar samples [103]. However, compared to cleavage, the reliability of these methods is limited, essentially because the obtained surfaces can present several phases with different stoichiometries. Thus, in order to control the quality of the oxide film, three different strategies have been developed. The first one, which is also the simplest, consists into exposing a single crystal of metal to an oxygen flux. This technique can, for instance, be applied in order to obtain oxidized Cu surfaces [104–109]. However, oxidizing metals often results in strained samples due to the geometry of the metallic substrate. Indeed, the quality of oxide film mainly relies on the epitaxial matching of the latter to the lattice parameter of the metal. Therefore, to overcome this issue, a second method offers the possibility to grow oxide films on inert metal surfaces, via metal deposition and oxidation. In that way the substrate can be selected with the purpose of reducing the lattice mismatch between the metal and the oxide, resulting in better quality films where atomic resolution can be reached [110, 111]. The last strategy is the oxidation of alloy surfaces. The main advantage of this technique compared to the previous one, is that the inherent properties of the alloy can be beneficial for the preparation process of well ordered oxide layers. For instance, it has been demonstrated that the quality of Al_2O_3 films can be drastically improved through annealing treatments at 1300 K [112]. However, if the oxide layer is grown on an Al sample, such a high temperature handling would cause the melting of the substrate before achievement of a long-range ordered film. Therefore, Al_2O_3 thin films are usually grown on the alloy NiAl(110) [113, 114].

3.2.2 The case of NiO

In the case of NiO, which is a binary ionic crystal with a rock salt structure, two distinct surfaces with different crystallographic orientation and different properties are accessible: NiO(001) and NiO(111). Figure 3.1 gives a summary of all possible methods to prepare both surfaces, namely: cleavage of a single crystal, oxidation of a Ni sample and epitaxial growth of thin films on inert metallic samples.

The non-polar surface, NiO(001), which is exposed on the sides of the crystal, possesses a finite surface potential [115] and can therefore be prepared by cleavage of a NiO single crystal. This method results into clean NiO(001) surfaces where atomic resolution can be reached by means of different SPM techniques [116–124]. On contrary, oxidation of Ni(001) appears to deliver less uniform surfaces over large scales. Indeed, because of the large lattice mismatch (18%) between Ni and NiO [125], the oxide films appear to grow with a certain tilt with respect to the terraces of the metal sample [126], leading to the formation of small crystallites (size: 5 – 10 nm) [101]. However, the lattice misfit can be reduced by selecting an inert metal substrate with more appropriate geometry, where Ni can be evaporated under oxygen flux. For instance, when thin films are grown on Ag(001) samples, the epitaxial relation to the oxide film is improved and the lattice mismatch can be reduced to 3% [125], leading to a drastic improvement of the film quality [127].

In comparison to non-polar surfaces such as NiO(001), the polar surfaces are more difficult to prepare. Indeed, as the surface energy of the Ni-terminated (111) surface

diverges [128], it can consequently not be cleaved. Furthermore, since polar surfaces exhibit the tendency to facet rapidly while preparation processes [101], additional stabilization mechanisms are necessary when oxide films are grown on metallic substrates. Oxides films with high degree of surface order and hexagonal structure, corresponding to the $p(1 \times 1)$ NiO surface can be obtained when grown on Au(111) [129, 130]. A reconstruction to a $p(2 \times 2)$ structure can be induced through heat treatment. Similar surface morphology and reconstruction processes are observed for thin films grown on Ni(111). However, stable $p(1 \times 1)$ surfaces appear to be hydroxyl covered [131–133].

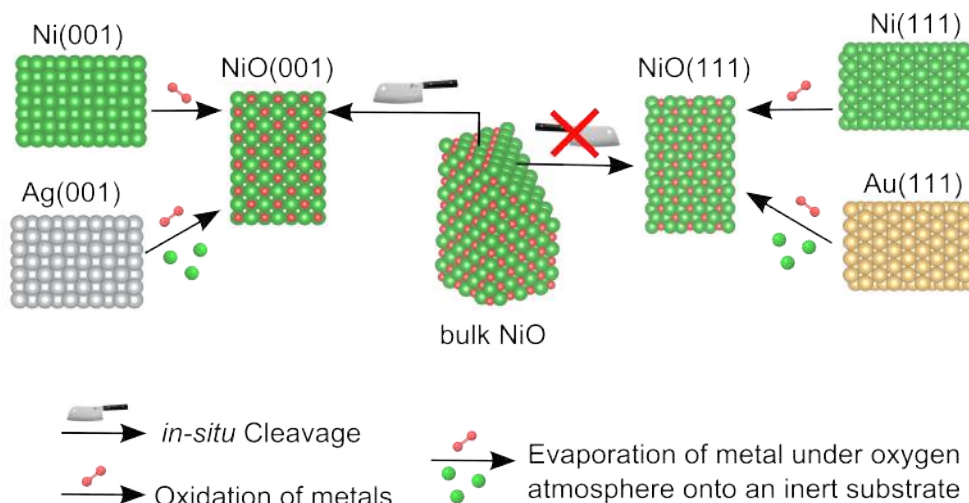


Figure 3.1: Preparation methods of NiO samples. *NiO(001) and NiO(111) surfaces can be prepared through several processes: cleavage, oxidation of nickel surfaces or thin films growth on other metallic samples.*

In conclusion, cleavage has been demonstrated to be the most reliable technique for the preparation of clean NiO surfaces. Therefore, in the following, the focus is put exclusively on single crystal samples and on the NiO(001) surfaces prepared through UHV *in situ* cleavage in particular.

3.3 Characterization of metal oxide surfaces by SPM

Since more than twenty years, SPM techniques, such as STM or nc-AFM have been intensively used to study the surfaces of numerous metal-oxides. Several samples have been imaged at large scale, but also resolved with atomic accuracy, providing a well documented catalogue of the physical and structural properties of the latter surfaces.

3.3.1 The surface of $\text{TiO}_2(110)$

To date, among the large class of metal oxides, some have been more exhaustively studied than others, leading to the publication of several detailed reviews. This is, for example, the case of the semiconductors ZnO [134], SnO_2 [135] and of course TiO_2 [136]. Because of its versatility and multiple potential applications (*e.g.* hybrid

3.3. Characterization of metal oxide surfaces by SPM

photovoltaics [137]), TiO_2 attracts particular interest. It crystallizes in three different structures where only two, the tetragonal rutile and anatase structures, are relevant for applications. Therefore, the (110) surface of TiO_2 (figure 3.2a) became, by far, the most studied metal oxide sample in the field of SPM [102,136]. Starting from the mid of the 90's, the atomic structure of this surface was resolved by STM [138,139] and nc-AFM [140] resulting in rows that could, actually, be attributed to Ti or O atoms in function of the polarity of the AFM tip only about ten years later [141], thanks to the careful study of defects and vacancies. Using a similar approach, Bechstein *et al.* highlighted, for the first time in 2009, an “all inclusive” contrast where both, Ti and O atoms, could be imaged simultaneously (see figure 3.2b) [142]. Besides O vacancies and H adatoms, which are the most common defects on the surface of $\text{TiO}_2(110)$, line defects were also observed. These defects, that are represented in figure 3.2c [143], were found to usually follow a step flow growth and were related as well to bulk impurities segregation [144] as to sample reduction [145,146]. These defects can also act as precursors for a (1×2) surface reconstruction [136].

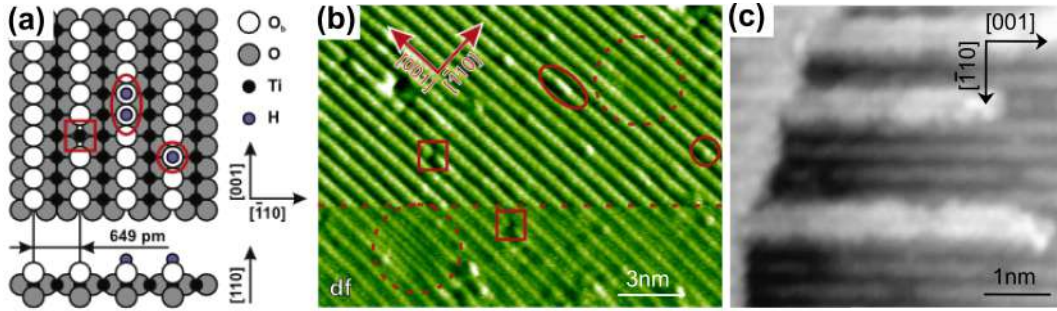


Figure 3.2: The surface of $\text{TiO}_2(110)$. *a*, Surface structure of $\text{TiO}_2(110)$ showing the dominant defects: O vacancies (red square), double and single OH (red ellipse and circle, respectively) – reproduced from [142]. *b*, nc-AFM detuning image showing the surface of $\text{TiO}_2(110)$, its surface atoms as well as its defects in classic (upper part) mode and ‘all inclusive’ mode (lower part)– adapted from [142]. *c*, STM image showing the structure of line defects growing from the upper terrace – adapted from [143].

3.3.2 The surface of $\text{MgO}(001)$

Because of its more simple structure and stable stoichiometry in comparison to TiO_2 or other metal oxides, the single crystal MgO , has also often been studied. This material presents a rock salt structure and is widely used as a basis for epitaxial growth of metals or for model catalysis [147–149]. When investigated by nc-AFM, it has been shown that the quality of imaging strongly depends on the quality of the cleavage [150,151]. The long range surface of $\text{MgO}(100)$ exhibits large terraces separated by steps which are dominantly oriented along the $\langle 001 \rangle$ crystallographic directions [148,152]. This is shown in figure 3.3a and 3.3b where it can be seen that long range steps consist of a succession of smaller step edges following the $\langle 001 \rangle$ directions [153]. Rectangular monoatomic indentations, which are running in the same directions as these step edges

(see figure 3.3a and 3.3c), as well as bright features corresponding to adatoms (see figure 3.3a and 3.3d) are frequently observed [150, 153]. The profile displayed in figure 3.3e attests that all these defects present a monoatomic height. Darker line defects, which are not shown here, corresponding to missing rows of Mg or O atoms can also be identified [150]. In addition, figure 3.3f shows that the atomic structure of MgO was resolved [153–155]. However, similar to other ionic crystals, only one type of atoms (either Mg or O) is imaged by the AFM tip [153].

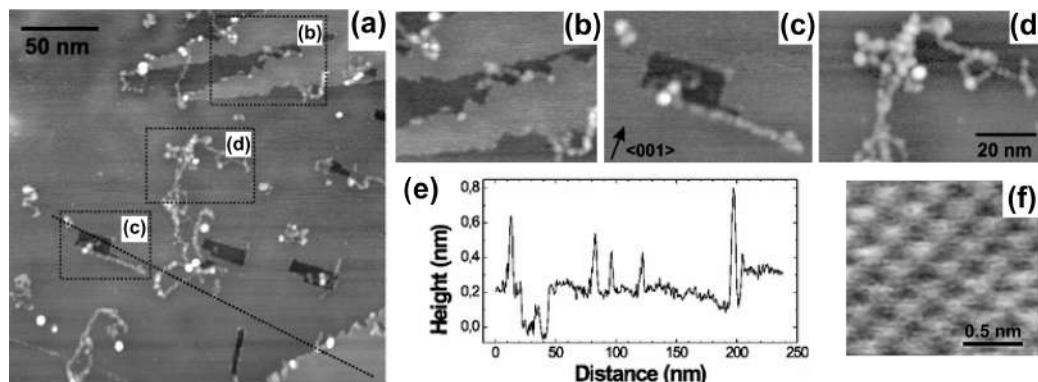


Figure 3.3: The surface of MgO(001). *a*, nc-AFM image of MgO showing the different types of defects: *b*, step edges; *c*, rectangular indentations as well as *d*, adatoms. *e*, profile recorded along the dark dotted line in *a*. *f*, Atomic resolution obtained on the surface of MgO – adapted from [153] and [155].

3.3.3 The surface of NiO(001)

Presenting the same rock-salt structure than MgO, with a lattice parameter of $a = 417$ pm, the (001) surface of a single NiO crystal can also be imaged by SPM. Comparably to TiO₂, NiO is known to be a semiconductor under some conditions. However, while the first is known to be n-type semiconductor, NiO is, on contrary, the first reported wide band gap p-type semiconductor [13]. Because of its larger band gap, in comparison to TiO₂, lying in a range between 3.5 eV and 4.3 eV according to previous studies [156–160], NiO is an insulator at RT, implying that STM can be used on this sample only when scanned at higher temperatures (~ 470 K) [116]. In addition, during the past twenty years, NiO has been the subject of few studies due to its magnetic properties which arise from the presence of unpaired electrons in the 3d shell of the Ni atoms, resulting in the fact that NiO is an antiferromagnet at RT. This is illustrated in figure 3.4a, where it can be seen that the spins are localized on the Ni atoms and are pointing in the $\langle 1\bar{2}1 \rangle$ directions. Considering the (001) plane, this leads to diagonals with parallel spin alignments in alternating directions. Contrary to other metal oxides, large scale topographic images are only rarely exposed in the literature, suggesting that clean sample over long ranges are particularly difficult to prepare. Figure 3.4b shows, to our knowledge, the one and only large scale image of a NiO(001) surface available in the literature [123], except of what was achieved

in the frame of the present PhD thesis [52, 161]. The surface displayed here exhibits large terraces separated by step edges. Few screw dislocations can also be identified as shown by the white arrow. In addition, atomic resolution has been reached on the surface of NiO (see inset of figure 3.4b) and comparably to MgO, only one type of atom could be imaged by the AFM tip [117–124]. However, contrary to the latter, where the nature of the imaged atom could not be determined so far, using several techniques, including defect investigation, tip functionalization or magnetic exchange force microscopy, bright protrusions were in general attributed to O atoms.

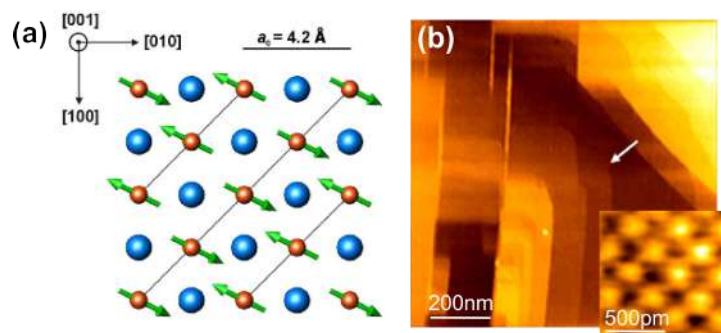


Figure 3.4: The surface of NiO(001). *a*, Surface structure of NiO(001) showing the spin alignment in opposite direction in neighbouring diagonal rows. *b*, Large scale nc-AFM image and atomic resolution acquired on a NiO(001) surface using a NiO tip – adapted from [123].

3.4 Surfaces functionalization of metal oxides

It has been mentioned in section 3.1 that numerous potential applications are based on metal oxides. Their surfaces, but even more often, their interfaces with other materials are the keystone of a proper functioning of the related devices. Therefore, functionalization of those surfaces with organic molecules or metal atoms, for instance, triggers great interest, also in the field of SPM.

3.4.1 Molecules and nanoparticles adsorbed on TiO₂(110)

Because the ability of TiO₂ to absorb light can be advanced when sensitized with specific organic molecules, these interfaces can be used for the development of hybrid photovoltaics [137]. Therefore, the functionalization of its (110) surface is one of the best studied among the class of metal oxides. Several organic molecules, have been deposited on its surface and their adsorptions have been studied [162–166]. In particular, the adsorption of several porphyrin molecules (3.5a shows the structures of three among others) has been intensively investigated by STM/AFM and it has been demonstrated that the presence or absence of anchoring groups in the structure of the molecule is playing a role for their stabilization on the surface. This results in the fact that some adsorb as single molecules whereas other can be observed only

when the coverage is increased leading to the formation of molecular islands (see figure 3.5b and 3.5c, respectively) [23]. Also, it has been observed that, independently of their metallic core, possible post deposition annealing treatment is influencing the anchoring geometry of porphyrins (see figure 3.5d and 3.5e) [22, 24, 25, 167].

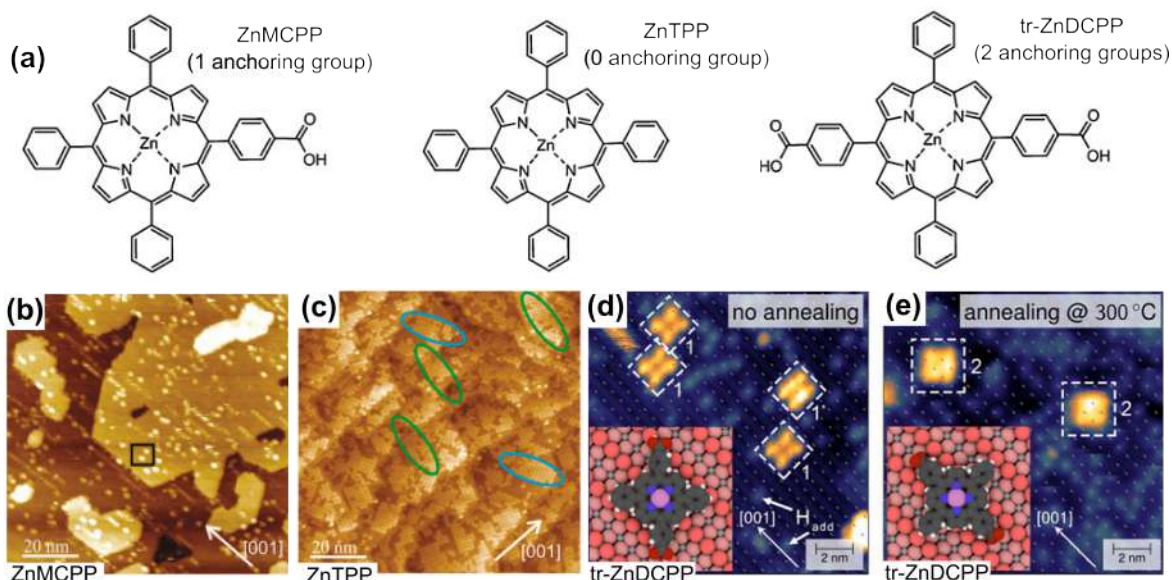


Figure 3.5: Porphyrin molecules adsorbed on TiO₂(110). *a*, Structure of different Zinc-porphyrins with: 1 (ZnMCP), 0 (ZnTPP) or 2 (tr-ZnDCPP) anchoring groups. *b*, large scale STM image, showing that ZnMCP adsorb as single molecules. *c*, large scale STM image, presenting the formation of ZnTPP islands. *d* and *e* are STM images highlighting the effect of annealing on the anchoring geometry of tr-ZnDCPP – adapted from [23] and [24].

On another hand, since it also represents a good promoter model for heterogeneous catalysis, the functionalized surface of TiO₂(110) with metallic nanoparticles has also been investigated by SPM [168–172]. There, it has been demonstrated that the surface termination as well as its oxidation or reduction states, strongly affects the size and distribution of metal clusters.

3.4.2 Metal atoms deposited on MgO(001)

Compared to TiO₂(110), the functionalization of MgO(001) single crystal surfaces has been more rarely investigated by SPM. However, similarly to the previous surface, a few studies are focusing on the adsorption of Pd atoms on the surface of MgO(001) [154, 173–175]. Being a model for supported metal catalysts, this interface is actually one of the most explored metal/oxide systems. Comparably to most of this type of systems, where the surface energy of the metal is higher than the one of the oxide [147], Pd exhibits a higher surface energy than MgO leading to a 3D growth type of the deposited metal, resulting in the formation of nanoclusters. The latter are shown in the topographic image displayed in figure 3.6a. They are formed of an

average of 7000 Pd atoms and appear to anchor on step edges as well as on points defects on terraces [149,154,173]. Also when imaged by KPFM, a clear contrast which corresponds perfectly to the topographic image can be observed (see figure 3.6b and profiles 3.6c and 3.6d).

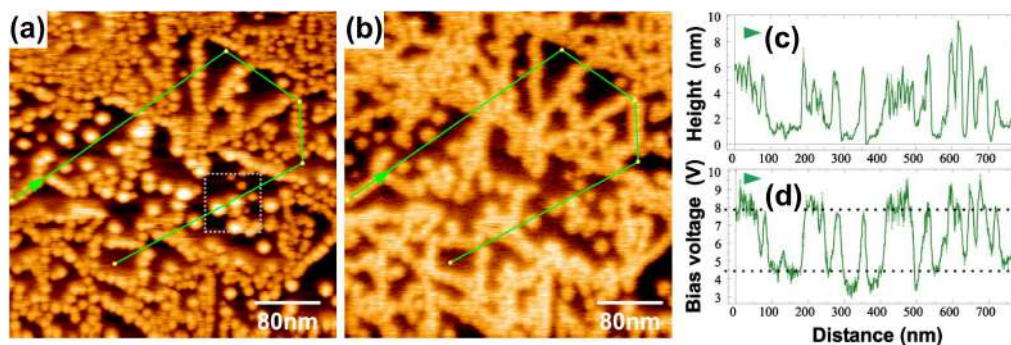


Figure 3.6: Palladium clusters formed on MgO(001). *a*, Topographic image showing the Pd clusters on the surface of MgO(001). *b*, Simultaneously recorded KPFM image. *c* and *d* are the corresponding profiles – reproduced from [154].

3.4.3 Functionalization of NiO(001)

Even though functionalized NiO(001) surfaces are known for their possible exploitation for the development of prototypical tandem DSSCs, this type of surfaces have extremely rarely been imaged by any SPM technique. Apart from the publications resulting from the present work [52,53,161], only one example dealing with the functionalization of single NiO crystals is reported in the literature [176]. In addition, this study, that has been conducted by Schwarz *et al.* in 2013, is related to the magnetic properties of NiO rather than to the fact that its ability to adsorb light can be enhanced when sensitized with some dye molecules, similar to TiO₂. Indeed, it focuses on the adsorption of the paramagnetic Co–Salen molecules on the surface of NiO(001). When deposited at low temperature (about 27 K), the Co–salen exhibit the tendency to adsorb as single molecules on the surface of NiO(001). Since the surface was resolved with atomic accuracy, the exact adsorption geometry of the molecules, with their Co atom on top of an O atom, could be determined (see figures 3.7a). In figure 3.7b the orientation of the molecules with respect to the crystallographic direction of the substrate are observed. It can be seen here, that the molecules are rotated clockwise or counter-clockwise by 4° away from the $\langle 110 \rangle$ directions. In addition, it has also been observed in this study that Co–salen molecules are occasionally displaced during the scanning process. The displacement happens stepwise from one adsorption site to another along the $\langle 110 \rangle$ directions, which corresponds to the lowest energy pathway for diffusion. Besides this, the growth mode of thin Co–salen films has been investigated. Increasing drastically the coverage and depositing the molecules on a surface kept at RT, results in a layer-by-layer step-flow growth implying relatively strong interactions between the substrate and the molecules.

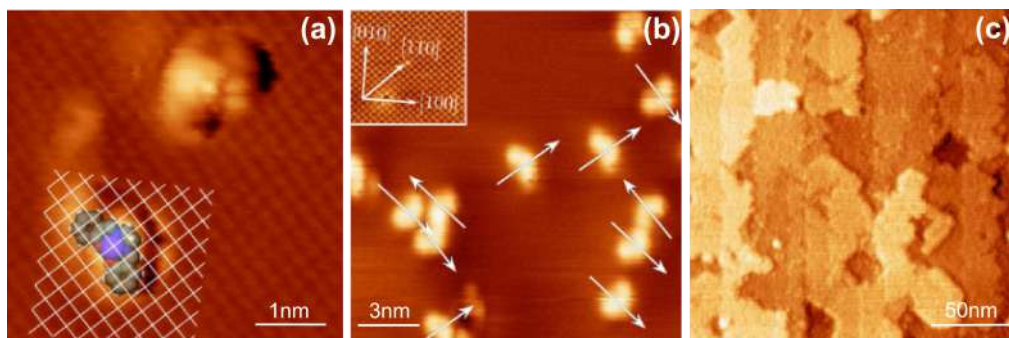


Figure 3.7: Co-Salen molecules adsorbed on NiO(001). *a*, nc-AFM image showing the adsorption geometry of the single molecule. *b*, nc-AFM image presenting the preferred orientation of the molecules which are rotated clockwise or counter-clockwise by 4° with respect to the $\langle 110 \rangle$ directions *a*, large scale nc-AFM image of the layer-by-layer step-flow growth of Co-salen on NiO(001). – adapted from [176].

3.5 Summary

In this chapter a brief overview of previous works focusing on the preparation, characterization and functionalization of metal oxides was given. In a first part, a short insight into the brought application field of this class of materials was exposed. Then, a second part was dedicated to the presentation of the different methods available for the preparation of clean metal oxide surfaces that are fulfilling the requirements to perform SPM measurements under UHV conditions. Among these techniques, one can cite: *in situ* cleavage, *ex situ* cleavage and polishing followed by several *in situ* sputtering/annealing cycles, metal oxidation as well as growth of oxide films on inert metals or alloys. However, it was discussed that *in situ* cleavage is the most reliable strategy for the preparation of clean surfaces starting from a single crystal NiO(001) sample. A third part was then focused on the characterization by STM of metal oxide surfaces, such as TiO_2 or MgO that present comparable properties or structure than NiO. There, what has already been achieved in terms of resolution on NiO(001) was briefly addressed. A last part highlighted the fact that an unequal amount of studies dedicated to the functionalization of several metal oxide surfaces are reported in the literature. A large set of organic molecules has already been investigated on the surface of $\text{TiO}_2(110)$ and the deposition of metal atoms on the same surface as well as on $\text{MgO}(001)$ has also been studied. As for NiO(001), putting aside the work that is presented in this thesis, only one example of molecules adsorbed on its surface is available in the literature. In conclusion, it was shown, that compared to other metal oxides, only a limited number of SPM studies are dedicated to the investigation of the surface of NiO in general, and to its functionalization in particular.

Surface Characterization of NiO

IN 1993, Satterley *et al.* reported NiO to be the first wide band gap p-type metal oxide [13], explaining why this metal oxide is the most studied material for the application in p-type DSSCs [14–16]. Also in the domain of surface science, NiO has been widely examined by numerous exploration techniques [103, 116–124, 129, 132, 133, 177–192]. However, because of its band gap which is lying in the range of 3.5 eV to 4.3 eV, according to previous studies [156–160], single NiO(001) crystals are non conductive at RT. For this reason, AFM is the one and only SPM technique which can be used to image this specific sample. Therefore, this chapter focuses on the investigation of the NiO(001) surface by nc-AFM at RT. Two types of surfaces with different morphologies are observed and resolved down to the atomic scale. The defects present on the surface are also studied and it is shown that their proportion and size can be tuned upon annealing.

4.1 Large scale imaging of the NiO surface

Figure 4.1a and 4.1b display a schematic representation of the rock salt structure of NiO(001). It can be seen in these images that the lattice constant of NiO is $a = 417$ pm and the step height is consequently $a/2 = 208.5$ pm. Figure 4.1c and 4.1d show topographic large scale images of two different NiO(001) surfaces both prepared following the process described in section 2.3.1 of chapter 2. Interestingly, both surfaces show completely different step morphology, for this reason, in the following, they are referred as type 1 and type 2 surfaces, respectively. The steps of the type 1 surface (figure 4.1c) are round shaped and do not follow any particular crystallographic orientation whereas the steps of the type 2 surface (figure 4.1d) are well ordered along the $\langle 110 \rangle$ directions of the surface. Interestingly, both step morphologies are rather unexpected. Because NiO presents the same crystallographic structure than MgO, similar step alignment along the $\langle 100 \rangle$ directions of the surface was anticipated [148, 152, 193]. Since the latter type of steps are exposing an alternating alignment of ions with opposite charges, they are neutral and thus, also energetically favourable. However, this is not the case of the edges observed in the present work. Indeed in the case of NiO, step edges, and

more particularly those which are running along the $\langle 110 \rangle$ directions of the surface, are polar. In other words, they are presumed to be energetically unstable, implying that some stabilization mechanisms are taking place at these sites. However, unlike other studies where stable polar step edges have been observed after functionalization with molecules [194,195], the stabilization process is, here, intrinsic to the metal oxide material. Therefore, it is thought that segregation of bulk impurities can lead to the observed polar step edges. This point is addressed in more details in section 4.3.

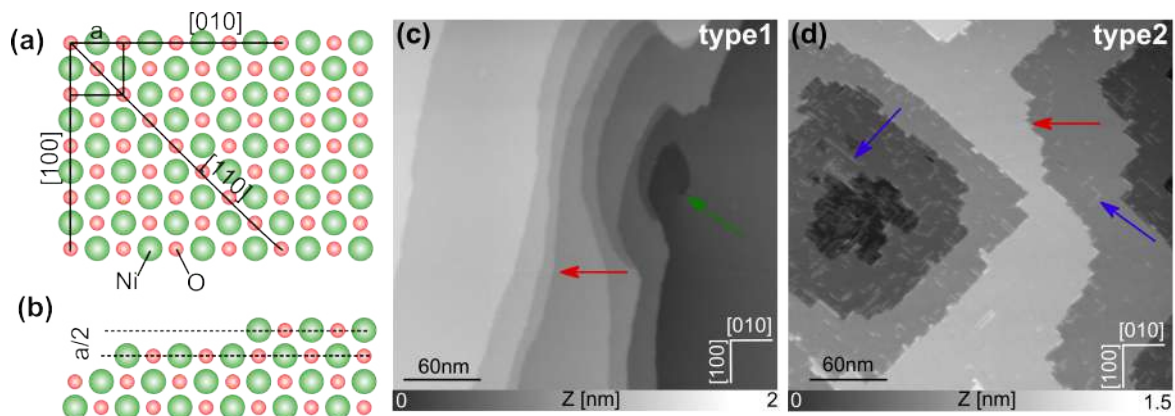


Figure 4.1: Large scale imaging of NiO(001). *a–b*, Crystallographic model of the NiO(001) surface. The lattice constant $a = 417$ pm and the step height is $a/2 = 208.5$ pm. *c–d*, Large scale topographic images of NiO(001) prepared following the process described in section 2.3.1. Two types of surfaces corresponding to crystals originating from two different batches are observed. Step height is measured to be ~ 210 pm for both types of sample. Depending on the surface type, defects with different shapes are observed. Scan parameters: **a**: $A_{f_1} = 5$ nm, $\Delta f_1 = -4$ Hz. **b**: $A_{f_1} = 5$ nm, $\Delta f_1 = -9$ Hz.

Type 1 surfaces are more rarely observed than type 2 (30% and 70%, respectively). In addition, more than 50 NiO crystals coming from three different batches were used for this work and surprisingly, all the crystals originating from the first batch were presenting type 1 surfaces, while the crystals from batches 2 and 3 appear to deliver type 2 surfaces. Type 1 is defect free except for a screw dislocation, which is pointed by the green arrow in figure 4.1c. This kind of defect has already been observed on NiO by Schmid *et al.* in a previous work [123]. On contrary, type 2 surfaces present quite a few line defects that are oriented in the same direction than the step edges (blue arrows in figure 4.1d). This point is discussed in section 4.3. Nevertheless, both types of surfaces present large terraces separated by steps which are roughly 210 pm in height corresponding to mono-atomic steps (red arrows).

4.2 Atomic resolution on the surface of NiO(001)

Figure 4.2 shows that atomic resolution can also be reached on both type of surfaces with several techniques. Figure 4.2a is a topographic image recorded on a type 1 sur-

4.2. Atomic resolution on the surface of NiO(001)

face. This image was obtained using the first oscillation mode (f_1) of the cantilever and presents the atomic rows of a type 1 surface oriented along the $[110]$ crystallographic direction of the sample. Figure 4.2b, which shows the single atoms of a type 2 surface, was obtained by applying the multipass technique. The frequency shift image displayed here was recorded during the second line scan applying an z_{offset} of -600 pm. The contrast can further be improved when the frequency shift image of the torsional oscillation mode (f_{TR}) is acquired while the tip/sample distance is regulated using a constant frequency shift (Δf_1). Indeed the image shown in figure 4.2c reveals a regular cubic pattern formed by bright protrusions which can unambiguously be attributed to single atoms of a type 1 surface.

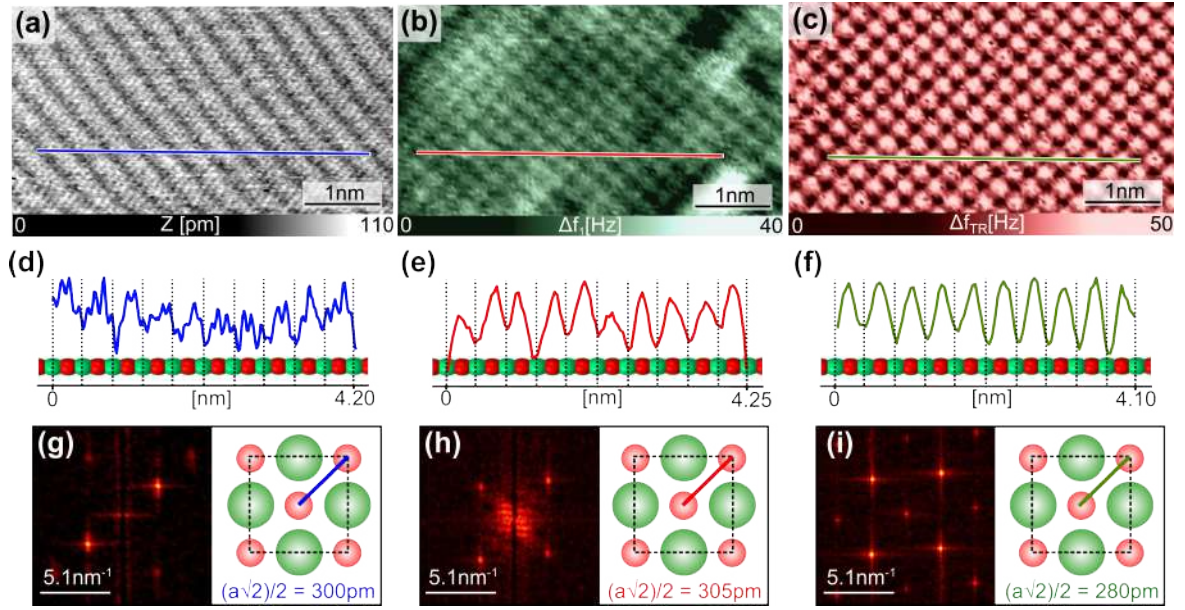


Figure 4.2: Atomic resolution on NiO(001). Atomic resolution can be reached employing several techniques. **a**, Topographic image showing the atomic rows of the NiO(001) type 1 surface. Single atoms of the type 2 surface can be seen in **b**, a frequency shift image recorded in the second scanning pass with an offset of -600 pm while the tip/sample distance is regulated in a first pass applying a constant Δf_1 . **c**, the same kind of contrast, revealing the single atoms, is obtained on a type 1 surface using the torsional mode. **d–f**, Corresponding profiles recorded along the lines drawn in the previous images, showing that only one type of atom is visible. **g–i**, Fast Fourier transforms (FFTs) acquired in **a–c** showing cubic packing of the crystal. The measured distances between two nearest neighbour atoms of the same type is fitting to the expected value : $a\sqrt{2}/2 = 295$ pm. Scan parameters: **a**: $A_1 = 4.3$ nm, $\Delta f_1 = -310$ Hz. **b**: $A_1 = 4$ nm, $\Delta f_1 = -42$ Hz $z_{offset} = -600$ pm. **c**: $A_1 = 7$ nm, $A_{TR} = 80$ pm, $\Delta f_1 = -79$ Hz

All the profiles recorded along the lines drawn in the previous mentioned images, point that the distance between two protrusions is $\sim 420 \pm 10$ pm (figures 4.2d–f), which corresponds to the lattice parameter of NiO ($a = 417$ pm). This implies that, for both types of surfaces, only every second atom is visible, similar to what is observed

for ionic crystals [196] or other metal oxides [196]. The fast Fourier transforms (FFTs) shown in figures 4.2g–4.2i are recorded on images 4.2a–4.2c, respectively. These FFTs all show, with more or less intensity, a cubic pattern supporting the mesh geometries of the rock salt structure of NiO. Figures 4.2g–4.2i highlight the fact that the distance between two nearest neighbour atoms of the same type is $\sim 290 \pm 15$ pm which fits to the theoretical value of $(a\sqrt{2})/2 = 295$ pm.

Because the imaging contrast is directed by the uncontrollable termination of the AFM tip apex at RT, attributing the bright protrusions of figures 4.2d–f to a specific type of atom and, as a consequence, determining if either Ni or O atoms are imaged is not an obvious task. Nevertheless, assuming that Ni vacancies appear more often at the surface of NiO [99], and taking into account that no atomic defects have been observed, there are two possible interpretations: either the bright protrusions are corresponding to Ni atoms and all the images were recorded on defect free areas, or the protrusions are related to O atoms resulting in the fact that Ni vacancies are simply not visible. However, earlier related works generally attribute the bright protrusions to O atoms [120–122, 124, 176], but this argument has to be treated carefully. Indeed, contrary to the present work where silicon tips are exclusively used, all the studies mentioned above involve metallic tips. Since it is well known that this kind of tips exhibits a stronger interaction with surface anions [197–199] it is obvious that O atoms are preferentially imaged when scanned by a metallic tip. Therefore, considering the particular case of a silicon tip scanning a NiO surface, it cannot be strictly excluded that the type of imaged atoms is changing from one image to another with respect to the polarity of the tip, as it has been previously observed on TiO_2 [141, 142, 200]. Yet, given that, no spontaneous contrast inversion has been observed during the imaging process, the previous hypothesis is highly unlikely.

Consequently, even if the present experiment does not allow to state clearly concerning the nature of the imaged atoms, the comparable contrasts highlighting the same orientations of the atomic rows as well as the similar values of the measured lattice parameters, for type 1 and type 2 surfaces, confirms at least that the imaged samples are effectively both NiO(001) surfaces independently of their different large scale morphology.

4.3 Line defects

It has been shown earlier that, depending on the batch from which the single crystal originates, two type of surfaces can be observed when following the same preparation process. This section here, focuses exclusively on type 2 surfaces where straight step edges are running along the $\langle 110 \rangle$ crystallographic directions of the NiO surface. Figure 4.3a shows one of these surfaces where small line defects which are parallel to the step edges can be observed.

In general, when following the preparation process which is described in section 2.3.1 of chapter 2, the length of these line defects is typically lying in the range of 5 to 20 nm. Interestingly, the size of these defects can be dramatically enlarged when the duration of the second annealing cycle is significantly extended (to 4h instead of 1h)

and its temperature is increased (from 500° to 600°). Figure 4.3b shows such a surface prepared through this altered process. The shape and direction of the line defects are unchanged but their length can now reach several tens of nm implying that they can cross a complete terrace. Nevertheless, these defects seem not to overpass the step edges. Contrary to the length of the defects, their heights, which are measured thanks to the profiles that are displayed in figures 4.3c and 4.3d, are staying constant and are estimated to be $h_{\text{defect}} \sim 120$ pm. This corresponds to roughly 60% the height of a step edge ($h_{\text{step}} \sim 210$ pm). However, because the surface potential at step edges is surely different than on defects, these heights cannot be really compared, and seeing bright defect doesn't necessarily mean that they are composed of adding rows of substrate material or related to surface contamination, but could also be related to vacancies [201].

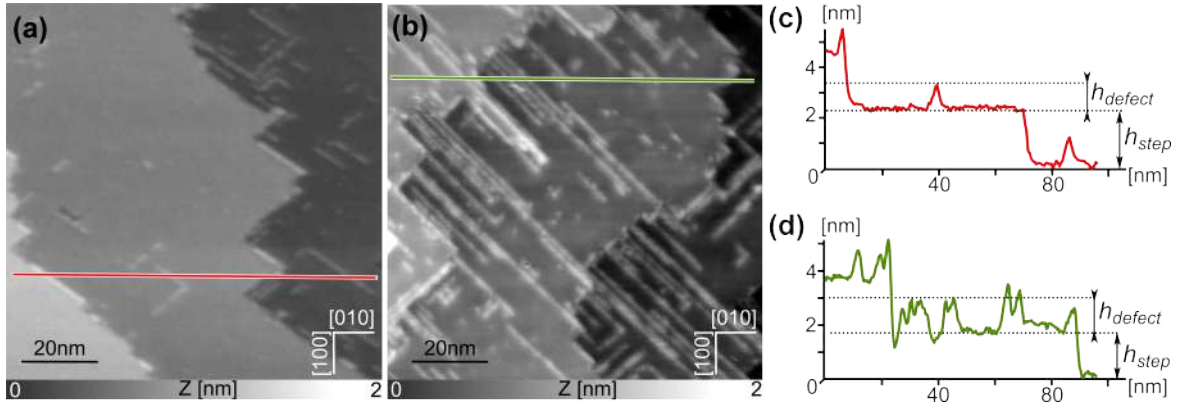


Figure 4.3: Preparation process induces tunable line defects. *a–b*, Large scale topographic images showing the line defects of $\text{NiO}(001)$ surfaces prepared by two different preparation processes. Increasing the annealing temperature and duration leads to surfaces which are defect richer. *c–d*, Profiles recorded along red and green lines of *a* and *b*, respectively. Scan parameters: *a*: $A_1 = 5$ nm, $\Delta f_1 = -9$ Hz. *b*: $A_1 = 9$ nm, $\Delta f_1 = -7$ Hz.

Not only the length of the defects is affected through this alternative preparation process, but also their number is drastically increased. Indeed whereas less than 10% of the surface is covered with defects when the preparation process presented in section 2.3.1 is respected, this proportion is increased to over 30% in case of an altered preparation process, suggesting that the defect ratio can be controlled and tuned. This property is of great interest since it has been shown in previous works that defect-rich surfaces favour the anchoring of atoms or molecules [164, 194, 202–204]. Indeed, it is well known that defects can act as nucleation center and thus can form strong bonds with molecules [205, 206]. It has also been shown that nanostructured surfaces can be used to trap nano-particles or organic molecules [207, 208]. Nevertheless, defects can also alter the physical intrinsic properties of semiconductors [209, 210]. For this reason, the defect proportion has to be kept to a reasonable level.

Figure 4.4 shows one of the previously mentioned line defect with higher magnification. In the topographic image displayed in figure 4.4a, recorded in the first scanning

pass while regulating the tip/sample distance by applying a constant Δf_1 , the defect appears actually as two strands. Figure 4.4b presents the corresponding Δf_1 image recorded in the second scanning pass while applying a z_{offset} of -600 pm. This image unambiguously shows that the strands are directed along the $[\bar{1}10]$ crystallographic direction of the surface and that their structure can be resolved. In addition, a feature that appears next to the double stranded line defect is visible in this image. Since it was observed for several different cases it is attributed to a double tip, which is imaging two times the same strand. It has been observed that double tip behaviour is pretty common on this kind of defect-rich surfaces. This can be related to the fact that defects are the cause of surface instabilities, which can lead to modification of the tip geometry. The profiles recorded along the red and green lines on the surface and the line defect, respectively, and displayed in figure 4.4c point that the distance between two bright protrusions is the same no matters if it is measured on the surface or on the defect. This altogether is suggesting that line defects are adding or missing rows consisting of surface material. However, given that only one type of atoms, is imaged by the AFM tip (see section 4.2), it is difficult to conclude concerning the composition of these rows. Namely if they are exclusively composed of one type of atoms or if they consist of adjacent rows composed of alternating type of atoms, where the second type of atoms are not visible.

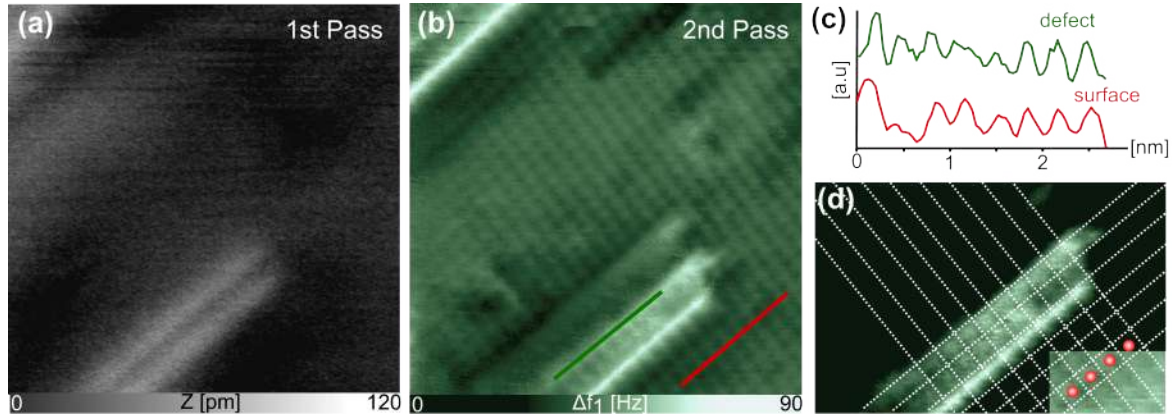


Figure 4.4: Atomic resolution on line defects. *a*, Topographic image of a line defect acquired in the first scanning pass. *b*, Δf_1 image recorded in the second scanning pass showing atomic resolution on a line defect. *c*, Profile recorded in *b* along the green (defect) and red (surface) lines. *d*, Close up Δf_1 image of *b* with modified contrast, showing that atoms from the same type are sitting on top of each other. Scan parameters: $A_1 = 4$ nm, $\Delta f_1 = -42$ Hz and $z_{offset} = -600$ pm.

Figure 4.4d is a close up look of 4.4b with modified contrast, so that the atoms of the defect are better visible. The structure of the surface is represented through white dotted lines, where the center of the checks coincides with the center of the surface atoms. Surprisingly, it can be seen in this image that the atoms of the line defect appear to sit exactly on top of the surface atoms. Meaning that atoms from the same type are sitting on top of each other which is energetically unfavourable. Therefore, and contrary to what was suggested above, it is thus highly unlikely that the defects

correspond to adding or missing rows of surface atoms. A second explanation would be that the strands are formed by H atoms that anchor on top of the oxygen rows of the surface. However, it has been seen that the number of defects is increasing after annealing, but it is also well known that this type of treatment leads to reduction of the surface. In other words, the amount of surface oxygen is decreased. Yet, if there is less oxygen, there are also less anchoring sites for H atoms meaning that the number of defects should drop upon annealing. Consequently, the last possible interpretation for the line defects is that they are related to bulk impurities segregation similar to what was observed on the surface of $\text{TiO}_2(110)$ [144]. Considering that several studies have proven the presence of this type of impurities in the bulk of single NiO crystals [211–214], and that line defects were not observed on type 1 surfaces, this reading for the compositions of defects is certainly the most reliable. The fact that the strands are appearing exclusively on type 2 surfaces, would then mean that the samples originating from the two last batches are less pure than the ones from the first batch.

4.4 Summary

In this chapter the surface of $\text{NiO}(001)$ was investigated. In a first part it was shown that clean and atomically flat surfaces can be obtained when following a rigorous preparation process. However, depending on the batch from which the crystal were originating, two types of surfaces were observed with different step shapes but constant step heights. In a second part, both types of surfaces could be resolved down to the atomic scale with several measurement techniques. The single atoms as well as their cubic packing pattern were observed. The last part focused on the line defects present on the surface of $\text{NiO}(001)$. It was shown that the length but also the number of these defects can be tuned by annealing. These defects were always oriented alongside the $\langle 110 \rangle$ crystallographic directions of the $\text{NiO}(001)$ surface and could be resolved with atomic accuracy. The composition of the strands remains unclear but it is thought that they can be related to bulk impurities segregation.

Comparing Standard n- and p-Type Dyes

IN the context of p-type dye sensitized solar cells, not only the choice of the semiconductor is crucial but also the careful selection of the sensitizers is significant. In this chapter, two dyes, which are originally designed for different types of DSSCs, are presented and studied by SPM techniques after adsorption on the surface of NiO(001). In the first part, the dye molecules are described and their characteristics are discussed. The motivations concerning the choice of these two specific molecules is explained. Then, the morphologies of the hybrid interface formed by the dyes adsorbed on the surface of NiO(001) are investigated by nc-AFM and the n- or p-type character of both dyes are determined using KPFM. As expected it is shown by experiments at the nanoscale that one dye is better adapted than the other for the design of p-type DSSCs.

5.1 Motivation

Lately, the wide band gap n-type semiconductor TiO_2 has become one of the most intensively studied metal oxide material in the field SPM [22–24, 164, 167, 170, 215, 216] with the purpose of using it in the context of dye sensitized solar cells (DSSCs). The working principle of this type of hybrid photovoltaic device entirely relies on a photoactive anode which is directed by the capacity of TiO_2 to absorb light after functionalization with organic molecules. There, excited electrons, that result from the absorption of incoming photons, are injected from the lowest unoccupied molecular orbital (LUMO) of the dye molecule into the conduction band (CB) of the semiconductor [137]. In contrast, even though NiO, was reported to be the first wide band gap p-type semiconductor [13], and can therefore be used for the fabrication of prototypical p-type DSSCs [8, 14, 217], its functionalization has only rarely been studied by the means of SPM techniques [52, 53, 161, 176]. In this second type of DSSCs, which are based on photoactive cathodes, the charge transfer mechanism has an opposite direction in comparison with n-type devices. Indeed, in this case, holes are injected from the highest occupied molecular orbital (HOMO) of the dye to the valence band

(VB) of the semiconductor after photon absorption. Consequently, the direction of the charge transfer, which can be tuned by adjusting the positioning of the energy levels of the molecular orbitals of the dye in comparison to the CB and VB of the metal oxide, is of paramount importance for the proper functioning of the devices. In other words, the ability of a dye molecule to accept or donate electrons, after it is adsorbed on the surface of the semiconductor, plays a crucial role for the manufacturing of optimized DSSCs. Therefore, dye molecules are specifically designed to be compatible with either n- or p-type cells. In the following, these two types of molecules, will be referred to as n- and p-type dyes, respectively.

Figure 5.1 presents the chemical structures of two molecules that are intended for different types of devices. Copper(II) meso-tetra (4-carboxyphenyl) porphyrin (Cu-TCPP) is comparable to some prototypical dye molecules that can be implemented for the design of n-type DSSCs [21,218], and can therefore be considered as a n-type dye. On contrary, Coumarin 343 (C343) can be used for the fabrication of working p-type devices [7,219].

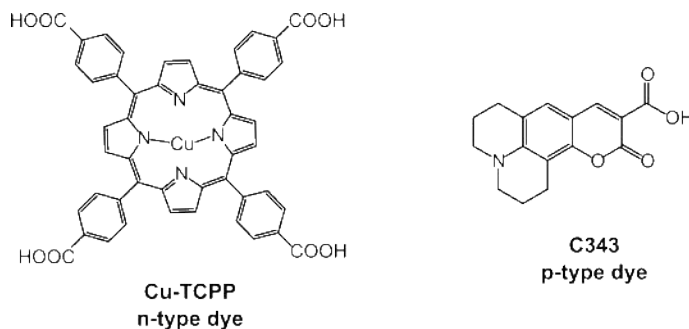


Figure 5.1: Chemical structure of Cu-TCPP and C343. *Copper(II) meso-tetra (4-carboxyphenyl)porphyrin (Cu-TCPP) is a n-type dye whereas Coumarin 343 (C343) is a p-type dye.*

5.2 Interface morphologies imaged by nc-AFM

This section is dedicated to the investigation of the adsorption properties of the n-type Cu-TCPP and the p-type C343 dye molecule on a type 2 NiO(001) surface (see section 4.1 in chapter 4). It is shown that both molecules tend to form molecular islands, where molecules are lying flat on the surface of this metal oxide. These assemblies are resolved with molecular accuracy by the means of nc-AFM.

5.2.1 Cu-TCPP islands formed on NiO(001)

In a first experiment, Cu-TCPP dye molecules are evaporated onto the surface of NiO(001). Figure 5.2a presents a large scale topographic image where it can be seen that the molecules appear either to form small cluster or to assemble in molecular islands on the surface of the semiconductor at RT. The emergence of large molecular

5.2. Interface morphologies imaged by nc-AFM

island, that can reach 80 nm in width at RT, arises because the diffusion rate of the molecules on the surface of NiO(001) is relatively large. In addition, the fact that numerous clusters are observed can be explained by the presence of a large amount of favorable anchoring sites such as defects or step edges. After annealing at 440 K, it can be seen in figure 5.2b, that the terraces of NiO(001) are still covered with numerous molecules but molecular islands are not longer observed. This demonstrates that the interactions between the Cu-TCPP molecules and the surface, especially at defects and step edges, are stronger than the interactions in between molecules. Thus, in order to better understand which mechanism triggers the formation of molecular islands, the following study focuses exclusively on these assemblies and not on single molecules or clusters. The height of these islands, which is between 250 and 300 pm indicate that the molecules are lying flat on the substrate. In addition, it can be seen in figure 5.2a, that the islands exhibit two types of assemblies (1 and 2) where the molecular rows are aligned along two different angles with respect to the [010] crystallographic direction of the substrate (see red and blue dotted lines). This suggests that the surface symmetries are playing a crucial role for the adsorption of molecules. With this in mind it is expected to observe the same anchoring geometry of the molecules, with their anchoring groups coupled always to the same kind of surface atoms, independently of the island type.

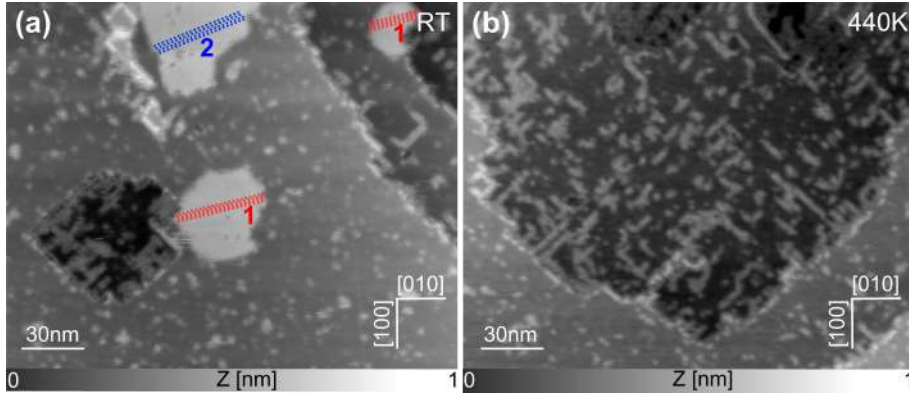


Figure 5.2: Cu-TCPP adsorbed on NiO(001). *a*, Large scale topographic image showing that, at RT, Cu-TCPP molecules form islands that have two different orientations with respect to the crystallographic direction of NiO(001). *b*, Large scale topographic image of the same sample after annealing at 440 K. Scan parameters: *a*: $A_1 = 7$ nm, $\Delta f_1 = -7$ Hz. *b*: $A_1 = 4$ nm, $\Delta f_1 = -18$ Hz.

The adsorption geometry of Cu-TCPP is resolved in figure 5.3a and 5.3b, which are acquired respectively in the first and second scan pass of the multipass technique on top of a type 2 island. The frequency shift image shown in figure 5.3b, which is recorded following the topography of figure 5.3a and applying a z_{offset} of -600 pm, reveals that the molecules are aligned in the assembly with their molecular axis oriented along the [110] direction of the substrate (see model 5.3c). In the frequency shift image it can also be seen that the upper right edges of the Cu-TCPPs appear with a brighter contrast compared to the rest of the molecule. However, since a slight asymmetry

is also visible in the topographic image, it is thought that this particularity is an imaging artefact originating from a irregular tip geometry, rather than a real feature arising from the actual adsorption geometry of the molecule. Moreover, an asymmetric adsorption geometry of the Cu-TCCP molecule is highly improbable because of its four equivalent anchoring groups which should exhibit similar interactions with the surface. This would in turn surely lead to a flat lying configuration of the molecule on the surface of NiO. Based on these statements, it is assumed in the following that the molecules of both island types adsorb in the same flat lying geometry. Considering the partial charge distribution of the surface (Ni is $\delta+$ and O is $\delta-$), the tentative model depicted in figure 5.3c highlights that the metallic core of the molecule as well as its four anchoring groups are likely located above of O atoms.

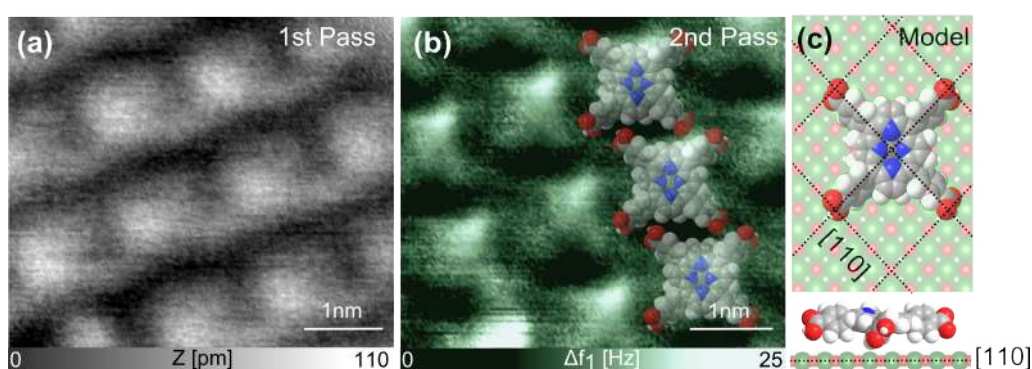


Figure 5.3: Submolecular resolution on a Cu-TCCP island. *a*, Topographic image recorded in the first pass of the multipass scanning mode of AFM on top of a Cu-TCCP island. *b*, Corresponding frequency shift image acquired in the second pass highlighting the adsorption geometry of Cu-TCCP on the surface of NiO(001). Scan parameters: $A_1 = 7$ nm, $\Delta f_1 = -12$ Hz, $z_{offset} = -600$ pm.

At this point, it is worth to mention that, in order to facilitate the reading of the following part, ρ_1 and ρ_2 are defined as the angles with respect to the [010] direction of the substrate along which the molecular rows of type 1 and 2 islands are aligned, respectively. a_1 and b_1 refer to the lattice vectors of one unit cell of type 1 island and θ_1 is the angle between these vectors. Analogue denominations are used for type 2 islands where a_2 and b_2 vectors are separated by a θ_2 angle. D_1 and D_2 stand for the molecular densities of both island types.

Close up topographic images acquired on top of both types of islands allow to study more in details the packing properties of Cu-TCCP. The molecular alignment of type 1 and 2 islands are resolved in figures 5.4a and 5.4d, respectively. The angles ρ_1 and ρ_2 are measured to be $\sim \pm 10^\circ$ and $\sim \pm 20^\circ$, respectively and the lattice parameters a_1 , b_1 , a_2 and b_2 are all estimated to lie in the range of $\sim 1.5 \pm 0.1$ nm. In contrast to the unit cell vectors which present similar values, the angle θ_1 and θ_2 are perceptibly different, and their values are measured to be around $\sim 88^\circ$ and $\sim 82^\circ$, respectively. Based on the high resolution images and the FFT signals displayed in figures 5.4b and 5.4e, the molecular densities of both types of islands (D_1 and D_2) are estimated to be $\sim 0.46 \pm 0.2$ nm⁻². Knowing the structure of the substrate and assuming that the Cu-

5.2. Interface morphologies imaged by nc-AFM

TCPP molecules adsorb in a flat lying geometry with their molecular axis along the [110] direction of the substrate and their metallic core, as well as their anchoring groups, above O atoms, tentative models corresponding to the experiments can be established. The latter are displayed in figure 5.4c and 5.4f and suggest that the molecules are linked to each other via H-bonding in between their carboxylic groups. Model values for the lattice parameters can be calculated: $a_1 = 1.47$ nm, $b_1 = 1.47$ nm, $\theta_1 = 90^\circ$, $D_1 = 0.46$ nm⁻², $a_2 = 1.62$ nm, $b_2 = 1.32$ nm, $\theta_2 = 85.2^\circ$, and $D_2 = 0.48$ nm⁻². These values are compared to the experimental parameters in table 5.1. The fact that experimental and model results are fitting pretty nicely suggests that the latter is relatively accurate and therefore present reliable mesh motifs for type 1 and 2 islands.

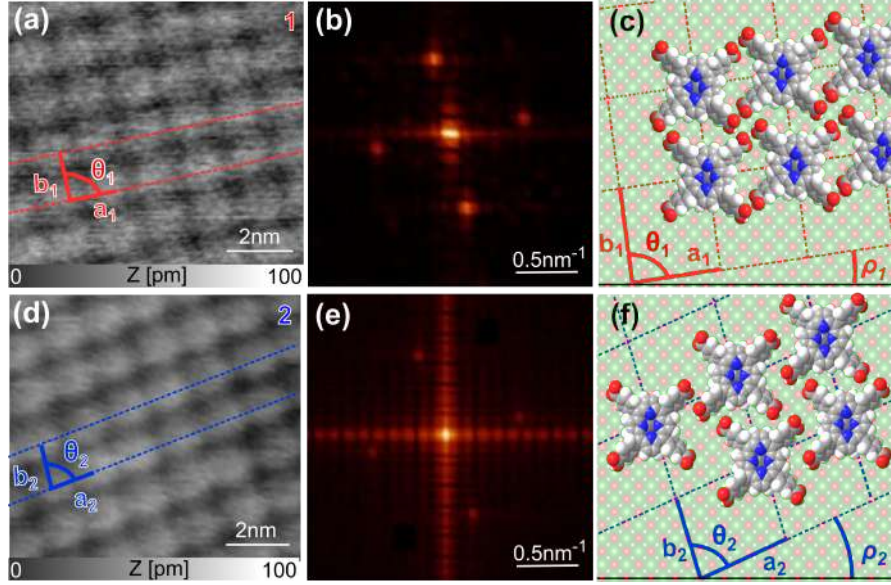


Figure 5.4: Molecular orientations of type 1 and 2 islands. *a and d*, Close-up topographic images showing the two different orientations of type 1 and 2 islands, respectively. *b and e*, Corresponding FFTs. *c and f*, Corresponding models. Scan parameters: *a-b*: $A_1 = 4$ nm, $\Delta f_1 = -38$ Hz. *d-e*: $A_1 = 7$ nm, $\Delta f_1 = -8$ Hz.

Molecules	Mesh parameters		Molecular density	
	Exp.	Model	Exp.	Model
Cu-TCPP type 1	$a_1 \sim 1.5 \pm 0.1$ nm $b_1 \sim 1.5 \pm 0.1$ nm $\theta_1 \sim 88^\circ$	$a_1 = 1.47$ nm $b_1 = 1.47$ nm $\theta_1 = 90^\circ$	$D_1 \sim 0.46$ nm ⁻²	$D_1 = 0.46$ nm ⁻²
Cu-TCPP type 2	$a_2 \sim 1.5 \pm 0.1$ nm $b_2 \sim 1.5 \pm 0.1$ nm $\theta_2 \sim 82^\circ$	$a_2 = 1.62$ nm $b_2 = 1.32$ nm $\theta_2 = 85.2^\circ$	$D_2 \sim 0.46$ nm ⁻²	$D_2 = 0.48$ nm ⁻²

Table 5.1: Parameters measured and calculated for Cu-TCPP islands.

5.2.2 C343 islands formed on NiO(001)

In a second experiment, C343 dye molecules are evaporated onto the surface of NiO(001). In the topographic images displayed in figure 5.5 it can be seen that the morphology of the sample drastically depends on the molecular coverage. When the latter is kept low (~ 0.1 ML), as shown on figure 5.5a, the C343 molecules appear to aggregate in small molecular clusters that preferentially adsorb at step edges or defects. The homogeneous distribution of these clusters over the terraces of NiO implies a relatively low diffusion rate of the molecules. In figure 5.5b, which shows the same sample imaged after annealing at 380 K, it can be seen that the morphology of the interface has not been modified. This suggests that the low diffusion rate of C343 cannot be increased via this type of treatment, and therefore that the formation of molecular islands cannot be triggered at low molecular coverage.

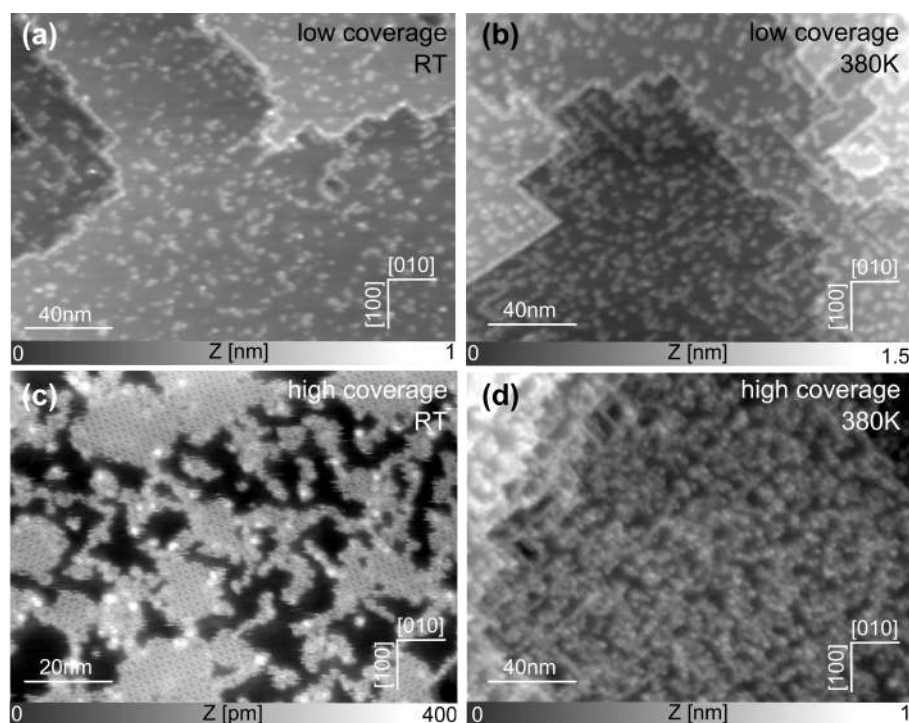


Figure 5.5: C343 adsorbed NiO(001). *a*, Large scale topographic image after low coverage deposition of C343 molecules at RT. *b*, Topographic image of the same sample after annealing at 380 K showing the same morphology than *a*. *c*, Large scale topographic image after higher coverage deposition of C343 molecules at RT showing the formation of islands. *d*, Topographic image of the same sample after annealing at 380 K showing a different morphology than *c*. Scan parameters: *a*: $A_1 = 7$ nm, $\Delta f_1 = -10$ Hz. *b*: $A_1 = 7$ nm, $\Delta f_1 = -5$ Hz. *c*: $A_1 = 7$ nm, $\Delta f_1 = -7$ Hz. *d*: $A_1 = 7$ nm, $\Delta f_1 = -9$ Hz.

Thus, C343 islands can be observed only when the coverage is increased (~ 0.6 ML), as illustrated in figure 5.5c, where molecular islands, that are 10 to 30 nm in width, are observed at RT. The fact that these islands are smaller compared to the assemblies

formed by Cu-TCPP suggests that the limited diffusion rate of C343 observed at lower coverage is even smaller in comparison to the Cu-TCPP. This is unexpected since the latter is designed with four carboxylic anchoring groups contrary to C343 who has only one. However, since the defect density of the surface can also strongly influence the anchoring of molecules, a defect richer surface can theoretically lead to formation of more but also smaller islands. Because C343 were deposited on a different surface than Cu-TCPP it is therefore difficult to conclude with respect to this point. Nonetheless, comparably to Cu-TCPP, it can be seen in figure 5.5d that the crystallinity of the molecular assemblies, which are formed at high coverage at RT, is lost when the sample is annealed at 380 K, suggesting that the molecule/molecule interactions are weaker than the molecule/surface bonds, also in the case of C343. This indicates that the forces acting in between the molecules or between the molecules and specific anchoring sites of the NiO surfaces are originating from the same interaction than in the case of Cu-TCPP.

In order to confirm this hypothesis, the molecular islands formed by C343 on the surface of NiO are studied in more detail in the following. In the image presented in figure 5.6a, it can be seen that even if their sizes differ in width from one island to another, their heights of ~ 250 -300 pm are constant, suggesting that, similar to Cu-TCPP, C343 are adsorbing in a flat lying geometry. On the other hand, unlike Cu-TCPP, only one type of island is observed for C343. The molecules are oriented along an angle which is measured to be $\rho_3 \sim \pm 15^\circ$ with respect to the [010] direction of the substrate.

Figure 5.6b shows a close up topographic image acquired on top of one of those C343 islands. In this image it can be seen that a mesh motif is composed of two pairs of molecules where the first pair has its molecular axis oriented along vector a_3 and the second pair aligns following vector b_3 , resulting in a unit cell containing four molecules. The mesh parameters a_3 and b_3 are measured to be 3.5 ± 0.1 nm and 1.5 ± 0.1 nm, respectively and an angle $\theta_3 \sim 87^\circ$ is measured between these vectors. Which leads to a molecular density of $D_3 = 0.74 \text{ nm}^{-2}$. The mesh motif, observed in figure 5.6b, is mimicked in the tentative model displayed in figure 5.6c. The alternating orientation of the molecules composing one pair is reproduced by operating an inplane rotation of C343 by 180° . Because C343 is a prochiral molecule when confined to 2D [52, 75, 220–224], two distinct molecule chiralities (α and β) are expected to be observed. However, the topographic image as well as the model suggest that the molecular domains are enantiopure. In the present work, only one of the two chiralities was observed, but this can surely be related to the fact that only a very limited number of islands could be imaged with a sufficient accurate resolution to determine the configuration of the molecules. Thus, in order to conclude concerning the value of the ratio $\alpha:\beta$, a more statistical study, involving high resolution imaging, would be needed. Nonetheless it can reasonably be expected that this ratio is 1:1. In the model, it can also be seen that, the pairs formed by the molecules are resulting from formation of H-bonds in between their carboxylic acid groups. The following values result from the model: $a_3 = 3.44$ nm, $b_3 = 1.47$ nm, $\theta_3 = 84.1^\circ$ and $D_3 = 0.79 \text{ nm}^{-2}$. The latter are compared to the experimental values in table 5.2 where it can be seen that they are matching again pretty nicely confirming the reliability of the model.

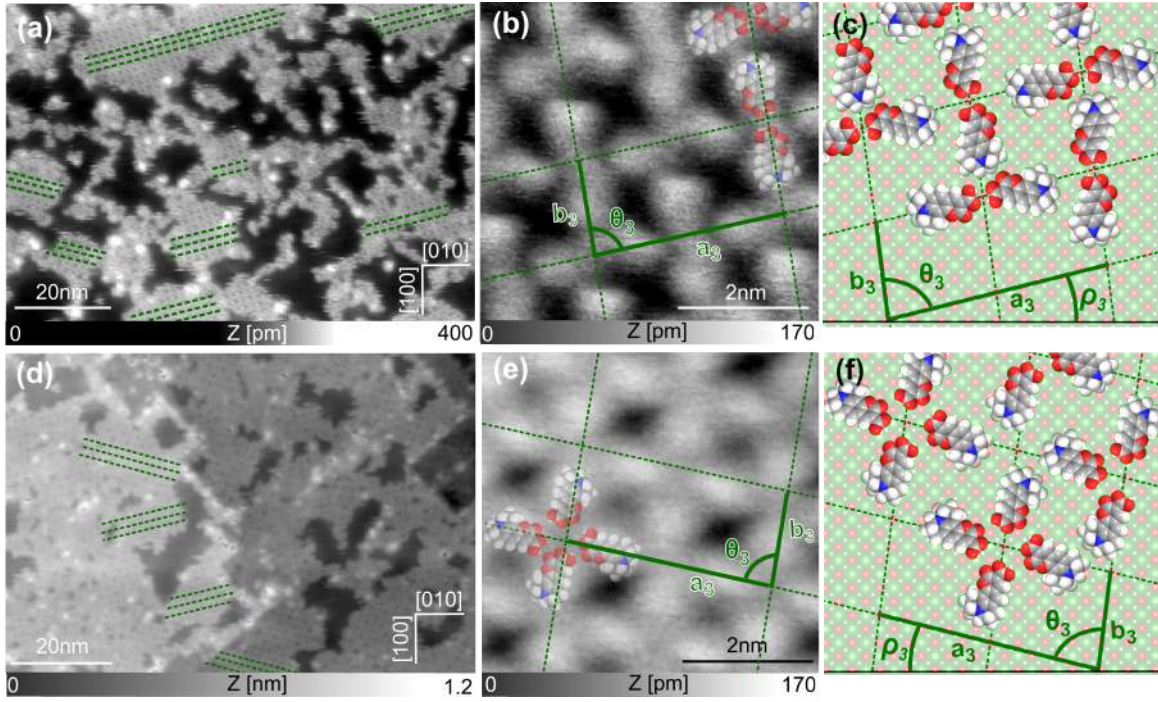


Figure 5.6: C343 islands on NiO(001). *a*, Large scale topographic image showing that C343 molecules form islands that present only one orientation with respect to the crystallographic direction of NiO(001). *b*, Close-up topographic image recorded on top of a C343 island and *c*, its corresponding model. *d*, Large scale topographic image showing C343 islands on a second NiO(001) sample. *e*, Close-up topographic image recorded on top of a C343 island showing a different contrast than *b*, and *f*, its corresponding model. Scan parameters: *a*: $A_1 = 7 \text{ nm}$, $\Delta f_1 = -7 \text{ Hz}$. *b*: $A_1 = 7 \text{ nm}$, $\Delta f_1 = -7 \text{ Hz}$. *d*: $A_1 = 5 \text{ nm}$, $\Delta f_1 = -13 \text{ Hz}$. *e*: $A_1 = 5 \text{ nm}$, $\Delta f_1 = -15 \text{ Hz}$.

Molecules	Mesh parameters		Molecular density	
	Exp.	Model	Exp.	Model
C343	$a_3 \sim 3.5 \pm 0.1 \text{ nm}$ $b_3 \sim 1.5 \pm 0.1 \text{ nm}$ $\theta_3 \sim 87^\circ$	$a_3 = 3.44 \text{ nm}$ $b_3 = 1.47 \text{ nm}$ $\theta_3 = 84.1^\circ$	$D_3 \sim 0.74 \text{ nm}^{-2}$	$D_3 = 0.79 \text{ nm}^{-2}$

Table 5.2: Parameters measured and calculated for the C343 island.

Comparably to figure 5.6a, the large scale topographic image displayed in figure 5.6d shows the molecular assemblies formed by C343 molecules on the surface of NiO(001). Even though, both samples were obtained using similar preparation processes, the molecular coverage appears to be higher on the second surface. Here also, C343 islands are formed, but because of the larger number of molecules, it is observed that the crystallinity of the molecular layers is affected. Indeed, on account of the reduced available space on the bare substrate, crystalline islands are observed to merge with less ordered areas resulting in a molecular layer that is of poor quality in terms of long range order. However, within this layer, several zones presenting a reliable crystallinity

can be identified. The latter exhibit molecular rows that are oriented along an angle $\rho_3 \sim \pm 15^\circ$ with respect to the [010] direction of the substrate, similar to what has been observed in figure 5.6a.

Figure 5.6e shows a close up topographic image acquired on top of one of those crystalline zones. This image presents a different contrast in comparison to figure 5.6b. Indeed, instead of presenting a mesh motif that is composed of two pairs of molecules, it seems that the molecules are linked four by four, forming a cross like structure and resulting, as well, in a unit cell that consists of four molecules. The experimental lattice parameters a_3 , b_3 , θ_3 and D_3 are also measured to be the same than for figure 5.6b. Consequently a second tentative model representing the mesh motif of a C343 island is displayed in figure 5.6f. The latter, which highlights the bonding of one molecule to three of its neighbours via H-bridging of their carboxylic groups also fits nicely with the experiment.

Thus, two different models corresponding nicely to the experimental results are available. In order to unambiguously state which one is the most accurate, further investigations involving submolecular imaging are required. Yet, considering that the contrast presented in figure 5.6b was more regularly observed than the contrast highlighted in figure 5.6e, it is thought that a mesh motif composed of two pairs of molecules, instead of four molecules arranged in a cross like feature, is more realistic. In addition, whereas the surface charges were compensated only locally in figure 5.6e, figure 5.6b was recorded while combining topographic and KPFM measurements, which should result in a more reliable contrast.

5.3 Charge transfer direction studied by KPFM

This section focuses on the comparison of the n- and p-type character of Cu-TCP and C343 after adsorption on the surface of NiO(001). The CPD between the surface and the different molecular islands are determined by FM-KPFM [225]. Because the CPD value measured on the surface of NiO can vary by about ± 100 mV depending on the tip, it is worth to mention that, for simplification reasons with the aim of facilitating the comparison between both samples, this value is set to 0 V. Consequently, all the values given below are relative CPDs.

Figure 5.7a presents a large scale KPFM image acquired simultaneously to the topography shown in figure 5.2a. Here it can be seen that the CPD is lowered above the molecular layers in comparison to the bare substrate. This is also visible in figure 5.7b where a line profile is displayed. The latter emphasizes that the CPD is decreased by roughly -400 mV. This value is confirmed by analysing a larger set of images using the method described in section 1.3, resulting in a $\Delta V_{CPD} = -400 \pm 50$ mV, independently of the island type. This drop in the absolute CPD is directly related to a decrease of the work function, which in turn is associated to a more positively charged molecular island in comparison to NiO. This effect is therefore attributed to a dipole moment pointing towards the molecular layer, originating from partial charge transfer directed from the molecules towards the underlying sample (see figure 5.7c) implying the electron donor character of Cu-TCP upon adsorption on NiO. This corresponds

to what is expected when an n-type dye molecule is adsorbed on the surface of a semiconductor. As discussed in section 1.3, the value of the average dipole moment and the corresponding partial charge transfer can be deduced from the measured CPD [62, 63] and the value of the molecular density. Thus, because type 1 and 2 Cu-TCPP islands present slightly different densities, the average dipole moment is calculated to be -2.3 D/molecule for type 1 and -2.1 D/molecule for type 2 assemblies. Resulting in a partial charge transfer which is 0.34 and 0.35 e^- /molecule, respectively. Consequently, the intensity of the charge transfer triggered when Cu-TCPP molecules are adsorbed on NiO, is determined to be roughly equal to 0.16 e^-/nm^2 .

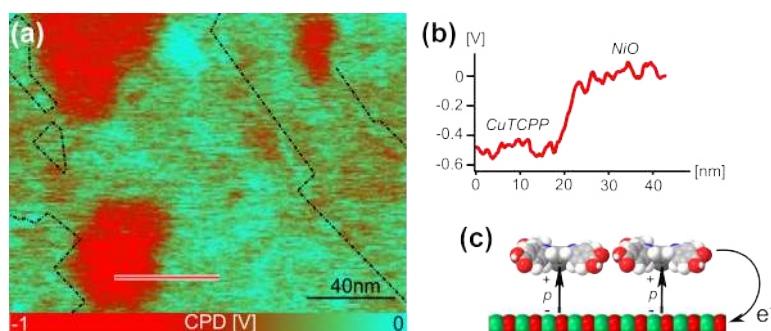


Figure 5.7: CPD on Cu-TCPP adsorbed on NiO. *a*, KPFM signal measured on Cu-TCPP islands formed on the surface of NiO(001). *b*, Profile recorded along the red line displayed in *a*. *c*, Sketch highlighting the direction of the charge transfer from the molecular layer to the surface of NiO. Scan parameters: $A_1 = 7$ nm, $\Delta f_1 = -7$ Hz, $V_{AC} = 800$ mV and $\omega = 1$ kHz.

The KPFM signal displayed in figure 5.8a showing C343 islands formed on the surface of NiO, was acquired simultaneously to figure 5.6a. Unlike figure 5.7a, it can be seen in this image, that the CPD contrast is varying a lot over large scales and is not restricted to a clear distinction between bare substrate and molecular layer. This originates from surface charge variations that probably arise after cleavage. For this reason, in order to be able to distinguish better the molecular layers from the bare substrate, the edges of the islands are highlighted through black dotted lines in this image. However, despite this long range charge variations, a clear contrast can unambiguously be determined locally. Indeed, when focusing on smaller areas, where the KPFM contrast is not directed by large scale charge variations, it can be stated that the CPD is increased above molecular islands compared to the metal oxide (see areas A, B, C and D in figure 5.8). Thus, contrary to Cu-TCPP, the work function is locally increased resulting in a charge transfer in opposite direction, *i.e.* from the substrate toward the molecules (see figure 5.8d), which fits to the expected electron acceptor behaviour of a p-type dye molecule. The local increase of the CPD is also observed in figure 5.8b which shows a KPFM image with molecular resolution. From this image, as well as the profile displayed in figure 5.8c, which was recorded along the green line shown in figure 5.8a, the value of ΔV_{CPD} can be deduced to be around 150 mV. As for Cu-TCPP, this value was confirmed by analysing a larger set of images resulting in a value that is 150 ± 30 mV. This value is attributed to an average dipole moment of

0.5 D/molecule corresponding to a partial charge transfer of $0.08e^-$ /molecule implying that, in terms of charge transfer intensity, the p-type C343 molecule appears to be around 4 times weaker than n-type Cu-TCPP. This can easily be explained by the fact that C343 has only one carboxylic acid anchoring group which can act as a dipole when the molecule is adsorbed on a surface in contrast to Cu-TCPP which has four. However, when the charge transfer is calculated in function of active area instead of single molecule, and because C343 is smaller in size than Cu-TCPP, its value becomes $0.06e^-/\text{nm}^2$. Thus, this implies that C343 is roughly 2.5 times less efficient in terms of charge injection than Cu-TCPP if one thinks about designing a prototypical device.

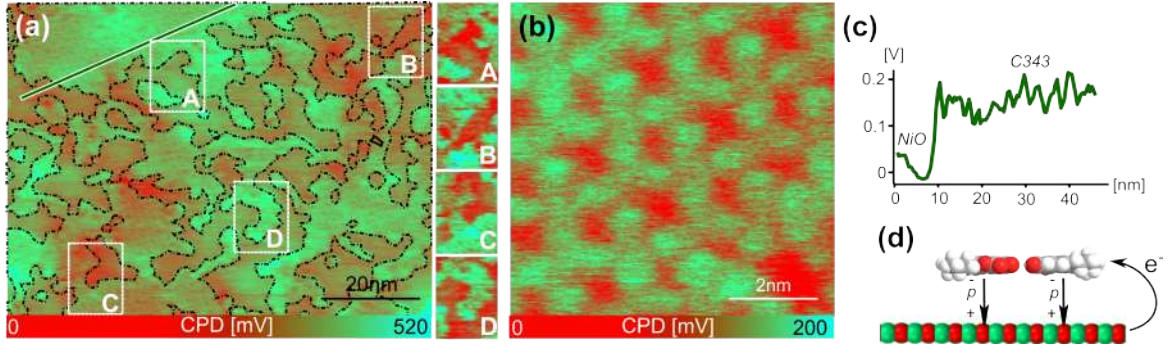


Figure 5.8: CPD on C343 adsorbed on NiO. *a*, KPFM signal measured on C343 islands formed on the surface of NiO(001). *b*, KPFM signal recorded on top of a C343 islands showing molecular contrast. *c*, Profile recorded along the green line displayed in *a*. *d*, Sketch highlighting the direction of the charge transfer from the surface of NiO to the molecular layer. Scan parameters: $A_1 = 7 \text{ nm}$, $\Delta f_1 = -7 \text{ Hz}$, $V_{AC} = 800 \text{ mV}$ and $\omega = 250 \text{ Hz}$.

In order to summarize the results, a comparison of Cu-TCPP and C343 in terms of n- and p-type character is given in table 5.3. Here it is worth to mention that + stands for a charge transfer directed from the molecular layer toward the substrate, whereas – stands for a charge transfer in opposite direction.

Molecules	ΔV_{CPD}	p /molecule	partial charge transfer		
			direction	/molecule	/nm ²
Cu-TCPP type1	$-400 \pm 50 \text{ mV}$	-2.3 D	+	$+0.35 e^-$	$+0.16 e^-$
Cu-TCPP type2	$-400 \pm 50 \text{ mV}$	-2.1 D	+	$+0.34 e^-$	$+0.16 e^-$
C343	$150 \pm 30 \text{ mV}$	0.5 D	–	$-0.08 e^-$	$-0.06 e^-$

Table 5.3: Comparison between Cu-TCPP and C343 adsorbed on NiO(001).

5.4 Summary

In this chapter, nc-AFM was employed in a first part in order to compare the adsorption of the n-type Cu-TCPP molecules to the p-type C343 dye on NiO(001). High

resolution imaging revealed that both dyes form molecular islands, where the molecules are lying flat on the surface of the metal oxide. Several types of islands originating from the fact that the molecules are oriented following different angles with respect to the [010] cristallographic direction of the substrate, were investigated. Models reproducing the different mesh motifs of the experiment, were established. Comparison between the values arising from the model with the experimentally measured lattice parameters demonstrated the larger molecular density of C343 compared to Cu-TCPP. Which is however expected because of the smaller size of C343.

KPFM measurements were performed with the prospect to state concerning the n- or p-type character of both molecules. Interestingly, it was observed that the work function is decreased above Cu-TCPP islands compared to the bare surface of NiO(001), whereas it is increased on top of C343 assemblies, implying that the charge transfer occurs in opposite directions from one molecule to the other. Cu-TCCP appear to injects electron to NiO while C343 accepts electrons and consequently injects holes. The values of these charge transfers were also calculated resulting in the fact that C343 appears to be less efficient than Cu-TCPP (0.16 against $0.06 e^-/\text{nm}^2$). Consequently, for the design of optimized p-type DSSC devices, the development of dyes combining the p-type character of C343 and the efficiency of Cu-TCPP is required.

Sensitization via On-Surface Synthesis

SENSITIZING inorganic surfaces with organic molecules, with the purpose of building hybrid interfaces, is an ubiquitous topic in the field of surface science in general and SPM in particular. However, this is not systematically easy to achieve, especially when metal oxides have to be functionalized with complex dye molecules that cannot be sublimated. Consequently, one possible method to fulfil this goal is to assemble the complete dye molecule on the specific surface. This method is expected also to result in more efficient dye molecules. In this chapter, the first steps of such an on-surface synthesis are followed with submolecular accuracy using several SPM methods. In a first part, the chemical reaction is described. It essentially consists in a successive assembly of a surface-bound heteroleptic dye. In the following parts, the adsorption of a dye precursor and the assembly of its metal complex from which the complete dye can originate are investigated at two different surfaces.

6.1 Motivation

In the context of p-type DSSCs, the hierarchical assembly strategy termed *surface-as-ligand surface-as-complex* (SALSAC) [226] is one of the options of sensitizing NiO surfaces for an optimized photon adsorption. This method allows to design novel molecular compounds owning anchoring groups such as carboxylic acids and a metal binding unit, such as 2,2'-bipyridine (bpy). The first groups are responsible for the anchoring of the molecule on surfaces and the second domain promotes ligand exchange when exposed to an homoleptic metal complex. As shown in figure 6.1, this strategy enables the synthesis of complex dyes through successive steps. Indeed, the dye precursor is, first of all, adsorbed on the surface of NiO, where it is then capped with a metal, followed by the ancillary ligand to complete the active dye [227–229].

In the context of DSSCs, this reaction is performed in solution. Nonetheless, because liquid environment is not compatible with the cleanliness level required for high resolution imaging, this is done under UHV conditions. Furthermore, the following work exclusively focuses on the first steps of the reaction involving the dye precursor DCPDM(bpy), which is based on a 6,6'-dimethyl-2,2'-bipyridine metal binding unit

with two 4-carboxyphenyl anchoring groups. Indeed, the adsorption of DCPDM(bpy) on surfaces as well as the formation of the complex M -DCPDM(bpy) triggered by binding of the bpy of DCPDM(bpy) to a metal M ($M = \text{Fe}$ or Au) is investigated by SPM techniques.

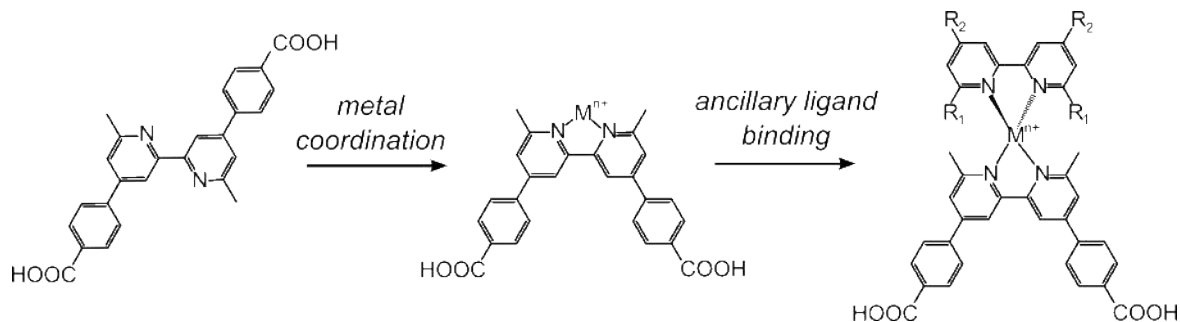


Figure 6.1: On–surface reaction. *The conformation of the dye precursor changes from transoid to cisoid upon coordination to a metal. The metal coordinated precursor, M -DCPDM(bpy), can further be capped with an ancillary ligand to form a photo active dye molecule.*

6.2 On–surface synthesis on NiO(001)

This section is dedicated to the study of the first steps of the above mentioned reaction on the surface of NiO(001) at RT. In a first part, the adsorption of the dye precursor DCPDM(bpy) on the surface of NiO is investigated at different coverages. Structural and electrical measurements performed by RT nc-AFM and KPFM are shown and discussed. In a second part the emergence of the specific iron complex Fe-DCPDM(bpy) is studied. It is shown that binding of the N atoms of the bpy domain of DCPDM(bpy) dye precursor to Fe atoms leads to a conformation change of the molecule.

6.2.1 Dye precursor anchoring on NiO(001)

The dye precursor DCPDM(bpy) molecules are sublimated onto the surface of NiO(001) kept at RT, with a low coverage rate, with the aim of imaging single molecules and resolve their adsorption geometry with submolecular accuracy by the means of nc-AFM. At this point it is worth to emphasize that all the images shown in this part were recorded at RT on a type 1 NiO surfaces with curvy step edges (see section 4.1 in chapter 4). Figure 6.2a shows the large terraces of NiO(001) covered with 0.2 ML of DCPDM(bpy). The fact that the bright protrusions, visible on the surface exhibit irregular shapes and sizes is related to the presence of both, molecular clusters and single molecules on the surface of NiO(001). Comparably to what can be observed on ionic crystals for several molecules [204, 230], DCPDM(bpy) manifests the clear tendency to preferentially adsorb at the upper as well as at the lower side of step edges. Nonetheless, the fact that terraces are homogeneously covered with molecules in addition to the relative small distance in between them (3.9 ± 0.7 nm in average, corresponding

to a relative interval of about twice the size of a molecule), suggests that the diffusion on NiO(001) is rather low. This therefore implies a relatively strong adhesion to the surface, which can, however, slightly be reduced when the sample is annealed 1 h at 420 K (see figure 6.2b). Indeed, upon this annealing treatment, the interval in between the protrusions is increased (5.3 ± 0.7 nm in average) and the step edges are completely saturated with molecules. Nevertheless this enhancement of diffusion is limited and can not be further improved. Annealing at higher temperature (500 K for 1 h) does not lead to intensification of the molecular mobility or to assembly formation, but rather results into desorption of DCPDM(bpy), as shown in figure 6.2c where the molecular density is drastically reduced in comparison to figure 6.2a and 6.2b.

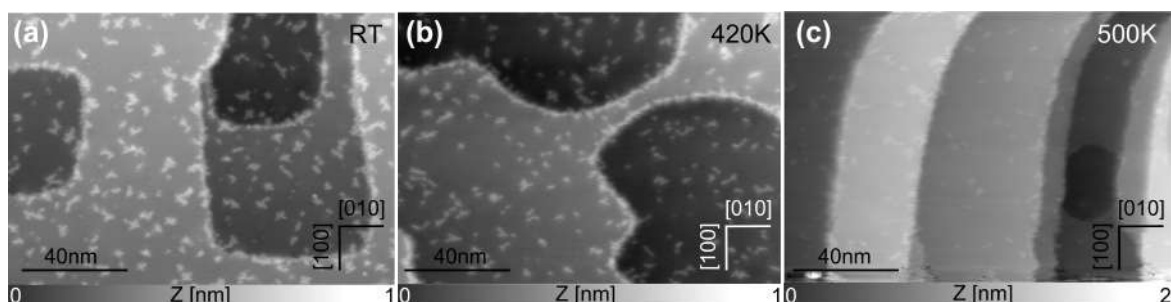


Figure 6.2: Annealing effect on the binding energy of DCPDM(bpy) to NiO(001). *a–c*, Topographic images recorded on a NiO(001) surface covered with 0.2 ML of DCPDM(bpy) molecules before and after annealing treatment of 420 K and 500 K, respectively. Scan parameters: **a**: $A_1 = 4$ nm, $\Delta f_1 = -3$ Hz. **b**: $A_1 = 4$ nm, $\Delta f_1 = -7$ Hz. **c**: $A_1 = 4$ nm, $\Delta f_1 = -6$ Hz.

The adsorption geometry of DCPDM(bpy) on a NiO(001) terrace is resolved using the multipass technique [51] (see section 1.2.3 in chapter 1). Because scan conditions are often unstable in close vicinity to the surface when measuring large corrugations, such as step edges, the multipass technique delivers reliable topographic informations for molecules adsorbed on terraces. Figure 6.3a shows an image of such a molecule acquired in the first scan pass using the previous mentioned method. The dimension of the protrusion imaged here is size consistent with the expected size of a single molecule (*i.e.* a length of ~ 1.8 nm). In addition the measured height of the present object (~ 200 pm) suggests that the single molecule is lying flat on the surface. Figure 6.3b presents the Δf_1 image of the same molecule recorded in the second scan pass of the multipass technique reducing the tip/sample distance by 350 pm in comparison to the first pass. It can be seen in that image that DCPDM(bpy) adsorbs in its transoid conformation on the surface of NiO(001). Interestingly, the transoid-geometry of DCPDM(bpy) can be observed before and after the sample is annealed at 420 K implying that temperature does not influence the conformation of the molecule. Knowing the atomic structure and the crystallographic orientation of the surface (see section 4.2 in chapter 4), a model of the absorption geometry of DCPDM(bpy) can be drawn. In the following it is considered that, because of minimization of H–H repulsions, the phenyl and pyridine rings are slightly twisted with respect to each other. Consequently, the model displayed in figure 6.3c, shows that DCPDM(bpy) adsorbs

according to the atomic symmetries of the substrate and aligns along the $[110]$ crystallographic direction in such a way that the two similar functional groups are always facing the same type of surface atoms (either Ni or O). Considering the partial charge distribution of the surface (Ni is $\delta+$ whereas O is $\delta-$), it is expected that the N atoms from the bpy domain are positioned on top of Ni atoms whereas the carboxylic acid groups adsorb on top of O atoms forming H-bonds with the surface.

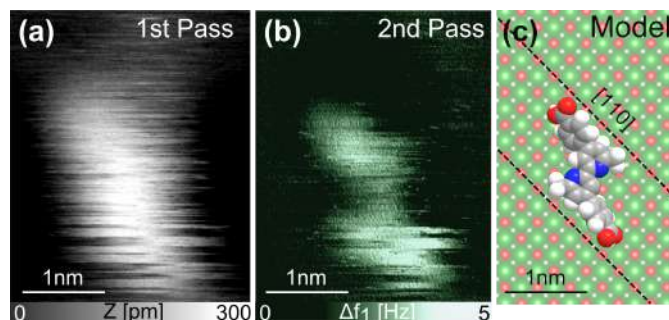


Figure 6.3: Single DCPDM(bpy) molecules on NiO(001) at RT. *a*, Topographic image of DCPDM(bpy) molecules adsorbed on the surface of NiO(001) acquired using the multipass scanning mode of AFM. the single molecule is imaged in the first scan pass. *b*, Frequency shift image recorded in the second scan pass on the same molecule, showing that DCPDM(bpy) adsorbed in its transoid-conformation. *c*, Model of transoid-DCPDM(bpy) on the surface of NiO(001). Scan parameters: $A_1 = 4$ nm, $\Delta f_1 = -2.5$ Hz, $z_{offset} = -350$ pm.

However, even at low coverage (0.2 ML), single molecules are relatively rarely observed. More often, DCPDM(bpy) appear to form clusters presenting a wind-mill shape as pointed by the red arrows visible in figure 6.4a. Similarly to what is observed for single molecules, this specific type of cluster appears to exhibit a preferential orientation along the atomic rows of the substrate. Figure 6.4b shows a close-up topographic image of such a cluster. This image recorded in the first scan pass of the multipass techniques clearly emphasizes that the windmill clusters consist of four distinct molecules. Because the measured height of the cluster appears to be the same than for single DCPDM(bpy), it can be concluded that the molecules composing the windmill clusters are also lying flat on the surface of NiO(001), implying that the adsorption geometry of the molecules is the same when adsorbing as a single molecule or when forming clusters. However, this can better be seen in the corresponding Δf_1 image (figure 6.4c) acquired in the second scan pass applying a z_{offset} of -350 pm, which unambiguously shows that the molecules are lying in their transoid conformation. Interestingly this image also highlights the fact that DCPDM(bpy) presents two distinct surface enantiomers. Indeed, molecules A, B and C exhibit the same form which can be obtained by 90° clockwise rotations with respect to each other whereas the form of molecule D cannot be obtained by any rotation of the other molecules. This can be related to the prochiral character of DCPDM(bpy). Indeed, like a large class of molecules, DCPDM(bpy), which is achiral in solutions or in the gas phase, becomes chiral after only one step, *i.e.* when confined in two dimensions [220–224]. Consequently as

shown in figure 6.4d, this leads to the appearance of two surface enantiomers: α and β . Considering the specific case of the cluster discussed above, molecules A, B and C are therefore α enantiomers whereas D is in the β form of DCPDM(bpy). The ratio $\alpha : \beta$ varies from cluster to cluster, suggesting that there is no preferred enantiomeric form of the molecule and thus implying that all over the total surface of the sample, this ratio should be 1:1.

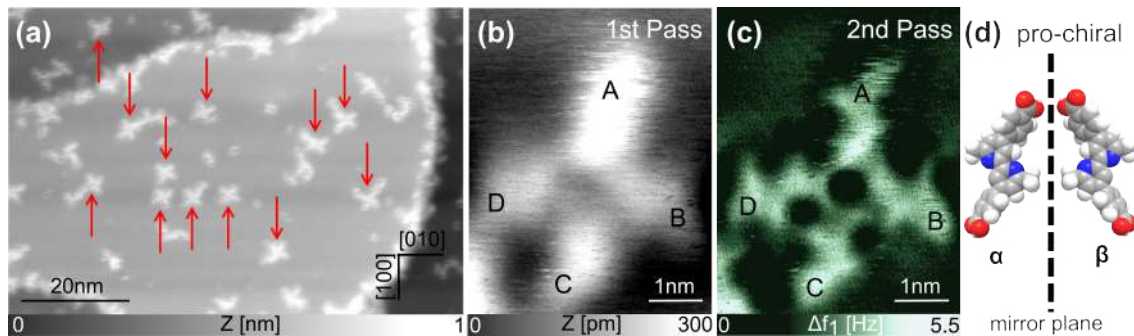


Figure 6.4: Windmill cluster on NiO(001) at RT. *a*, Topographic image of DCPDM(bpy) molecules forming a windmill shaped cluster (red arrows) on NiO(001). *b*, Topographic image of a cluster formed by 4 molecules (A, B, C and D) recorded in the first scan of the multipass technique. *c*, Frequency shift image acquired in the second scanning pass with an offset of -350 pm showing that DCPDM(bpy) adsorbs on NiO(001) with two distinct chiralities. *d*, Sketch presenting the prochiral character of DCPDM(bpy). Scan parameters: *a*: $A_1 = 4$ nm, $\Delta f_1 = -3$ Hz. *b-c*: $A_1 = 4$ nm, $\Delta f_1 = -2.8$ Hz, $z_{offset} = -350$ pm.

Contrary to what is observed at low molecular coverages, temperature drastically influences the interface morphology when the sample presents a higher molecular coverage. This is illustrated in figure 6.5 where a NiO surface covered with 0.8 ML of molecules is displayed. When this sample is imaged before annealing treatment, as shown in figure 6.5a, the surface of NiO is barely visible and almost completely covered with DCPDM(bpy) molecules packing in a random way. After annealing for 1h at 420 K, crystalline islands are observed on the terraces of the surface, whereas the step edges are saturated with disorganized molecules (figure 6.5b). The fact that island formation is observed only at higher coverage, implies that the molecules have to be really close to each other from the beginning to reorganize in crystalline assemblies after annealing. This confirms that the diffusion of DCPDM(bpy) on the surface of NiO(001) can be only slightly enhanced upon heat treatment. Interestingly, in contrast to what is usually observed at RT where molecular islands often undergo a step-flow growth process [165, 176, 231, 232], it appears in figure 6.5b that the DCPDM(bpy) islands exhibit the clear tendency to avoid growing from step edges. This might imply that adsorption at these specific sites is different than on the terraces. However, in order to confirm this hypothesis, high resolution imaging with submolecular accuracy at step edges is required. This could not be achieved so far because of the larger corrugations at these specific sites of the surface, resulting in scanning instabilities, which are not compatible with high resolution imaging.

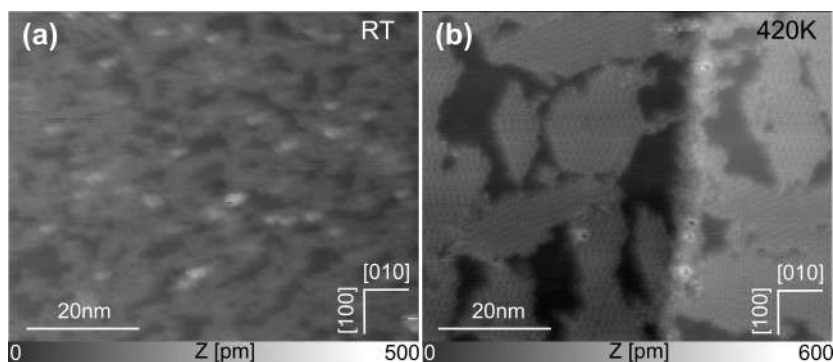


Figure 6.5: Annealing effect on the morphology of assemblies. *a* and *b*, Topographic images recorded on a NiO(001) surface covered with 0.8 ML of DCPDM(bpy) molecules before and after annealing treatment at 420 K, respectively. Scan parameters: *a*: $A_1 = 4$ nm, $\Delta f_1 = -9$ Hz. *b*: $A_1 = 4$ nm, $\Delta f_1 = -18$ Hz.

Figure 6.6a highlights two different orientations for the molecular islands. Both assemblies exhibit an identical height of 180 ± 20 pm. This supports the fact that, similar to single molecules adsorbed on the surface of NiO(001), DCPDM(bpy) are still lying flat in their transoid conformation and this independently of the island orientation. This can better be seen in figures 6.6b and 6.6c which are close-up topographic images of both structures overlaid with a tentative model representation. In the first assembly, presented in figure 6.6b, the DCPDM(bpy) molecules are aligned in vertical rows following the [100] direction of the substrate (orientation V) while they form horizontal rows extended in the [010] direction in the second (orientation H – figure 6.6c). From this images it can also be clearly seen that orientation V can be converted to H by operating an 90° rotation, and vice versa, which is consistent with the symmetries of the NiO(001) surface and also supports the expected alignment of the molecules along the $\langle 110 \rangle$ cristallographic directions of the substrate. Furthermore, the topographic images of figures 6.6b and 6.6c show that the molecules are arranged with alternating orientations within the islands, suggesting that every second molecule exhibits a different conformation. This probably results from the emergence of the prochiral character of DCPDM(bpy) after confinement on a surface. Indeed, this orientation alternation is related to the chiral α and β forms of DCPDM(bpy), implying that the ratio $\alpha : \beta$ is 1 : 1 as expected (see models in figures 6.6b and 6.6c). In addition, the models suggest that the DCPDM(bpy) interact with each other via H-bridging of their carboxylic groups.

Figure 6.6d represents the CPD recorded by KPFM simultaneously to the topographic image displayed in figure 6.6a [225]. Here it can be seen that the voltage needed for the compensation of electrostatic forces is the same for V and H islands, supporting that the adsorption geometry of DCPDM(bpy) is the same in both islands. In these areas, where molecules are self assembled, the absolute CPD value is increased in comparison to the surface of bare NiO, and the average CPD difference is measured to be $\Delta V_{CPD} = 180 \pm 30$ mV. However, in areas, such as step edges and certain zones of the terraces, where the molecular order and density are lower, the CPD contrast is

much weaker, evidencing that the arrangement into islands through H-bridging has a direct influence on the electrical coupling between the NiO surface and the molecular layer.

Because the CPD arises from the work function difference between the tip and the substrate, a higher absolute CPD value over the molecular layer can be directly related to a higher work function in these areas. This can, in turn, be attributed to more negatively charged molecular islands compared to the substrate and a dipole moment is pointing towards the surface. It is thought that the latter originates from a partial charge transfer directed from the surface to the molecular layer. Moreover, both quantities can be determined based on the measured CPD difference ΔV_{CPD} [62,63]. Indeed, starting from this value, the dipole moment density difference between the molecular layer and the surface of NiO can be calculated to be $\Delta p = 0.5 \text{ D/nm}^2$. Dividing this value by the molecular density ($D = 0.43 \text{ nm}^{-2}$), which can easily be extracted from the high resolution imaging, leads to an average dipole moment of 1.1 D per molecules. Assuming an effective substrate/molecule distance of 90 pm corresponding to half the height of an island [62], a partial charge transfer of $0.26 e^-/\text{molecule}$ can be calculated.

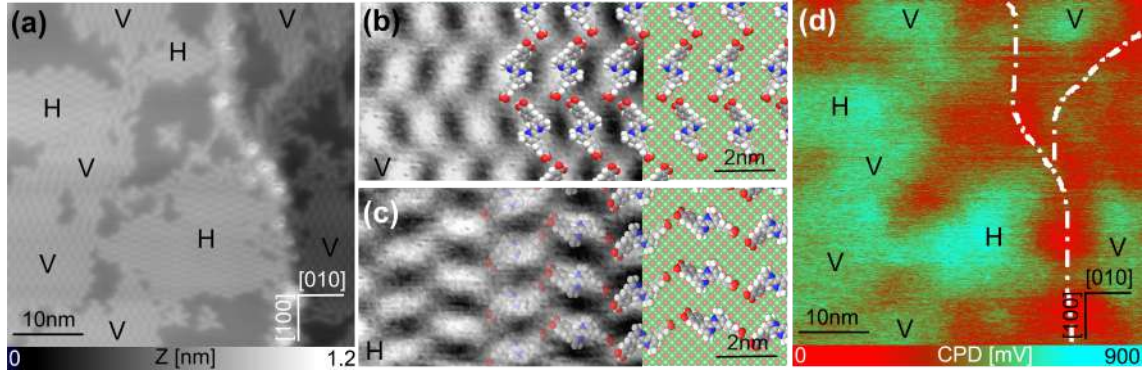


Figure 6.6: DCPDM(bpy) islands on NiO(001) at RT. *a*, Topographic image showing two possible orientation for molecular islands: H and V. *b*, Corresponding KPFM signal measured simultaneously. *c* and *d*, Close-up on V and H islands respectively. Models of the substrate and molecular layer are superimposed to the topographic measurements. Scan parameters: $A_1 = 4 \text{ nm}$, $\Delta f_1 = -9 \text{ Hz}$, $\omega = 900 \text{ Hz}$, $V_{AC} = 800 \text{ mV}$.

Interestingly the direction of this partial charge transfer (from the substrate to the molecular layer) is similar to what is observed for the p-type dye molecule C343, however its value is roughly 4 times larger (see section 5.3 in chapter 5). Furthermore, if calculated in function of active surface, DCPDM(bpy) appears to be about two times more efficient than C343 in terms of charge injection ($0.11 e^-/\text{nm}^2$ against $0.06 e^-/\text{nm}^2$). Knowing that DCPDM(bpy) is not a complete dye but only a precursor, one might expect that the intensity of this partial charge transfer can be further increased after assembly of the full dye, making it even more efficient and therefore much better adapted compared to C343 for the design of optimized DSSCs devices.

6.2.2 Metal complex formation on NiO(001)

In order to trigger the formation of a metal complex, a bare type 2 surface of NiO(001), with straight step edges running along the $\langle 110 \rangle$ directions of the substrate (see section 4.1 in chapter 4), is first of all covered with less than 0.1 ML of Fe atoms. This is shown in figure 6.7a where small Fe clusters are visible on the terraces of NiO. Figure 6.7b presents a topographic image of the same surface after additional deposition of 0.2 ML of DCPDM(bpy) molecules. Because of the low diffusion rate of DCPDM(bpy) on NiO(001), the metal is deposited first, and only then the molecules, with the prospect of observing the DCPDM(bpy) adsorbing directly on Fe atoms. However, in order to slightly favour the diffusion of molecules and thus the formation of metal complexes, the surface is annealed at 420 K while molecule's sublimation. Even if the molecules cannot be differentiated from the cluster atoms at large scale when comparing images 6.7a and 6.7b, there is no doubt about their presence since the surface coverage significantly increased from one image to the other. For instance, the step edges which are barely covered in presence of Fe atoms, are almost saturated after DCPDM(bpy) deposition.

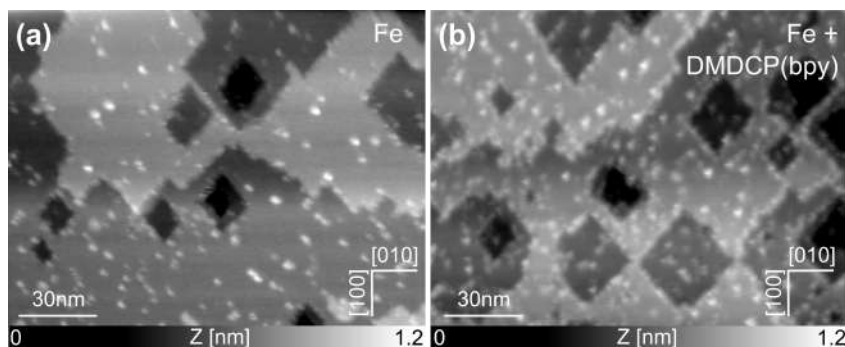


Figure 6.7: Successive Fe and DCPDM(bpy) depositions. *a*, Topographic image of NiO(001) covered with less than 0.1 ML Fe atoms *b*, Topographic image of the same surface after additional deposition of 0.2 ML of DCPDM(bpy) molecules. Scan parameters: *a*: $A_{f_1} = 4$ nm, $\Delta f_1 = -9$ Hz. *b*: $A_1 = 4$ nm, $\Delta f_1 = -10$ Hz.

Figure 6.8a is a topographic image of a single molecule acquired at RT on a terrace of NiO covered with Fe atoms in the first scan pass of the multipass method. Comparably to what has been observed for non metal bounded objects, this image emphasizes that single molecules are lying flat on the substrate also when it is functionalized with Fe atoms. Nevertheless, because the tip/sample separation is relatively large here, the shape of the present protrusion is attributed to tip asymmetry rather than to submolecular contrast. However, its adsorption geometry in a cisoid conformation is revealed in the Δf_1 image, recorded in the second scan pass at lower tip/sample distance ($z_{offset} = -280$ pm), shown in figure 6.8b and sketched in the model of figure 6.8c. Even if the Fe atom is not visible in the image, and because the transoid conformation of DCPDM(bpy) is stable even after annealing at 420 K, the observed cisoid conformation is assigned to the formation of a metal complex (see figure 6.1) and the object imaged here is therefore related to Fe-DCPDM(bpy).

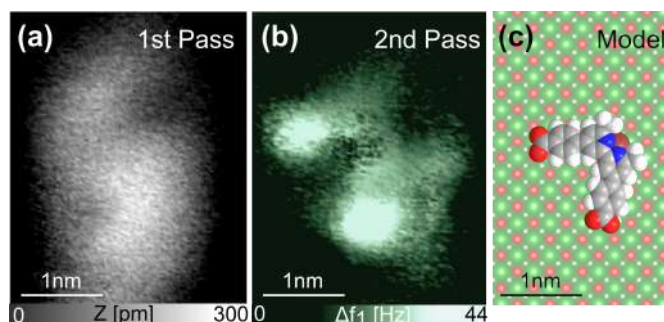


Figure 6.8: Single Fe-DCPDM(bpy) molecules on NiO(001) at RT. *a*, Topographic image of a single supposed Fe-DCPDM(bpy) molecule adsorbed on a NiO(001) terrace acquired in the first scanning pass of the multipass mode of AFM. *b*, Frequency shift image recorded in the second scan pass on the same molecules, showing that Fe-DCPDM(bpy) is lying in a cisoid conformation. *c*, Model of cisoid-Fe-DCPDM(bpy) on the surface of NiO(001). Scan parameters: $A_1 = 4$ nm, $\Delta f_1 = -29$ Hz, $z_{\text{offset}} = -280$ pm.

Nonetheless, to firmly confirm the systematic switching from the transoid conformation of DCPDM(bpy) to the cisoid form of Fe-DCPDM(bpy) through metal coordination, a more statistical study is needed. For technical reasons, such a study, where intramolecular resolution is mandatory to state the adsorption geometry of single molecules, is difficult at RT. Indeed, it has been shown earlier that this quality of imaging cannot be reached at large scale but only when single molecules are imaged applying the multipass technique, which is a tricky and time consuming method, especially because molecules cannot be distinguished from Fe clusters at large scales.

6.3 On-surface synthesis on Au(111)

To improve the resolution, but also to emphasize that the switching reaction is triggered by Fe coordination, the study of the adsorption of DCPDM(bpy) as well as the formation of the metal complex Fe-DCPDM(bpy) on Au(111) by low temperature (LT) STM and AFM with a CO-terminated tip [54], is presented in this section. Even if Fe atoms cannot be directly imaged, their primordial role is evidenced thanks to statistical investigation by high resolution STM imaging at LT combined with X-ray photoelectron spectroscopy (XPS) measurements.

6.3.1 Dye precursor anchoring on Au(111)

Compared to NiO(001), the Au(111) surface is prepared with comparable DCPDM(bpy) dye precursor coverage (0.2 ML on NiO against 0.1 ML on Au). In these conditions, at 4.7 K, most of the molecules appear to lie in a transoid conformation, confirming that DCPDM(bpy) adsorbs in the same geometry on Au(111) than on NiO(001). The structure of one of those molecules is resolved by LT STM imaging as shown in figure 6.9a and the corresponding constant-height AFM image is displayed in figure 6.9b. In the

latter image, the phenyl rings, the carboxylic groups, as well as the methyl groups attached to the bpy unit of the molecules, can unambiguously be identified, confirming the flat lying geometry of the molecules similarly to what is observed at RT on NiO(001) (see model of figures 6.9c and figures 6.9d).

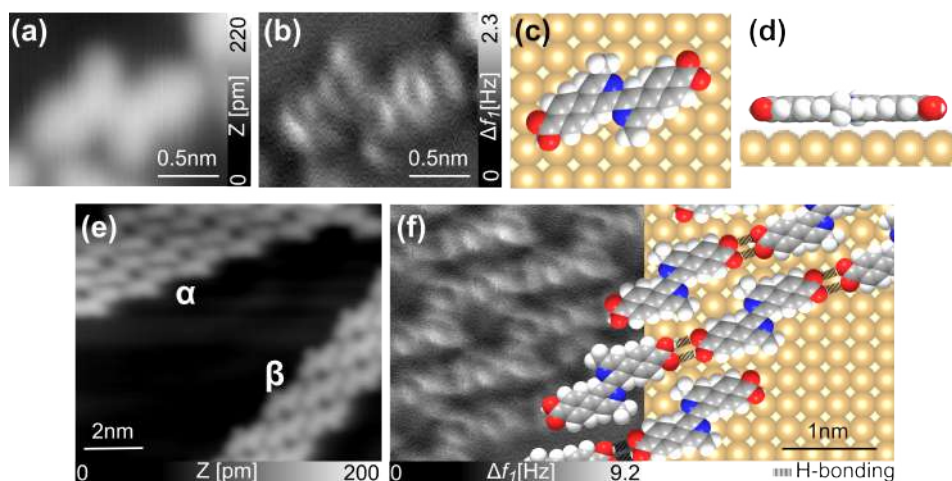


Figure 6.9: The transoid configurations of DCPDM(bpy) imaged at LT. *a*, Topographic STM image of a single DCPDM(bpy) molecule in transoid conformation adsorbed on Au(111). *b*, corresponding constant height AFM image showing the same molecule with intramolecular resolution. *c*, and *d*, Corresponding tentative models. *e*, Topographic STM image of molecular assemblies formed by DCPDM(bpy) adsorbed on Au(111). The prochiral character of the molecules leads to two types of structures: α and β . *f*, corresponding constant height AFM image showing an α assembly with submolecular resolution and a superimposed tentative model. Scan parameters: *a*, *e*: $I_t = 1$ pA, $V_{BIAS} = -0.15$ V. *b*, *f*: $A = 50$ pm, $V_{BIAS} = 0$ V.

However, because the diffusion rate of DCPDM(bpy) on Au(111) is higher than on NiO(001), large assemblies can be observed on the surface upon adsorption at RT even at low coverage (~ 0.1 ML) as shown in figure 6.9e. The prochiral character of DCPDM(bpy), which has been discussed earlier and could be observed on NiO(001), can also be evidenced on Au(111). Indeed, figure 6.9e emphasises the presence of two distinct domains formed by either α - or β -DCPDM(bpy) molecules (see figure 6.4d). Importantly, and in contrast to what is observed on NiO surfaces for higher coverages, molecular domains do not present an alternating arrangement of both chiralities. In other words, the gold substrate acts as a catalyst for the formation of enantiopure supramolecular structures. Figure 6.9f is a close up constant height AFM image acquired on top of an α assembly overlaid with a tentative model. This figure emphasises that the formation of the extended close-packed molecular domains is driven by the formation of H-bonding between the carboxylic groups of adjacent enantiomers.

6.3.2 Metal complex formation on Au(111)

After the surface of Au(111) is covered with DCPDM(bpy), less than 0.1 ML of Fe atoms are deposited onto the same surface. To trigger the formation of metal complexes, the sample is annealed for 30 min at 420 K. As a result of this preparation process, a large majority of the molecules present on the substrate adopt a cisoid geometry implying a metal coordination between the N atoms of their bpy domain and a Fe adatom. The structure of Fe–DCPDM(bpy) is imaged by LT STM (figure 6.10a) and constant height AFM with a CO terminated tip (figure 6.10b). The latter reveals the cisoid conformation of the metal complex with intramolecular accuracy. Contrary to the phenyl rings and the methyl groups of the bpy unit that can clearly be observed in this image, the metal atom is not visible. This is, however, not surprising since it is well known that metal atoms are generally difficult to observe by AFM while imaging metal–ligand complexes at surfaces [167, 233–235]. Nonetheless, the fact that methyl groups of the bpy unit appear brighter in comparison to carboxylic acid groups which are not visible, implies that the tip is in closer vicinity to the metal binding domain than to the anchoring groups while scanning the molecule. This, in turn, suggests that the carboxylic groups are closer to the surface than the other parts of the molecule, meaning that the latter is not lying completely flat on the substrate like DCPDM(bpy) but is slightly bent. This might be explained by the fact that the Fe atom partially intercalates in between the molecule and the substrate as shown in the models displayed in figures 6.10c and 6.10d.

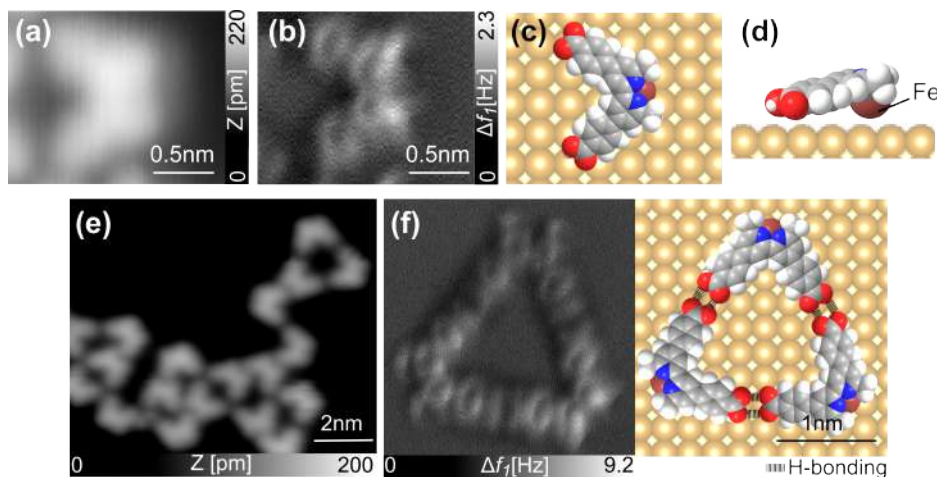


Figure 6.10: The cisoid configurations of Fe–DCPDM(bpy) imaged at LT. **a**, Topographic STM image of single a Fe–DCPDM(bpy) molecule in cisoid conformation adsorbed on Au(111). **b**, Corresponding constant height AFM image showing the same molecule with intramolecular resolution. **c**, and **d**, Corresponding tentative models. **e**, Topographic STM image of a molecular structure formed by Fe–DCPDM(bpy) adsorbed on Au(111). The achiral character of the molecules leads to only one type of structure. **f**, Constant height AFM image showing an assembly of three molecules with submolecular resolution and its corresponding tentative model. Scan parameters: **a**, **e**: $I_t = 1$ pA, $V_{BIAS} = -0.15$ V. **b**, **f**: $A = 50$ pm, $V_{BIAS} = 0$ V.

Unlike the chiral domains formed by DCPDM(bpy), the supramolecular structures originating from Fe-DCPDM(bpy) are fully achiral (Figure 6.10e). However, in the constant height AFM image and its corresponding model displayed in figure 6.10f, it can be seen that the emergence of this type of network is governed by the same interaction than what is observed for DCPDM(bpy) islands, *i.e.* H-bonding between the carboxylic groups of two neighbouring molecules. Consequently, even though Fe atoms do not directly participate in intermolecular interactions, they are essential for the formation of this type of achiral networks because they are responsible for the upkeep of the molecules in a cisoid conformation. Conclusively, Fe coordination leads not only to the formation of a metal complex but also to the suppression of the prochiral character of specific molecular domains. The control of this chiral to achiral transition at a surface might be the starting point for the future design of molecular compounds that could be used as chiral switches in molecular electronics.

6.3.3 The role of Fe adatoms for the reaction

In the previous mentioned experiment, the conformation switch arises not only when Fe adatoms are brought in contact with the DCPDM(bpy) molecules, but also after annealing at 400 K to activate the transition. So, in order to attribute unambiguously this switching to Fe coordination and not only to annealing, the reaction is further investigated.

The conformation ratio (transoid:cisoid) in function of the sample preparation, at 0.1 ML coverage of DCPDM(bpy), is determined by statistical analysis of a set of several STM images and is summarized in table 6.1. Upon RT deposition, almost all DCPDM(bpy) adsorb on the surface of Au(111) in their transoid conformation and the conformation ratio is 91:9 (see figure 6.11a). As already mentioned, Fe deposition followed with surface annealing results in an inversion of this ratio (3:97), meaning that a large majority of molecules are in a cisoid conformation (see figure 6.11b). In contrast, when driven exclusively by thermal annealing, only around half of molecules undergo a conformation change and the transoid:cisoid ratio becomes 52:48 (figure 6.11c). Furthermore, it is pointed by black arrows in figure 6.11c that most of the molecules that switched to a cisoid geometry are sitting on the elbows or edges of the gold reconstruction, which are known to be reactive sites where a coupling to the surface is possible [236]. For this reason it is expected that this transoid:cisoid ratio can be increased for higher molecule coverage since it will lead to the saturation of those reactive sites. In conclusion, the switching process can be facilitated or hindered as a function of the underlying substrate. In other words, metallic surfaces are logically playing a catalytic role for the formation of metal complexes. Table 6.1 summarises the conformation ratio as a function of the sample preparation.

To evidence the role of Fe adatoms, similar samples are prepared with higher molecular coverage (close to 1 ML) and the N1s binding energies (BE) of the molecules on Au(111) are measured by X-ray photoelectron spectroscopy (XPS) (figure 6.11c). This allows to reveal the chemical environment of the bpy unit of the molecules and therefore to emphasize if they are coordinated to Fe atoms. After deposition of ~ 1 ML of DCPDM(bpy) on Au(111), the N1s BE is measured to be 398.2 eV (green curve).

6.3. On-surface synthesis on Au(111)

	without Fe without annealing	with Fe with annealing	without Fe with annealing
transoid	91%	3%	52%
cisoid	9%	97%	48%

Table 6.1: Effect of Fe and annealing on the conformation of DCPDMBpy.

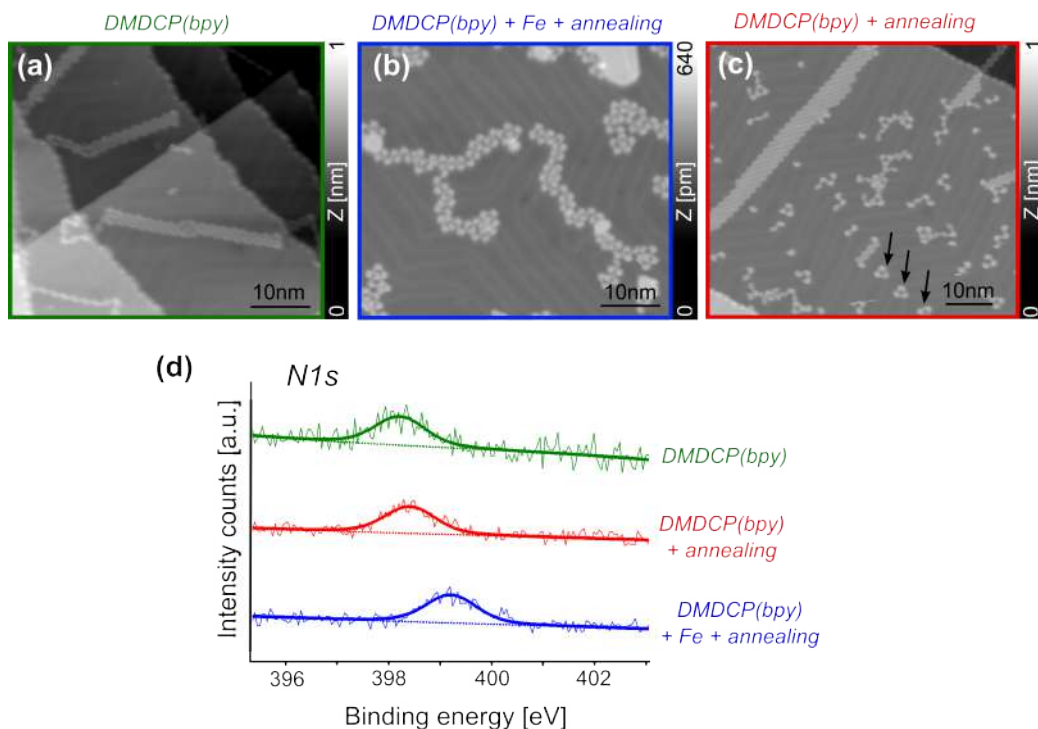


Figure 6.11: Effect of annealing and metal coordination. *a–c*, STM images of 0.05 ML DCPD(bpy) on Au(111) adsorbed at room temperature (green), after annealing at 400 K (red) and after annealing at 400 K and Fe deposition (blue). *d*, Comparable XPS spectra of 1 ML DCPD(bpy) deposited on Au(111) following the same preparation processes. The shown spectra are normalized and shifted vertically for comparison.

When complex formation is governed by Fe deposition and activated by temperature, the N1s shifts by 1 eV towards higher energies ($BE = 399.2$ eV, blue curve) supporting the expected coordination of the bpy moieties with an Fe adatom [237,238]. In contrast, upon temperature activation in absence of Fe adatoms, the N1s BE shifts only by 0.2 eV ($BE = 398.4$ eV, red curve). In correlation with STM images, it is thought that this smaller shift originates from the fraction of DCPD(bpy) molecules that have formed complexes through metal coordination at specific sites of the Au(111) substrate. Because there is only a limited amount of these sites, the formation of the Au–DCPD(bpy) is less efficient. However, the low signal-to-noise ratio, which is due to the small amount of molecules (less than 1 ML) does not allow a proper deconvolution of the N1s peak arising from transoid–DCPD(bpy) and cisoid–Au–

DCPDM(bpy).

6.4 Summary

In this chapter the first steps of an on–surface reaction, which is commonly used for the design of p–type DSSCs was studied. In a first part, the reaction was discussed and the involved products were described. By investigating the adsorption of the dye precursor DCPDM(bpy) and the formation of the corresponding metal complex Fe–DCDM(bpy) on the surface of NiO(001) and Au(111) by RT nc–AFM and LT STM/AFM, respectively, it was shown that the reaction is independent from the underlying substrate. On both surfaces, DCPDM(bpy) exhibited the clear tendency to preferentially adsorb in a flat lying transoid conformation. However, it was evidenced that, because of higher diffusion, the formation of large assemblies is facilitated upon deposition on a gold surface. Indeed, whereas molecular networks were observed directly after low coverage DCPDM(bpy) deposition at RT on Au(111), the formation of molecular islands took place only at higher coverage and after activation by annealing at 420 K on the NiO(001). Furthermore, it has been observed that DCPDM(bpy) become prochiral after deposition on a surface. As a consequence, the molecular island observed on NiO(001) appear to be composed of molecules with alternating chiralities, while in contrast, the domains formed on Au(111) are enantiopure. However, it is thought that the emergence of both types of islands is governed by the formation of H–bonding between the carboxylic groups of neighbouring molecules. In the case of NiO, it was also shown that these interactions are responsible for the electrical coupling between the surface and the molecular layer and a partial charge transfer of 0.26 electrons per molecule from the first toward the second was observed. Upon contact with Fe atoms, the molecule switched its conformation from transoid to cisoid. The structure of the so formed molecules was observed on both surfaces with submolecular resolution. AFM and STM measurements, as well as at RT and LT, could not clearly state the presence of Fe atoms in this cisoid molecule. However, thanks to statistical analysis of high resolution images combined with XPS measurements, the conformation switch could unambiguously be attributed to metal coordination, therefore evidencing the formation of the corresponding metal complex.

Functionalization through Spray Deposition

SURFACE sensitization of NiO can occur following several preparation methods, such as molecular evaporation or on-surface synthesis, which are compatible with imaging at the submolecular scale. However, these deposition techniques are reserved to a restricted class of molecules. Indeed, a large majority of dyes, can neither be sublimated nor assembled directly on surfaces because of their thermal fragility and structural complexity. In order to overcome this limitation, it is shown here, that NiO can be functionalized with large dye molecules via electrospray deposition (ESD), delivering surfaces that fulfil the cleanliness requirements needed to resolve the samples with submolecular accuracy. In a first part, the choice of the studied molecules is discussed and their chemical structures are described. The well studied C₆₀ molecules are then used as reference molecules in order to probe the reliability of the ESD technique on a NiO surface. To finish, three different dyes are imaged by nc-AFM and their structure is revealed with submolecular resolution.

7.1 Motivation

Since He *et al.* proposed the first prototypical p-type DSSCs in 1999, several studies focused on the optimization of this type of devices [7, 9, 219, 239]. However, it is only during the past decade, that significant progresses have been made in terms of efficiency by designing sensitizers that are better adapted to the function of p-type DSSCs. Indeed, from 2008, Qin *et al.* imposed their prototypical dye, 4-(Bis-{4-[5-(2,2-dicyano-vinyl)-thiophene-2-yl]-phenyl}-amino)-benzoic acid (P1) (see figure 7.1), as a reference molecule for further investigations [217, 240–243]. P1 consists in a triphenylamine unit linked on one side to an carboxylic acid anchoring domain and on the other side to two malononitrile moieties. Contrary to organic dyes used for the design of n-type DSSCs, the anchoring part of the molecule is located on the HOMO side (*i.e.* the electron donor part) of the molecule resulting in an electron flow from the semiconductor towards the molecule upon light adsorption. Nonetheless, recently, ruthenium based dyes with similar properties have been investigated and it has been

shown that they outperform the reference dye P1 [27]. These sensitizers, namely the zwitterionic dye $[\text{Ru}(\text{bpy})_2](\text{H1})$ and the salt $[\text{Ru}(\text{bpy})_2](\text{H2})[\text{PF}_6]$ are shown in figure 7.1. Both dyes consists in a Ru core linked to two bpy units and to a 4-(2-phenylpyridin-4-yl)phenyl)phosphonic acid group (H1) or a (4-(2-phenylpyridin-4-yl)phenyl)carboxylic acid group (H2), respectively. Comparing both dyes showed that binding the sensitizer to a NiO working electrode through a phosphonic acid group leads to improvement of the device performance and stability in comparison to the carboxylic acid anchoring domain.

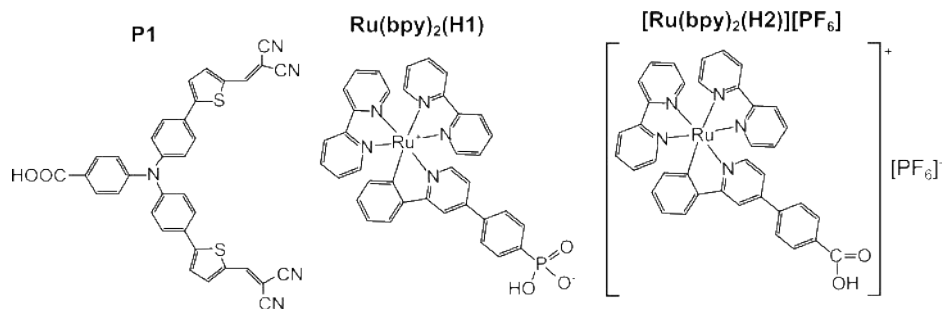


Figure 7.1: Structures of P1, $\text{Ru}(\text{bpy})_2(\text{H1})$ and $[\text{Ru}(\text{bpy})_2(\text{H2})][\text{PF}_6]$. All three molecules can be used for the design of *p*-type DSSCs.

Although P1, $\text{Ru}(\text{bpy})_2(\text{H1})$ and $[\text{Ru}(\text{bpy})_2(\text{H2})][\text{PF}_6]$ are of paramount interest in the context of DSSCs, their structures have not been investigated up to now by the means of any SPM technique. The main reason being probably the difficulty of preparing a sample which fulfills the cleanness requirements needed to perform nanoscale imaging. Indeed, because of their complex chemical structures and their fragility, these dyes, cannot be thermally evaporated onto the surface of NiO(001). Thus, the only possibility to prepare a sample that is compatible with UHV measurements relies on ESD. The latter method was reported to deliver clean interfaces where large organic molecules exhibit intact structures when deposited on the clean surfaces of alkali halides or metallic samples [74, 75]. However, there are no reported studies focusing on the functionalization of NiO using ESD so far. Therefore, the content of this chapter, opens the path to the preparation of new interfaces, which were not accessible until today.

7.2 C_{60} as a reference molecule

Until now, ESD followed by SPM imaging was exclusively performed on metallic or alkali halide samples [74, 75, 244–246]. During the past two decades, this method was also used for the preparation of sensitized TiO_2 samples. However, these interfaces were not imaged by STM or AFM [247–250], suggesting that their preparation using ESD results in surfaces that are not fulfilling the cleanliness requirements needed to perform SPM imaging. Nowadays, other functionalized metal oxides, such as sensitized NiO, prepared via ESD are not reported in the available literature. Nonetheless, because the Buckminsterfullerene or C_{60} became one of the most intensively studied molecule in the

field of SPM since its discovery in 1985 by Kroto *et al.* [251], it presents an excellent reference molecule to test the reliability of the ESD method for the preparation of functionalized NiO samples.

The structure of C_{60} is given in figure 7.2. It consists of 60 carbon atoms which are all linked to three other atoms through one double bond and two single bonds. In that way, all the valences of the structure are satisfied leading to a superstable molecule. Because C_{60} is a polygon that is composed of 12 pentagonal and 20 hexagonal faces sharing 60 vertices, it is often compared to a football with a diameter of 1 nm [251]. Considering its structural simplicity, the adsorption of C_{60} has been investigated on numerous surfaces and submolecular contrast has been obtained at LT using STM [252–254] as well as nc-AFM [255–257], during the past years. After sublimation, and when imaged at RT, it has been demonstrated that C_{60} molecules form 2D layers on the surface of metals [258–260], and semiconductors, such as TiO_2 [165, 166] or Si [261, 262]. In contrast, it has been observed that the same molecules form large 3D molecular islands and clusters when deposited on the surface of insulators [232, 263–271]. Under certain conditions, when the substrate presents enough reactive sites, C_{60} can also adsorb as single molecule. This has, for instance, been observed on the surface of several Si reconstructions [272–274]. In addition, it has also been demonstrated that C_{60} molecules are good candidates for spray deposition methods [244, 275, 276].

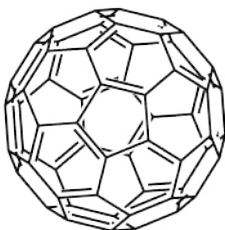


Figure 7.2: Chemical structure of C_{60} . *Because of its simplicity and stability, the Buckminsterfullerene molecule is one of the most studied in the field of SPM.*

However, despite the considerable amount of studies dedicated to the investigation of C_{60} by SPM methods, the metal oxide NiO(001) has, so far, never been functionalized with any fullerene molecules, neither through sublimation, nor via spray deposition. Consequently we present here a comparison of both preparation methods in order to show the reliability of the ESD technique.

Figure 7.3a presents a large scale topographic image of the surface of NiO(001) functionalized with C_{60} molecules via sublimation. Large 2D molecular islands, which present irregular shapes, and are various sizes, comparably to what has been observed earlier on the surface of TiO_2 [165], are visible on terraces of the substrate. Even though these islands are varying in width, they exhibit a constant height of one layer of molecules. Figure 7.3b shows a close up topographic image acquired above one of those molecular domains. Interestingly the height of the island is measured to be about 300 pm instead of 1 nm as theoretically expected. This was attributed to the fact that the surface charges were compensated only locally, instead of measuring in a KPFM

mode, which can strongly affect the measured height of molecular domains. However, because the size of the observed protrusions (~ 1 nm) is fitting with the diameter of C_{60} and because a hexagonal packing of the molecules is observed, the islands can unambiguously be attributed to C_{60} domains.

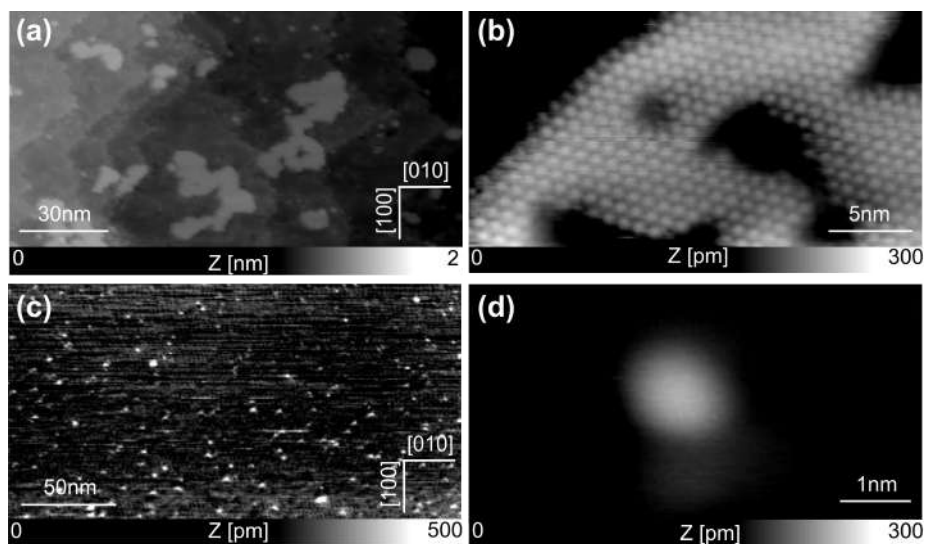


Figure 7.3: Comparison between sublimation and spray deposition for the functionalization of $NiO(001)$ with C_{60} molecules. *a*, Large scale topographic image of C_{60} molecules adsorbed on the surface of $NiO(001)$ after sublimation. *b*, Close up topographic image of the same surface showing an 2D island formed by the C_{60} molecules. *c*, Large scale topographic image of C_{60} molecules adsorbed on the surface of $NiO(001)$ after spray deposition. *d*, Close up topographic image of the same surface showing a single C_{60} molecule. Scan parameters: *a*: $A_1 = 8$ nm, $\Delta f_1 = -5$ Hz. *b*: $A_1 = 8$ nm, $\Delta f_1 = -12$ Hz. *c*: $A_1 = 4$ nm, $\Delta f_1 = -15$ Hz. *d*: $A_1 = 5$ nm, $\Delta f_1 = -25$ Hz.

Comparably to figure 7.3a, the large scale topographic image displayed in figure 7.3c shows the surface of $NiO(001)$ covered with C_{60} molecules, except that the latter were deposited via ESD instead of evaporation. Obviously, the surface presented here, exhibits a different morphology compared to the sample described above, demonstrating that different preparation methods can lead to different interfaces. Indeed, whereas molecular domains are formed after the molecules are sublimated onto the surface of $NiO(001)$, the spray deposition method results in a surface covered with single molecules. This can be seen in figure 7.3c where numerous protrusions, whose size is fitting to the diameter of C_{60} , are observed. In addition, the prevalence of noise lines, highlighting the slight instability of the scanning conditions, suggests the presence of remaining solvent molecules. However, because these undesirable molecules have a size that is smaller than the diameter of C_{60} (100 pm for MeOH and 600 pm for toluene), they can be clearly distinguished from each other. Consequently, because of its measured diameter of ~ 1 nm, the protrusion visible in figure 7.3d is attributed to a single C_{60} molecule. Furthermore, this is also confirmed by the fact that the height of the present

object is measured to be the same as the height of the molecular domain formed by fullerene molecules and displayed in figure 7.3b.

The most plausible argument to explain the interface morphology dissemblance when using different preparation methods, is the possibly increased amount of defects when ESD is employed. This is supported by a recent work, where it has been observed that large craters can be formed through bombardment of the surface with molecules, solvent or even unpumped droplets, during ESD [277]. However, even though large defects are not observed in this case, one can reasonably assume that ESD can also induce smaller defects that are acting as trapping sites for the molecules [164,194,202–208], leading to a surface where single C₆₀ can be observed.

Consequently, even though it was demonstrated in this section that ESD can be used on NiO(001) for the preparation of clean sensitized surfaces, this method also appears to be relatively invasive. Thus, it results in interfaces that present a different morphology than what is observed after molecule sublimation.

7.3 Complex dye molecules imaging

In this section, ESD is used as an experimental method for the deposition of large dye molecules which are not compatible with sublimation or cannot be assembled directly on surfaces. It is shown that ESD of these molecules results in samples that are clean enough to be imaged by the means of nc-AFM under UHV conditions. However, the difficulty of imaging single molecules with complex structures as well as the limitation of the deposition method are also addressed.

7.3.1 The reference P1 dye molecule

In a first experiment, the reference molecules P1 are deposited via ESD onto a clean surface of NiO(001). The large scale topographic image of figure 7.4a shows a NiO(001) surface after spray deposition of P1 molecules. This sample exhibits large terraces separated by monoatomic step edges, demonstrating that ESD delivers surfaces with comparable cleanliness to samples prepared via molecule sublimation, even in the case of a metal oxide. In this image it can also be seen that P1 adsorbed preferentially at step edges. Few molecules are also visible on terraces. Larger adsorbates are related to molecular clusters (red arrows), whereas the regular size (~ 2 nm) of the smaller objects (green arrows), which is fitting with the expected size of P1, indicates the presence of single molecules. In addition, since ESD was proven to not damage the structure of complex molecules [75], the further residues that exhibit an even smaller size compared to the P1 dye (blue arrows) are attributed to solvent molecules (MeOH has an expected width of roughly 100 pm and toluene is about 600 pm). However, the stable and well defined image shown in figure 7.4a, indicates that these remaining traces of solvent do not disturb the imaging.

Figure 7.4b and 7.4c show a single P1 molecule imaged in the first and second pass of the multipass method, respectively. From the height of the molecule (~ 200 pm) measured in the topographic signal, it can be deduced that P1 adsorbs in a more

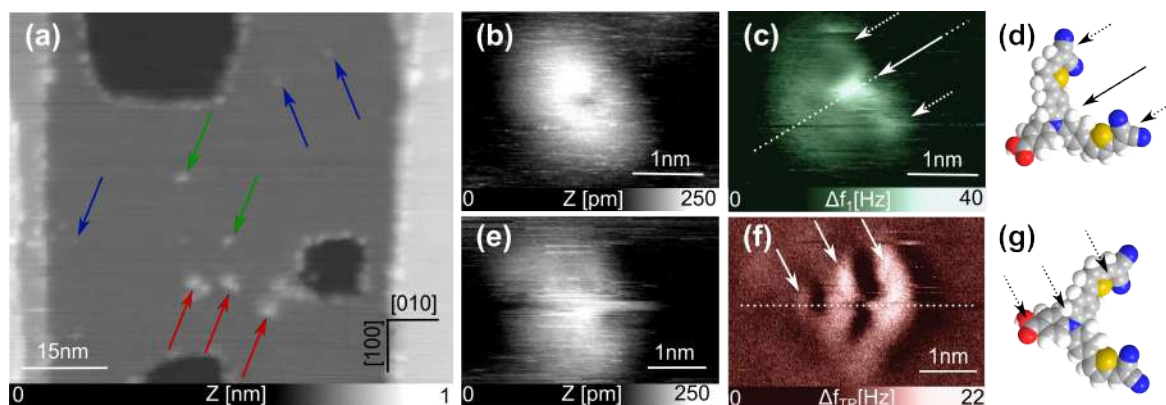


Figure 7.4: The reference dye molecule P1. *a*, Large scale topographic image of P1 molecules adsorbed on the surface of NiO(001) *b*, Close up topographic signal acquired using the multipass scanning mode of AFM. The single molecule is imaged in the first scan pass. *c*, Frequency shift image recorded in the second scan pass on the same molecules, showing the symmetric shape of P1. *d*, Corresponding tentative model. *e*, Different P1 molecule imaged in the topographic mode. *f*, Simultaneously acquired torsional signal emphasizing the symmetrical shape of P1. Different P1 molecule imaged in the topographic mode. *g*, Corresponding tentative model. Scan parameters:*a*: $A_2 = 400$ pm, $\Delta f_2 = -25$ Hz. *b*, *c*: $A_2 = 800$ pm, $\Delta f_2 = -28$ Hz, $z_{offset} = -300$ pm. *e*, *f*: $A_2 = 400$ pm, $A_{TR} = 80$ pm, $\Delta f_2 = -38$ Hz.

or less flat lying geometry on the surface NiO(001). The heterogeneous contrast of the frequency shift signal recorded in the second line scan while applying an offset of -300 pm gives a better insight of the structure of the molecule. Indeed, even if the structure cannot be resolved unambiguously, it can be seen that the object imaged here exhibits an axial symmetry that is oriented along the white dotted line of figure 7.4c. This symmetry, which can be directly related to the shape of P1, is translated into a brighter spot (white full arrow) surrounded by two equally distributed darker lobes (white dotted arrows). The latter are related to the triphenylamine unit and the malononitrile moieties of the molecule, respectively, as shown in the tentative model displayed in figure 7.4d. The last darker unit that is located in line with the white full arrow, is associated to the carboxylic acid anchoring domain of P1. Furthermore, imaging a second molecule in another scanning mode confirms the expected symmetric shape of the dye. As for figure 7.4b, the topographic image presented in figure 7.4e indicates the flat lying adsorption of P1. The corresponding torsional signal (figure 7.4f) recorded simultaneously, emphasizes the axial symmetry of the molecule (white dotted line). In this image three distinct lobes that are increasing in size from left to right can be related to the different parts of the molecule (see tentative model of figure 7.4g). However, neither the multipass method, nor torsional AFM mode, allow to resolve clearly the structure of the molecule. This is probably due to the flexibility of the side groups of P1 and therefore to a non fully planar adsorption geometry, but also to the fact that the measurements are performed at RT, leading to scanning instabilities which translate into noise lines that are visible in all the close up images.

7.3.2 The prototypical Ruthenium dyes

In a second experiment, ESD is used to study the adsorption of the prototypical dyes $\text{Ru}(\text{bpy})_2(\text{H1})$ and $[\text{Ru}(\text{bpy})_2](\text{H2})[\text{PF}_6]$, which were recently used for the fabrication of DSSCs devices [27], on the surface of $\text{NiO}(001)$.

Figure 7.5a shows a large scale topographic image of $\text{NiO}(001)$ covered with $\text{Ru}(\text{bpy})_2(\text{H1})$. This image reveals the preferential tendency of the sensitizers to adsorb as single molecules on reactive sites such as step edges and line defects. The surface coverage is measured to be ~ 0.08 ML. In addition, the pretty regular size of the adsorbates, which is fitting with the expected width of $\text{Ru}(\text{bpy})_2(\text{H1})$ (~ 1.5 nm), strongly suggests the absence of solvent molecules, resulting in more stable imaging conditions in comparison to P1. The close up topographic image displayed in figure 7.5b presents a single molecule imaged in the first line scan of the multipass technique. When imaged in the second scanning pass while reducing the tip/sample distance by -600 pm, the structure of $\text{Ru}(\text{bpy})_2(\text{H1})$ is revealed (figure 7.5c). Because of its 3D geometry (see figure 7.5d), it is hard to state concerning the exact adsorption of the molecule. However, in the frequency shift image, one clearly distinguishes the presence of several carbon rings, as pointed by the white arrow in figure 7.5c, which can be related to the structure of the molecule.

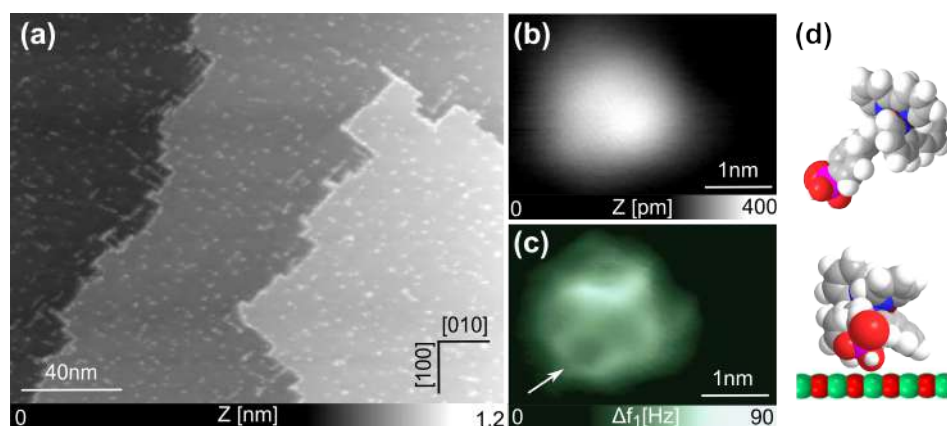


Figure 7.5: The zwitterionic dye $\text{Ru}(\text{bpy})_2(\text{H1})$ adsorbed on NiO . *a*, Large scale topographic image of $[\text{Ru}(\text{bpy})_2](\text{H1})$ molecules adsorbed on the surface of $\text{NiO}(001)$. *b*, Close up topographic signal acquired in the first scanning pass of the multipass technique showing a single $[\text{Ru}(\text{bpy})_2](\text{H1})$. *c*, Frequency shift image recorded in the second scan line on the same molecules while applying an offset of -600 pm, partially resolving the structure of $[\text{Ru}(\text{bpy})_2](\text{H1})$. *d*, Model of a single $[\text{Ru}(\text{bpy})_2](\text{H1})$ revealing the 3D adsorption geometry of the dye. Scan parameters: *a*: $A_1 = 4$ nm, $\Delta f_1 = -27$ Hz. *b-c*: $A_1 = 4$ nm, $\Delta f_1 = -13$ Hz, $z_{\text{offset}} = -600$ pm.

Figure 7.6a shows a large scale topographic image of $\text{NiO}(001)$ after spray deposition of a solution of $[\text{Ru}(\text{bpy})_2(\text{H2})][\text{PF}_6]$. The main difference between this dye solution and the one containing $\text{Ru}(\text{bpy})_2(\text{H1})$, is the presence of $[\text{PF}_6]^-$ anions. However, because of their small size (~ 350 pm), which lies in the same range than the size of the solvent molecules, it can reasonably be assumed that they are pumped during deposition and

that they are therefore not present on the surface of NiO(001) at the end of the process. This hypothesis is also supported by the stable scanning conditions of image 7.6a, where no noise lines are observed. Thus, in the following, $[\text{Ru}(\text{bpy})_2(\text{H2})][\text{PF}_6]$ refers the dye solution before deposition and $\text{Ru}(\text{bpy})_2(\text{H2})$ stand for the dye molecules once they are deposited on the surface of NiO(001). So, after deposition, the main difference between both interfaces is actually the anchoring group of the dye (phosphonic acid in the case of $\text{Ru}(\text{bpy})_2(\text{H1})$ and carboxylic acid in the case of $\text{Ru}(\text{bpy})_2(\text{H2})$).

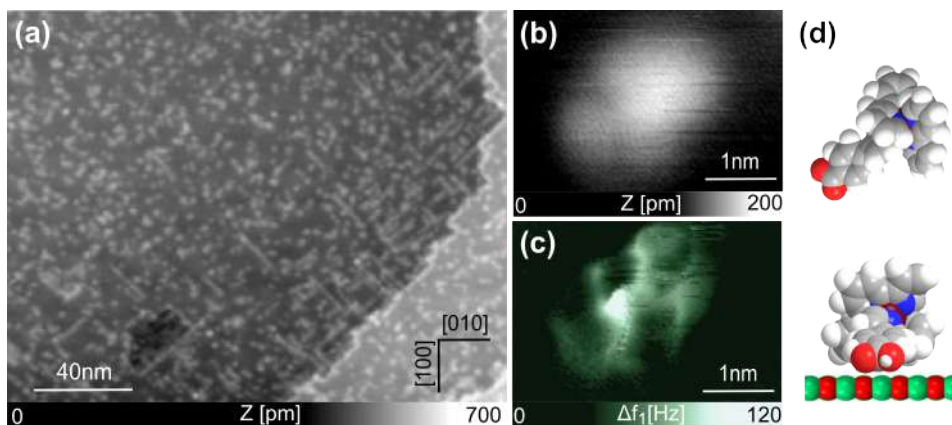


Figure 7.6: $\text{Ru}(\text{bpy})_2(\text{H2})$ adsorbed on NiO. *a*, Large scale topographic image of $\text{Ru}(\text{bpy})_2(\text{H2})$ molecules adsorbed on the surface of NiO(001). *b*, Close up topographic signal acquired in the first scanning pass of the multipass technique showing a single $\text{Ru}(\text{bpy})_2(\text{H2})$. *c*, Frequency shift image recorded in the second scan line on the same molecules while applying an offset of -750 pm, partially resolving the structure of $\text{Ru}(\text{bpy})_2(\text{H2})$. *d*, Model of a single $\text{Ru}(\text{bpy})_2(\text{H2})$ molecule revealing the 3D adsorption geometry of the dye. Scan parameters: *a*: $A_1 = 4$ nm, $\Delta f_1 = -30$ Hz. *b-c*: $A_1 = 4$ nm, $\Delta f_1 = -35$ Hz, $z_{\text{offset}} = -750$ pm.

Obviously, the coverage of figure 7.6a is drastically increased compared to figure 7.5a (~ 0.30 ML against ~ 0.08 ML), even if the concentration of the solution containing $\text{Ru}(\text{bpy})_2(\text{H1})$ was higher than for $[\text{Ru}(\text{bpy})_2(\text{H2})][\text{PF}_6]$ ($\sim 0.5 \cdot 10^{-4}$ M against $\sim 0.3 \cdot 10^{-4}$ M) and also the deposition time was longer for the first dye (30 min against 10 min). Thus, this coverage difference is mainly attributed to the fact that both samples were prepared in different systems where the entry of the spray was positioned 70 cm away from the sample in case of $\text{Ru}(\text{bpy})_2(\text{H1})$ whereas it was placed at 40 cm for $[\text{Ru}(\text{bpy})_2(\text{H2})][\text{PF}_6]$. Also, it has been observed during both deposition processes that the spray stream was interrupted from time to time and needed to be adjusted by tuning the deposition parameters (see section 2.4.3), limiting the reproducibility of this specific deposition technique. However, both surfaces present some similarities. Like $\text{Ru}(\text{bpy})_2(\text{H1})$, $\text{Ru}(\text{bpy})_2(\text{H2})$ exhibits the tendency to preferentially adsorb on defects or step edges. The size of the protrusions are also lying in the same range in both cases, highlighting, here too, the presence of single molecules. One of these single molecules is imaged by the means of the multipass technique and the topographic signal acquired in the first scan line is shown in figure 7.6b whereas the frequency shift image recorded in the second scanning pass as the tip sample distance is reduced by

–750 pm, is displayed in figure 7.6c. As $\text{Ru}(\text{bpy})_2(\text{H1})$, the exact adsorption geometry of the dye is difficult to resolve because of its 3D structure (see tentative model of figure 7.6d).

In conclusion, comparing both large scale images as well as the close up images acquired using the multipass technique after deposition of both dyes, suggests a comparable adsorption behaviour for $\text{Ru}(\text{bpy})_2(\text{H1})$ and $\text{Ru}(\text{bpy})_2(\text{H2})$. In other words, the nature of the anchoring group does not play a crucial role for the bounding of the dye molecule to the substrate, as they are deposited under UHV conditions. However, knowing that ESD is a relatively invasive technique as demonstrated in section 7.2, the latter hypothesis has to be treated carefully. In order to make firm conclusions concerning this point, the experiment should be repeated using a less invasive deposition method, such as sublimation, which is, however, not possible in the case of this kind of complex dye molecules. In addition, the present experiments highlighted another limitation of the ESD method, namely that reproducibility of the process is restricted. Furthermore, it has also been demonstrated that the chosen molecules do not present the ideal morphology to be imaged via SPM techniques with intramolecular resolution. Certainly, selecting molecules with more planar shapes instead of pronounced 3D structure would lead to an enhancement of the resolution when imaged using the multipass method.

7.4 Summary

In this chapter the adsorption of several molecules on the surface of $\text{NiO}(001)$ after sample preparation via ESD was studied by nc-AFM. In a first part, the motivation concerning the choice of these molecules was discussed and their chemical structures were described. The second part of this chapter was dedicated to the testing of the reliability of ESD using the well investigated C_{60} molecules. Comparing two deposition methods, namely sublimation and ESD, it was shown that the latter is a relatively invasive technique in comparison to thermal evaporation. This results in the creation of defects that are acting as anchoring sites for the molecules. To finish, the last part of the chapter was devoted to the imaging of three different dye molecules that can be used for the design of p-type DSSCs, delivering promising efficiency values. First the reference dye P1 was deposited on the surface of $\text{NiO}(001)$ and the symmetric character of its chemical structure was revealed as well by multipass scanning as by multimodal AFM using the torsional mode. Then it was illustrated, using two different ruthenium based dyes that even though their structure could be resolved partially, nc-AFM in general, and the multipass technique in particular, is complicated to apply to molecules presenting a pronounced 3D geometry. Therefore, when the main goal of the study is high resolution imaging, the usage of ESD techniques is recommended for more planar molecules in order to be able to resolve unambiguously their structure and adsorption geometry. However, from the experiments, it could be deduced that the nature of the anchoring group (phosponic- or carboxylic acid) has a negligible influence on the adsorption geometry of the molecules. Yet, considering that ESD is a relatively invasive technique, which can create anchoring sites, this argument has to

be treated carefully.

Conclusion

EVEN if NiO has been demonstrated to be a fascinating material, in particular because it can be used for the design of prototypical p-type DSSCs with the prospect of building efficient tandem solar cells in a near future [8, 9], its interface with other materials has extremely rarely been studied by SPM techniques. Apart from this thesis and its resulting publications [52, 53, 161], only one paper in the literature reports SPM analysis of the functionalization of a NiO(001) surface with molecules [176]. Therefore, this work has been dedicated to the filling of this information gap.

First of all, in chapter 4 the surface of NiO(001) has been investigated by nc-AFM. It has been shown that atomically flat and clean surfaces can be obtained after *in situ* cleavage. However, depending on the crystal batch, two types of surfaces have been reported. While the first was exhibiting curvy steps, the second was showing straight edges that were oriented along the $\langle 110 \rangle$ directions. However, a constant step height of ~ 210 pm has been observed and atomic resolution could be reached using three different scanning modes. The line defects present on the surface of NiO(001) and oriented along the $\langle 110 \rangle$ directions have also been studied in detail. However, even if the defects could be resolved with atomic accuracy, they remain complicated to interpret and their composition is still unclear. In addition, it has been shown that the length but also the number of these defects are temperature dependent.

After the surface of NiO(001) has been characterized, it has been functionalized with several molecules using different sensitization techniques.

In chapter 5, two standard dye molecules, Cu-TCPP and C343, which can be used in n- and p-type DSSCs [7, 21, 218, 219], have both been evaporated on atomically clean NiO(001) surfaces. The adsorption of both dyes have then been compared using nc-AFM. It has been revealed by high resolution imaging that both dyes form molecular islands, where the molecules are lying flat on the surface of the metal oxide. Different types of islands with distinct lattice parameters have been observed. Tentative models reproducing the different mesh motifs have been established with the prospect of relating experimental and model parameters. It has been shown, that because of its smaller

size, C343 appears to form islands with a higher molecular density than Cu-TCPP. Comparing the topographic data to the KPFM images, it has been demonstrated that, the work function is decreased above Cu-TCPP islands compared to the bare surface of NiO(001), whereas it is increased on top of C343 assemblies, implying that the charge transfer occurs in opposite direction. Which is expected when a n-type and a p-type dye are adsorbed on the same metal oxide surface. The values of these charge transfers have also been calculated resulting in the fact that C343 appears to be less efficient than Cu-TCPP in terms of charge injection (0.16 against $0.06\text{ e}^-/\text{nm}^2$). Consequently, it has been stated that for the design of optimized p-type DSSC devices, the development of dyes combining the charge transfer efficiency of Cu-TCPP and p-type character of C343 is required.

In practice, the method termed as SALSAC (surface-as-ligand surface-as-complex) [226] has been introduced in order to design more efficient dye molecules. This technique, where the dyes are assembled directly on the surface of the metal oxide [227–229], is an alternative to evaporation for the functionalization of NiO(001). Therefore, in chapter 6, the first steps of this on-surface reaction has been discussed and studied. The adsorption of the dye precursor DCPDM(bpy) as well as the formation of its corresponding metal complex Fe-DCDM(bpy) have been investigated on the surface of NiO(001) and Au(111) via RT nc-AFM and LT STM/AFM, respectively. Resulting in the fact that the reaction has been proven to be independent from the underlying substrate. Thanks to high resolution imaging, it has also been shown on both surfaces that DCPDM(bpy) exhibits the clear tendency to preferentially adsorb in a flat lying transoid conformation. However, because of increased diffusion on gold, the formation of large assemblies has been proven to be facilitated on this specific surface. Indeed, whereas molecular networks are observed directly after low coverage DCPDM(bpy) deposition at RT on Au(111), the formation of molecular islands on NiO(001) takes place only at higher coverage and after activation by annealing at 420 K. Furthermore, since DCPDM(bpy) becomes prochiral after confinement in 2D, the molecular islands that have been observed on NiO(001) appear to be composed of molecules with alternating chiralities, whereas, the domains formed on Au(111) are enantiopure. However, it has been demonstrated that the emergence of both types of islands is governed by the formation of H-bonding between the carboxylic groups of neighbouring molecules. In the case of NiO, it has also been observed by KPFM that this interactions result in an electrical coupling between the surface and the molecular layer. A partial charge transfer of 0.26 e^- per molecule directed from the surface towards the molecular island has been determined. In consequence, when calculated as a function of active surface, DCPDM(bpy) appears to be almost two times more efficient in terms of charge injection than C343 ($0.11\text{ e}^-/\text{nm}^2$ against $0.06\text{ e}^-/\text{nm}^2$) even if it is not a complete dye but only a precursor. When in contact with Fe atoms, it has been observed on both surfaces that the molecule switches from a transoid to a cisoid conformation. Even if Fe atoms have not been directly observed neither by AFM nor by STM, as well at RT as LT, statistical analysis of high resolution images combined to XPS measurements have demonstrated that this conformation change can unambiguously be attributed to metal coordination, evidencing the formation of the corresponding metal complex.

The last strategy for the sensitization of NiO(001), electrospray deposition, has been

investigated in chapter 7. First of all, the reliability of this method has been tested using the well studied C_{60} molecules [251] as reference molecules. Comparing two preparation techniques, *i.e.* thermal evaporation and ESD, it has been demonstrated that the latter is a relatively invasive technique which gives access to interfaces that cannot be obtained in different conditions. Indeed, when sublimated on the surface of NiO(001), the C_{60} form 2D molecular domains, whereas they adsorb as single molecules when the sample is prepared via the ESD method. This has been attributed to the fact that spray can possibly create small defects on the surface of NiO(001) which act as anchoring sites for molecules. To finish, the adsorption of three different organic dye molecules, that have been previously implemented in the fabrication of efficient p-type DSSCs devices [27, 217, 240–243], have been studied by nc-AFM after sample preparation via ESD. Because of their complex structures and fragility, P1, $Ru(bpy)_2(H1)$ and $Ru(bpy)_2(H2)$ could not be prepared using thermal evaporation. After deposition on NiO(001), it has been observed that all three dyes appear as single molecules, suggesting that the nature of the anchoring group does not play a significant role on the adsorption of the dye when deposited via ESD. In addition, the molecules have been resolved with submolecular resolution applying several scanning modes. However, the non-planar geometries of these dyes makes it difficult to operate nc-AFM. Therefore, in the light of these results, and if the main aim of the experiment is to resolve the structures of the molecules, the use of ESD is recommended for the examination of compound with less pronounced 3D structures.

In conclusion, the adsorption of eight different molecules on the surface of NiO(001) have been explored in this work, giving a solid basis to further studies involving the functionalization of this specific metal oxide. It has been shown that several preparation techniques, including sublimation, on-surface synthesis as well as electro spray deposition, are compatible with the cleanliness requirements of nc-AFM measurements, allowing to resolve the structure of several molecules with submolecular accuracy. However, since the main point of studying sensitized surfaces is to gain information about their working mechanism at the nanoscale, with the prospect of building efficient devices, further comprehensive studies are required. Indeed, only basic investigations concerning the adsorption of molecules have been conducted so far. To get a better overview of the performance of such a system, further investigations should be performed, for example, under illumination. In this way, the optical activities of the different dye molecules as well as their adsorption bandwidth or injection efficiencies could be determined.

Bibliography

- [1] Hagfeldt, A., Boschloo, G., Sun, L., Kloo, L. & Pettersson, H. Dye-sensitized solar cells. *Chem. Rev.* **110**, 6595–6663 (2010). URL <https://doi.org/10.1021/cr900356p>.
- [2] Service, R. F. Is it time to shoot for the sun? *Science* **309**, 548– (2005). URL <http://science.sciencemag.org/content/309/5734/548.abstract>.
- [3] Potočník, J. Renewable energy sources and the realities of setting an energy agenda. *Science* **315**, 810–811 (2007). URL <http://science.sciencemag.org/content/315/5813/810.abstract>.
- [4] Eisenberg, R. & Nocera, D. G. Preface: Overview of the forum on solar and renewable energy. *Inorg. Chem.* **44**, 6799–6801 (2005). URL <https://doi.org/10.1021/ic058006i>.
- [5] Schiermeier, Q., Tollefson, J., Scully, T., Witze, A. & Morton, O. Energy alternatives: Electricity without carbon. *Nature* **454**, 816–823 (2008). URL <https://www.nature.com/news/2008/080813/full/454816a.html>.
- [6] Green, M. A. *et al.* Solar cell efficiency tables (version 51). *Prog Photovolt Res Appl* **26**, 3–12 (2017). URL <https://doi.org/10.1002/pip.2978>.
- [7] Morandeira, A., Boschloo, G., Hagfeldt, A. & Hammarström, L. Photoinduced ultrafast dynamics of coumarin 343 sensitized p-type-nanostructured NiO films. *J. Phys. Chem. B* **109**, 19403–19410 (2005). URL <https://doi.org/10.1021/jp053230e>.
- [8] He, J., Lindström, H., Hagfeldt, A. & Lindquist, S.-E. Dye-sensitized nanostructured p-type nickel oxide film as a photocathode for a solar cell. *J. Phys. Chem. B* **103**, 8940–8943 (1999). URL <http://dx.doi.org/10.1021/jp991681r>.
- [9] He, J., Lindström, H., Hagfeldt, A. & Lindquist, S.-E. Dye-sensitized nanostructured tandem cell-first demonstrated cell with a dye-sensitized photocathode. *Solar Energy Materials and Solar Cells* **62**, 265 – 273 (2000). URL <http://www.sciencedirect.com/science/article/pii/S0927024899001683>.
- [10] Kawazoe, H. *et al.* P-type electrical conduction in transparent thin films of CuAlO₂. *Nature* **389**, 939–942 (1997). URL <http://dx.doi.org/10.1038/40087>.
- [11] Renaud, A. *et al.* CuGaO₂: a promising alternative for NiO in p-type dye solar cells. *J. Mater. Chem.* **22**, 14353–14356 (2012). URL <http://dx.doi.org/10.1039/C2JM31908J>.

Bibliography

- [12] Yu, M., Draskovic, T. I. & Wu, Y. Cu(i)-based delafossite compounds as photocathodes in p-type dye-sensitized solar cells. *Phys. Chem. Chem. Phys.* **16**, 5026–5033 (2014). URL <http://dx.Doi.org/10.1039/C3CP55457K>.
- [13] Sato, H., Minami, T., Takata, S. & Yamada, T. Transparent conducting p-type NiO thin films prepared by magnetron sputtering. *Thin Solid Films* **236**, 27–31 (1993). URL <http://www.sciencedirect.com/science/article/pii/0040609093906364>.
- [14] Odobel, F. *et al.* Recent advances and future directions to optimize the performances of p-type dye-sensitized solar cells. *Coordin. Chem. Rev.* **256**, 2414–2423 (2012). URL <http://dx.Doi.org/10.1016/j.ccr.2012.04.017>.
- [15] D’Amario, L., Boschloo, G., Hagfeldt, A. & Hammarström, L. Tuning of conductivity and density of states of NiO mesoporous films used in p-type DSSCs. *J. Phys. Chem. C* **118**, 19556–19564 (2014). URL <http://dx.Doi.org/10.1021/jp504551v>.
- [16] D’Amario, L., Antila, L. J., Pettersson Rimgard, B., Boschloo, G. & Hammarström, L. Kinetic evidence of two pathways for charge recombination in NiO-based dye-sensitized solar cells. *J. Phys. Chem. Lett.* **6**, 779–783 (2015). URL <http://dx.Doi.org/10.1021/acs.jpcllett.5b00048>.
- [17] De Angelis, F., Fantacci, S., Selloni, A., Grätzel, M. & Nazeeruddin, M. K. Influence of the sensitizer adsorption mode on the open-circuit potential of dye-sensitized solar cells. *Nano Lett.* **7**, 3189–3195 (2007). URL <https://doi.org/10.1021/nl071835b>.
- [18] Yella, A. *et al.* Porphyrin-sensitized solar cells with cobalt (II/III)-based redox electrolyte exceed 12 percent efficiency. *Science* **334**, 629–634 (2011). URL <http://www.sciencemag.org/content/334/6056/629>.
- [19] Ambre, R. *et al.* Effects of porphyrinic meso-substituents on the photovoltaic performance of dye-sensitized solar cells: Number and position of p-carboxyphenyl and thienyl groups on zinc porphyrins. *J. Phys. Chem. C* **116**, 11907–11916 (2012). URL <https://doi.org/10.1021/jp302145x>.
- [20] Ambre, R. B., Chang, G.-F. & Hung, C.-H. Three p-carboxyphenyl groups possessing zinc porphyrins: efficient, stable, and cost-effective sensitizers for dye-sensitized solar cells. *Chem. Commun.* **50**, 725–727 (2014). URL <http://dx.doi.org/10.1039/C3CC47985D>.
- [21] Rochford, J., Chu, D., Hagfeldt, A. & Galoppini, E. Tetrachelate porphyrin chromophores for metal oxide semiconductor sensitization: Effect of the spacer length and anchoring group position. *J. Am. Chem. Soc.* **129**, 4655–4665 (2007). URL <https://doi.org/10.1021/ja068218u>.
- [22] Jöhr, R. *et al.* Characterization of individual molecular adsorption geometries by atomic force microscopy: Cu-TCPP on rutile TiO₂ (110). *The Journal of Chemical Physics* **143**, 094202 (2015). URL <http://dx.Doi.org/10.1063/1.4929608>.
- [23] Zajac, L. *et al.* Self-assembling of Zn porphyrins on a (110) face of rutile TiO₂ the anchoring role of carboxyl groups. *Applied Surface Science* **379**, 277–281 (2016). URL <http://www.sciencedirect.com/science/article/pii/S0169433216308108>.

- [24] Jöhr, R. *et al.* Thermally induced anchoring of a zinc-carboxyphenylporphyrin on rutile TiO₂(110). *The Journal of Chemical Physics* **146**, 184704 (2017). URL <https://aip.scitation.org/doi/abs/10.1063/1.4982936>.
- [25] Jöhr, R. *Interaction of single metallo-porphyrins with titania surfaces - Advance atomic force microscopy studies*. Ph.D. thesis, University of Basel, Faculty of Science (2017). URL http://edoc.unibas.ch/diss/DissB_12122.
- [26] Pellegrin, Y. *et al.* Ruthenium polypyridine complexes as sensitizers in NiO based p-type dye-sensitized solar cells: Effects of the anchoring groups. *J. Photoch. and Photobio. A* **219**, 235–242 (2011). URL <http://www.sciencedirect.com/science/article/pii/S1010603011000876>.
- [27] Marinakis, N., Wobill, C., Constable, E. C. & Housecroft, C. E. Refining the anchor: Optimizing the performance of cyclometallated ruthenium(II) dyes in p-type dye sensitized solar cells. *Polyhedron* **140**, 122 – 128 (2018). URL <http://www.sciencedirect.com/science/article/pii/S0277538717307970>.
- [28] Binnig, G., Rohrer, H., Gerber, C. & Weibel, E. 7×7 reconstruction on Si(111) resolved in real space. *Phys. Rev. Lett.* **50**, 120–123 (1983). URL <https://doi.org/10.1103/PhysRevLett.50.120>.
- [29] Binnig, G. Tunneling through a controllable vacuum gap. *Appl. Phys. Lett.* **40**, 178–180 (1982). URL <http://dx.Doi.org/10.1063/1.92999>.
- [30] Binnig, G., Quate, C. F. & Gerber, C. Atomic force microscope. *Phys. Rev. Lett.* **56**, 930–933 (1986). URL <https://doi.org/10.1103/PhysRevLett.56.930>.
- [31] Albrecht, T. R., Grütter, P., Horne, D. & Rugar, D. Frequency modulation detection using high-Q cantilevers for enhanced force microscope sensitivity. *J. Appl. Phys.* **69**, 668–673 (1991). URL <http://dx.Doi.org/10.1063/1.347347>.
- [32] Giessibl, F. J. Atomic resolution of the silicon (111)-(7×7) surface by atomic force microscopy. *Science* **267**, 68–71 (1995). URL <http://science.sciencemag.org/content/267/5194/68>.
- [33] Ueyama, H., Ohta, M., Sugawara, Y. & Morita, S. Atomically resolved InP(110) surface observed with noncontact ultrahigh vacuum atomic force microscope. *Japanese Journal of Applied Physics* **34**, L1086– (1995). URL <http://stacks.iop.org/1347-4065/34/i=8B/a=L1086>.
- [34] Kitamura, S. & Iwatsuki, M. Observation of silicon surfaces using ultrahigh-vacuum noncontact atomic force microscopy. *Japanese Journal of Applied Physics* **35**, L668– (1996). URL <http://stacks.iop.org/1347-4065/35/i=5B/a=L668>.
- [35] Giessibl, F. J. Forces and frequency shifts in atomic-resolution dynamic-force microscopy. *Phys. Rev. B* **56**, 16010–16015 (1997). URL <https://doi.org/10.1103/PhysRevB.56.16010>.
- [36] Gotsmann, B., Anczykowski, B., Seidel, C. & Fuchs, H. Determination of tip-sample interaction forces from measured dynamic force spectroscopy curves. *Applied Surface Science* **140**, 314–319 (1999). URL <http://www.sciencedirect.com/science/article/pii/S0169433298005479>.

Bibliography

- [37] Dürig, U. Extracting interaction forces and complementary observables in dynamic probe microscopy. *Appl. Phys. Lett.* **76**, 1203–1205 (2000). URL <https://doi.org/10.1063/1.125983>.
- [38] Giessibl, F. J. A direct method to calculate tip–sample forces from frequency shifts in frequency-modulation atomic force microscopy. *Appl. Phys. Lett.* **78**, 123–125 (2001). URL <https://doi.org/10.1063/1.1335546>.
- [39] Sader, J. E. & Jarvis, S. P. Accurate formulas for interaction force and energy in frequency modulation force spectroscopy. *Appl. Phys. Lett.* **84**, 1801–1803 (2004). URL <http://scitation.aip.org/content/aip/journal/apl/84/10/10.1063/1.1667267>.
- [40] Giessibl, F. J. Advances in atomic force microscopy. *Rev. Mod. Phys.* **75**, 949–983 (2003). URL <https://doi.org/10.1103/RevModPhys.75.949>.
- [41] Hamaker, H. The London-Van der Waals attraction between spherical particles. *Physica* **4**, 1058–1072 (1937). URL <https://www.sciencedirect.com/science/article/pii/S0031891437802037>.
- [42] Israelachvili, J. N. 6 - Van der Waals forces. In *Intermolecular and Surface Forces (Third Edition)*, 107–132 (Academic Press, San Diego, 2011). URL <https://www.sciencedirect.com/science/article/pii/B9780123751829100065>.
- [43] Hudlet, S., Saint Jean, M., Guthmann, C. & Berger, J. Evaluation of the capacitive force between an atomic force microscopy tip and a metallic surface. *The European Physical Journal B - Condensed Matter and Complex Systems* **2**, 5–10 (1998). URL <https://doi.org/10.1007/s100510050219>.
- [44] Guggisberg, M. *et al.* Separation of interactions by noncontact force microscopy. *Phys. Rev. B* **61**, 11151–11155 (2000). URL <https://doi.org/10.1103/PhysRevB.61.11151>.
- [45] Israelachvili, J. N. 7 - repulsive steric forces, total intermolecular pair potentials, and liquid structure. In *Intermolecular and Surface Forces (Third Edition)*, 133–149 (Academic Press, San Diego, 2011). URL <https://www.sciencedirect.com/science/article/pii/B9780123751829100077>.
- [46] Kawai, S. *et al.* Systematic achievement of improved atomic-scale contrast via bimodal dynamic force microscopy. *Phys. Rev. Lett.* **103**, 220801 (2009). URL <https://doi.org/10.1103/PhysRevLett.103.220801>.
- [47] Kawai, S. *et al.* Ultrasensitive detection of lateral atomic-scale interactions on graphite (0001) via bimodal dynamic force measurements. *Phys. Rev. B* **81**, 085420 (2010). URL <https://journals.aps.org/prb/abstract/10.1103/PhysRevB.81.085420>.
- [48] Kawai, S., Kitamura, S.-I., Kobayashi, D., Meguro, S. & Kawakatsu, H. An ultrasmall amplitude operation of dynamic force microscopy with second flexural mode. *Appl. Phys. Lett.* **86**, 193107– (2005). URL <https://doi.org/10.1063/1.1923200>.
- [49] Kikukawa, A., Hosaka, S. & Imura, R. Vacuum compatible high-sensitive Kelvin probe force microscopy. *Review of Scientific Instruments* **67**, 1463–1467 (1996). URL <https://doi.org/10.1063/1.1146874>.

- [50] Sommerhalter, C., Matthes, T. W., Glatzel, T., Jäger-Waldau, A. & Lux-Steiner, M. C. High-sensitivity quantitative Kelvin probe microscopy by noncontact ultra-high-vacuum atomic force microscopy. *Appl. Phys. Lett.* **75**, 286–288 (1999). URL <https://doi.org/10.1063/1.124357>.
- [51] Moreno, C., Stetsovych, O., Shimizu, T. K. & Custance, O. Imaging three-dimensional surface objects with submolecular resolution by atomic force microscopy. *Nano Letters* **15**, 2257–2262 (2015). URL <http://dx.doi.org/10.1021/nl504182w>.
- [52] Freund, S. *et al.* Anchoring of a dye precursor on NiO(001) studied by non-contact atomic force microscopy. *Beilstein Journal of Nanotechnology* **9**, 242–249 (2017). URL <http://dx.doi.org/10.3762/bjnano.9.26>.
- [53] Freund, S. *et al.* Transoid-to-cisoid conformation changes of single molecules on surfaces triggered by metal coordination. *ACS Omega* **3**, 12851–12856 (2018). URL <https://doi.org/10.1021/acsomega.8b01792>.
- [54] Gross, L., Mohn, F., Moll, N., Liljeroth, P. & Meyer, G. The chemical structure of a molecule resolved by atomic force microscopy. *Science* **325**, 1110– (2009). URL <http://science.sciencemag.org/content/325/5944/1110.abstract>.
- [55] Kelvin, L. V. contact electricity of metals. *The London, Edinburgh, and Dublin Philosophical Magazine and Journal of Science* **46**, 82–120 (1898). URL <https://doi.org/10.1080/14786449808621172>.
- [56] Weaver, J. M. R. & Abraham, D. W. High resolution atomic force microscopy potentiometry. *Journal of Vacuum Science & Technology B: Microelectronics and Nanometer Structures Processing, Measurement, and Phenomena* **9**, 1559–1561 (1991). URL <https://doi.org/10.1116/1.585423>.
- [57] Nonnenmacher, M., O’Boyle, M. P. & Wickramasinghe, H. K. Kelvin probe force microscopy. *Appl. Phys. Lett.* **58**, 2921 (1991). URL <http://dx.doi.org/10.1063/1.105227>.
- [58] Loppacher, C. *et al.* FM demodulated Kelvin probe force microscopy for surface photovoltage tracking. *Nanotechnology* **16**, S1– (2005). URL <http://stacks.iop.org/0957-4484/16/i=3/a=001>.
- [59] Kitamura, S. & Iwatsuki, M. High-resolution imaging of contact potential difference with ultrahigh vacuum noncontact atomic force microscope. *Appl. Phys. Lett.* **72**, 3154–3156 (1998). URL <https://doi.org/10.1063/1.121577>.
- [60] Glatzel, T., Sadewasser, S. & Lux-Steiner, M. C. Amplitude or frequency modulation-detection in Kelvin probe force microscopy. *Appl. Surf. Sci.* **210**, 84–89 (2003). URL [http://dx.doi.org/10.1016/S0169-4332\(02\)01484-8](http://dx.doi.org/10.1016/S0169-4332(02)01484-8).
- [61] Zerweck, U., Loppacher, C., Otto, T., Grafström, S. & Eng, L. M. Accuracy and resolution limits of Kelvin probe force microscopy. *Phys. Rev. B* **71**, 125424 (2005). URL <https://doi.org/10.1103/PhysRevB.71.125424>.
- [62] Milde, P. *et al.* Interface dipole formation of different ZnPcCl 8 phases on Ag(111) observed by Kelvin probe force microscopy. *Nanotechnology* **19**, 305501 (2008). URL <http://stacks.iop.org/0957-4484/19/i=30/a=305501>.

Bibliography

- [63] Glatzel, T., Zimmerli, L., Koch, S., Kawai, S. & Meyer, E. Molecular assemblies grown between metallic contacts on insulating surfaces. *Appl. Phys. Lett.* **94**, 063303 (2009). URL <http://dx.Doi.org/10.1063/1.3080614>.
- [64] Fessler, G. *Structural Friction Anisotropy on the Nanometer Scale*. Ph.D. thesis, University of Basel, Faculty of Science (2013). URL http://edoc.unibas.ch/diss/DissB_10652.
- [65] Frey, S. D. *The nature of condensed single molecules : local electronic and mechanical characteristics*. Ph.D. thesis, University of Basel, Faculty of Science. (2014). URL http://edoc.unibas.ch/diss/DissB_10690.
- [66] Meier, T. *Controlling structural, chemical and electronic properties of single molecules on surfaces*. Ph.D. thesis, University of Basel, Faculty of Science (2018). URL http://edoc.unibas.ch/diss/DissB_12648.
- [67] Automated amplitude calibration in non-contact afm mode. URL <http://www.specs-zurich.com/upload/cms/user/AN-AmplitudecalibrationncAFM.pdf>.
- [68] Koch, S. *Investigation of hexagonal 2D super structures by dynamic force spectroscopy*. Ph.D. thesis, University of Basel, Faculty of Science (2012). URL http://edoc.unibas.ch/diss/DissB_9932.
- [69] Eberhart, M. E. *Why Things Break* (Harmony Books, 2003).
- [70] Schmid, M., Renner, A. & Giessibl, F. J. Device for in situ cleaving of hard crystals. *Review of Scientific Instruments* **77**, 036101– (2006). URL <https://Doi.org/10.1063/1.2166670>.
- [71] Hernández Redondo, A. *Copper(I) polypyridine complexes: the sensitizers of the future for dye-sensitized sola cells*. Ph.D. thesis, University of Basel, Faculty of Science (2009). URL http://edoc.unibas.ch/diss/DissB_8757.
- [72] Fenn, J. B., Mann, M., Meng, C. K., Wong, S. F. & Whitehouse, C. M. Electrospray ionization for mass spectrometry of large biomolecules. *Science* **246**, 64–71 (1989). URL <http://science.sciencemag.org/content/246/4926/64>. <http://science.sciencemag.org/content/246/4926/64.full.pdf>.
- [73] Fenn, J. B. Ion formation from charged droplets: roles of geometry, energy, and time. *Journal of the American Society for Mass Spectrometry* **4**, 524 – 535 (1993). URL <http://www.sciencedirect.com/science/article/pii/1044030593850140>.
- [74] Hinaut, A., Pawlak., R., Meyer, E. & Glatzel, T. Electrospray deposition of organic molecules on bulk insulator surfaces. *Beilstein Journal of Nanotechnology* **6**, 1927–1934 (2015). URL <https://www.beilstein-journals.org/bjnano/articles/6/195>.
- [75] Hinaut, A. *et al.* Electrospray deposition of structurally complex molecules revealed by atomic force microscopy. *Nanoscale* **10**, 1337–1344 (2018). URL <http://dx.Doi.org/10.1039/C7NR06261C>.
- [76] Brunner, F. *et al.* Modular synthesis of simple cycloruthenated complexes with state-of-the-art performance in p-type DSCs. *J. Mater. Chem. C* **4**, 9823–9833 (2016). URL <http://dx.doi.org/10.1039/C6TC03874C>.

- [77] Wager, J. F. Transparent electronics. *Science* **300**, 1245–1246 (2003). URL <http://science.sciencemag.org/content/300/5623/1245.abstract>.
- [78] Facchetti, A. & Marks, T. J. *Transparent electronics: from synthesis to applications* (John Wiley and Sons Ltd, 2010).
- [79] Hartnagel, H. L., Dawar, A. L., Jain, A. & Jagadish, C. *Semiconducting Transparent Thin Films* (Institute of Physics, Bristol, 1995).
- [80] Kim, H. *et al.* Indium tin oxide thin films for organic light-emitting devices. *Appl. Phys. Lett.* **74**, 3444–3446 (1999). URL <https://doi.org/10.1063/1.124122>.
- [81] Tang, C. W. & VanSlyke, S. A. Organic electroluminescent diodes. *Appl. Phys. Lett.* **51**, 913–915 (1987). URL <http://scitation.aip.org/content/aip/journal/apl/51/12/10.1063/1.98799>.
- [82] Kim, H. *et al.* Electrical, optical, and structural properties of indium tin oxide thin films for organic light-emitting devices. *Journal of Applied Physics* **86**, 6451–6461 (1999). URL <https://doi.org/10.1063/1.371708>.
- [83] Andersson, A. *et al.* Fluorine tin oxide as an alternative to indium tin oxide in polymer LEDs. *Adv. Mater.* **10**, 859–863 (1999). URL [https://doi.org/10.1002/\(SICI\)1521-4095\(199808\)10:11<859::AID-ADMA859>3.0.CO;2-1](https://doi.org/10.1002/(SICI)1521-4095(199808)10:11<859::AID-ADMA859>3.0.CO;2-1).
- [84] Banyamin, Y. Z., Kelly, J. P., West, G. & Boardman, J. Electrical and optical properties of fluorine doped tin oxide thin films prepared by magnetron sputtering. *Coatings* **4**, 732–746 (2014). URL <http://www.mdpi.com/2079-6412/4/4/732>.
- [85] Ramelan, A. H., Wahyuningsih, S., Munawaroh, H. & Narayan, R. ZnO wide bandgap semiconductors preparation for optoelectronic devices. *IOP Conference Series: Materials Science and Engineering* **176**, 012008 (2017). URL <http://stacks.iop.org/1757-899X/176/i=1/a=012008>.
- [86] Lee, D. W. & Yoo, B. R. Advanced metal oxide (supported) catalysts: Synthesis and applications. *Journal of Industrial and Engineering Chemistry* **20**, 3947–3959 (2014). URL <http://www.sciencedirect.com/science/article/pii/S1226086X14003955>.
- [87] Clark, A. Oxides of the transition metals as catalysts. *Ind. Eng. Chem.* **45**, 1476–1480 (1953). URL <https://doi.org/10.1021/ie50523a034>.
- [88] Haruta, M. Size- and support-dependency in the catalysis of gold. *Catalysis Today* **36**, 153–166 (1997). URL <http://www.sciencedirect.com/science/article/pii/S0920586196002088>.
- [89] Jager, B. & Espinoza, R. Advances in low temperature Fischer–Tropsch synthesis. *Catalysis Today* **23**, 17–28 (1995). URL <http://www.sciencedirect.com/science/article/pii/S092058619400136P>.
- [90] Sie, S. T. Process development and scale up: Iv. case history of the development of a fischer-tropsch synthesis process. *Reviews in Chemical Engineering* **14**, 109–157 (1998). URL <https://www.scopus.com/record/display.uri?eid=2-s2.0-0032317328&origin=inward>.

Bibliography

- [91] Khodakov, A. Y., Chu, W. & Fongarland, P. Advances in the development of novel cobalt Fischer–Tropsch catalysts for synthesis of long-chain hydrocarbons and clean fuels. *Chem. Rev.* **107**, 1692–1744 (2007). URL <https://doi.org/10.1021/cr050972v>.
- [92] Iwamoto, M. & Hamada, H. Removal of nitrogen monoxide from exhaust gases through novel catalytic processes. *Catalysis Today* **10**, 57–71 (1991). URL <http://www.sciencedirect.com/science/article/pii/092058619180074J>.
- [93] Spivey, J. J. Complete catalytic oxidation of volatile organics. *Ind. Eng. Chem. Res.* **26**, 2165–2180 (1987). URL <https://doi.org/10.1021/ie00071a001>.
- [94] Goldstein, A. H. & Galbally, I. E. Known and unexplored organic constituents in the earth’s atmosphere. *Environ. Sci. Technol.* **41**, 1514–1521 (2007). URL <https://doi.org/10.1021/es072476p>.
- [95] Brunekreef, B. & Holgate, S. T. Air pollution and health. *The Lancet* **360**, 1233–1242 (2002). URL <http://www.sciencedirect.com/science/article/pii/S0140673602112748>.
- [96] Bamwenda, G., Tsubota, S., Nakamura, T. & Haruta, M. The influence of the preparation methods on the catalytic activity of platinum and gold supported on TiO₂ for CO oxidation. *Catalysis Letters* **44**, 83–87 (1997). URL <https://doi.org/10.1023/A:1018925008633>.
- [97] Bowker, M. & Fourré, E. Direct interactions between metal nanoparticles and support: Stm studies of pd on TiO₂(110). *Applied Surface Science* **254**, 4225–4229 (2008). URL <http://www.sciencedirect.com/science/article/pii/S0169433208000445>.
- [98] Wang, D. & Bierwagen, G. P. Sol–gel coatings on metals for corrosion protection. *Progress in Organic Coatings* **64**, 327–338 (2009). URL <http://www.sciencedirect.com/science/article/pii/S0300944008002038>.
- [99] Henrich, V. E. & Cox, P. A. *The Surface Science of Metal Oxides* (Cambridge University Press, 1994).
- [100] Vurens, G., Salmeron, M. & Somorjai, G. The preparation of thin ordered transition metal oxide films on metal single crystals for surface science studies. *Progress in Surface Science* **32**, 333–360 (1989). URL <http://www.sciencedirect.com/science/article/pii/0079681689900063>.
- [101] Freund, H.-J., Kühlenbeck, H. & Staemmler, V. Oxide surfaces. *Rep. on Prog. in Phys.* **59**, 283–347 (1996). URL <http://stacks.iop.org/0034-4885/59/i=3/a=001>.
- [102] Freund, H.-J. Introductory lecture: Oxide surfaces. *Faraday Discuss.* **114**, 1–31 (1999). URL <http://dx.doi.org/10.1039/A907182B>.
- [103] Cappus, D. *et al.* Polar surfaces of oxides: reactivity and reconstruction. *Surf. Sci.* **337**, 268–277 (1995). URL <http://www.sciencedirect.com/science/article/pii/0039602895006249>.
- [104] Espinós, J. P. *et al.* Interface effects for Cu, CuO, and Cu₂O deposited on SiO₂ and ZrO₂. XPS determination of the valence state of copper in Cu/SiO₂ and Cu/ZrO₂.

- catalysts. *J. of Phys. Chem. B* **106**, 6921–6929 (2002). URL <http://dx.Doi.org/10.1021/jp014618m>.
- [105] Uehara, Y., Matsumoto, T. & Ushioda, S. Identification of O atoms on a Cu(110) surface by scanning tunneling microscope light emission spectra. *Phys. Rev. B* **66**, 075413 (2002). URL <https://doi.org/10.1103/PhysRevB.66.075413>.
- [106] Hu, Y., Maschek, K., Sun, L., Hohage, M. & Zeppenfeld, P. para-sexiphenyl thin film growth on Cu(110) and Cu(110)-(2×1)O surfaces. *Surf. Sci.* **600**, 762–769 (2006). URL <http://dx.Doi.org/10.1016/j.susc.2005.11.027>.
- [107] Oehzelt, M. *et al.* α -sexithiophene on Cu(110) and Cu(110)-(2×1)O: An STM and NEXAFS study. *Surf. Sci.* **603**, 412–418 (2009). URL <http://dx.Doi.org/10.1016/j.susc.2008.12.005>.
- [108] Bamidele, J. *et al.* Chemical tip fingerprinting in scanning probe microscopy of an oxidized Cu(110) surface. *Phys. Rev. B* **86**, 155422 (2012). URL <http://dx.Doi.org/10.1103/PhysRevB.86.155422>.
- [109] Bamidele, J. *et al.* Image formation and contrast inversion in noncontact atomic force microscopy imaging of oxidized Cu(110) surfaces. *Phys. Rev. B* **90**, 035410 (2014). URL <https://doi.org/10.1103/PhysRevB.90.035410>.
- [110] Schintke, S. *et al.* Insulator at the ultrathin limit: MgO on Ag(001). *Phys. Rev. Lett.* **87**, 276801 (2001). URL <https://link.aps.org/doi/10.1103/PhysRevLett.87.276801>.
- [111] Lu, J.-L., Gao, H.-J., Shaikhutdinov, S. & Freund, H.-J. Morphology and defect structure of the CeO₂(111) films grown on Ru(0001) as studied by scanning tunneling microscopy. *Surface Science* **600**, 5004–5010 (2006). URL <http://www.sciencedirect.com/science/article/pii/S0039602806008958>.
- [112] Jaeger, R. *et al.* Formation of a well-ordered aluminium oxide overlayer by oxidation of NiAl(110). *Surface Science* **259**, 235–252 (1991). URL <http://www.sciencedirect.com/science/article/pii/0039602891905557>.
- [113] Stierle, A., Renner, F., Streitl, R. & Dosch, H. Observation of bulk forbidden defects during the oxidation of NiAl(110). *Phys. Rev. B* **64**, 165413 (2001). URL <https://link.aps.org/doi/10.1103/PhysRevB.64.165413>.
- [114] Pang, C. L., Raza, H., Haycock, S. A. & Thornton, G. Noncontact atomic force microscopy imaging of ultrathin Al₂O₃ on NiAl(110). *Phys. Rev. B* **65**, 201401 (2002). URL <https://link.aps.org/doi/10.1103/PhysRevB.65.201401>.
- [115] Wolf, D. Reconstruction of NaCl surfaces from a dipolar solution to the Madelung problem. *Phys. Rev. Lett.* **68**, 3315–3318 (1992). URL <https://doi.org/10.1103/PhysRevLett.68.3315>.
- [116] Castell, M. R. *et al.* Atomic-resolution STM of a system with strongly correlated electrons : NiO(001) surface structure and defect sites. *Phys. Rev. B* **55**, 7859–7863 (1997). URL <https://doi.org/10.1103/PhysRevB.55.7859>.

Bibliography

- [117] Hosoi, H., Sueoka, K., Hayakawa, K. & Mukasa, K. Atomic resolved imaging of cleaved NiO(100) surfaces by nc-AFM. *Appl. Surf. Sci.* **157**, 218–221 (2000). URL <http://www.sciencedirect.com/science/article/pii/S0169433299005292>.
- [118] Hosoi, H., Kimura, M., Hayakawa, K., Sueoka, K. & Mukasa, K. Non-contact atomic force microscopy of an antiferromagnetic NiO(100) surface using a ferromagnetic tip. *Appl. Phys. A* **72**, S23–S26 (2001). URL <http://dx.Doi.org/10.1007/s003390100722>.
- [119] Allers, W., Langkat, S. & Wiesendanger, R. Dynamic low-temperature scanning force microscopy on nickel oxide (001). *Appl. Phys. A* **72**, S27–S30 (2001). URL <http://dx.Doi.org/10.1007/s003390100731>.
- [120] Langkat, S., Hölscher, H., Schwarz, A. & Wiesendanger, R. Determination of site specific interatomic forces between an iron coated tip and the NiO(001) surface by force field spectroscopy. *Surf. Sci.* **527**, 12–20 (2003). URL [http://dx.Doi.org/10.1016/S0039-6028\(03\)00076-1](http://dx.Doi.org/10.1016/S0039-6028(03)00076-1).
- [121] Hosoi, H., Sueoka, K. & Mukasa, K. Investigations on the topographical asymmetry of non-contact atomic force microscopy images of NiO(001) surface observed with a ferromagnetic tip. *Nanotechnology* **15**, 505–509 (2004). URL <http://stacks.iop.org/0957-4484/15/i=5/a=018>.
- [122] Kaiser, U., Schwarz, A. & Wiesendanger, R. Magnetic exchange force microscopy with atomic resolution. *Nature* **446**, 522–525 (2007). URL <http://dx.Doi.org/10.1038/nature05617>.
- [123] Schmid, M., Mannhart, J. & Giessibl, F. J. Searching atomic spin contrast on nickel oxide (001) by force microscopy. *Phys. Rev. B* **77**, 045402 (2008). URL <https://doi.org/10.1103/PhysRevB.77.045402>.
- [124] Pielmeier, F. & Giessibl, F. J. Spin resolution and evidence for superexchange on NiO(001) observed by force microscopy. *Phys. Rev. Lett.* **110**, 266101 (2013). URL <https://doi.org/10.1103/PhysRevLett.110.266101>.
- [125] Wyckoff, R. W. G. *Crystal Structures* (Wiley Interscience, 1965), 2nd edn.
- [126] Bäumer, M. *et al.* The structure of thin NiO(100) films grown on Ni(100) as determined by low-energy-electron diffraction and scanning tunneling microscopy. *Surface Science* **253**, 116–128 (1991). URL <http://www.sciencedirect.com/science/article/pii/003960289190585G>.
- [127] Bertrams, T. & Neddermeyer, H. Growth of NiO(100) layers on Ag(100): Characterization by scanning tunneling microscopy. *Journal of Vacuum Science & Technology B: Microelectronics and Nanometer Structures Processing, Measurement, and Phenomena* **14**, 1141–1144 (1996). URL <https://doi.org/10.1116/1.588416>.
- [128] Tasker, P. W. The stability of ionic crystal surfaces. *Journal of Physics C: Solid State Physics* **12**, 4977– (1979). URL <http://stacks.iop.org/0022-3719/12/i=22/a=036>.

- [129] Ventrice, C. A., Bertrams, T., Hannemann, H., Brodde, A. & Neddermeyer, H. Stable reconstruction of the polar (111) surface of NiO on Au(111). *Phys. Rev. B* **49**, 5773–5776 (1994). URL <https://doi.org/10.1103/PhysRevB.49.5773>.
- [130] Hannemann, H., Jr., C. A. V., Bertrams, T., Brodde, A. & Neddermeyer, H. Scanning tunneling microscopy on the growth of ordered NiO layers on Au(111). *Phys. Stat. Sol. (a)* **146**, 289–297 (1994). URL <https://doi.org/10.1002/pssa.2211460125>.
- [131] Rohr, F. *et al.* Hydroxyl driven reconstruction of the polar NiO(111) surface. *Surface Science* **315**, L977–L982 (1994). URL <http://www.sciencedirect.com/science/article/pii/0039602894905290>.
- [132] Kitakatsu, N., Maurice, V., Hinnen, C. & Marcus, P. Surface hydroxylation and local structure of NiO thin films formed on Ni(111). *Surf. Sci.* **407**, 36–58 (1998). URL <http://www.sciencedirect.com/science/article/pii/S0039602898000892>.
- [133] Kitakatsu, N., Maurice, V. & Marcus, P. Local decomposition of NiO ultra-thin films formed on Ni(111). *Surface Science* **411**, 215–230 (1998). URL <http://www.sciencedirect.com/science/article/pii/S0039602898003720>.
- [134] Wöll, C. The chemistry and physics of zinc oxide surfaces. *Progress in Surface Science* **82**, 55–120 (2007). URL <http://www.sciencedirect.com/science/article/pii/S0079681606000955>.
- [135] Batzill, M. & Diebold, U. The surface and materials science of tin oxide. *Progress in Surface Science* **79**, 47–154 (2005). URL <http://www.sciencedirect.com/science/article/pii/S007968160500050X>.
- [136] Diebold, U. The surface science of titanium dioxide. *Surface Science Reports* **48**, 53–229 (2003). URL <http://www.sciencedirect.com/science/article/pii/S0167572902001000>.
- [137] O'Regan, M., B.; Grätzel. A low-cost, high-efficiency solar cell based on dye-sensitized colloidal TiO₂ films. *Nature* **353**, 737–739 (1991). URL <https://www.nature.com/articles/353737a0>.
- [138] Murray, P. *et al.* Extended defects on TiO₂(100) 1×3. *Surface Science* **321**, 217–228 (1994). URL <http://www.sciencedirect.com/science/article/pii/0039602894901872>.
- [139] Murray, P. W., Condon, N. G. & Thornton, G. Effect of stoichiometry on the structure of TiO₂(110). *Phys. Rev. B* **51**, 10989–10997 (1995). URL <https://doi.org/10.1103/PhysRevB.51.10989>.
- [140] Fukui, K.-i., Onishi, H. & Iwasawa, Y. Imaging of individual formate ions adsorbed on TiO₂(110) surface by non-contact atomic force microscopy. *Chem. Phys. Lett.* **280**, 296–301 (1997). URL <http://www.sciencedirect.com/science/article/pii/S0009261497011433>.
- [141] Lauritsen, J. V. *et al.* Chemical identification of point defects and adsorbates on a metal oxide surface by atomic force microscopy. *Nanotechnology* **17**, 3436–3441 (2006). URL <http://stacks.iop.org/0957-4484/17/i=14/a=015>.

Bibliography

- [142] Bechstein, R. *et al.* 'all-inclusive' imaging of the rutile TiO₂(110) surface using nc-AFM. *Nanotechnology* **20**, 505703 (2009). URL <http://stacks.iop.org/0957-4484/20/i=50/a=505703>.
- [143] Onishi, H. & Iwasawa, Y. Reconstruction of TiO₂(110) surface: STM study with atomic-scale resolution. *Surface Science* **313**, L783–L789 (1994). URL <http://www.sciencedirect.com/science/article/pii/0039602894911460>.
- [144] Zhang, L., Li, M. & Diebold, U. Characterization of Ca impurity segregation on the TiO₂(110) surface. *Surface Science* **412–413**, 242–251 (1998). URL <http://www.sciencedirect.com/science/article/pii/S0039602898004324>.
- [145] Bennett, R. A., Stone, P., Price, N. J. & Bowker, M. Two (1×2) reconstructions of TiO₂(110): Surface rearrangement and reactivity studied using elevated temperature scanning tunneling microscopy. *Phys. Rev. Lett.* **82**, 3831–3834 (1999). URL <https://doi.org/10.1103/PhysRevLett.82.3831>.
- [146] Li, M. *et al.* The influence of the bulk reduction state on the surface structure and morphology of rutile TiO₂(110) single crystals. *J. Phys. Chem. B* **104**, 4944–4950 (2000). URL <https://doi.org/10.1021/jp9943272>.
- [147] Campbell, C. T. Ultrathin metal films and particles on oxide surfaces: structural, electronic and chemisorptive properties. *Surf. Sci. Rep.* **27**, 1–111 (1997). URL <http://www.sciencedirect.com/science/article/pii/S0167572996000118>.
- [148] Abriou, D., Creuzet, F. & Jupille, J. Characterization of cleaved MgO(100) surfaces. *Surface Science* **352–354**, 499–503 (1996). URL <http://www.sciencedirect.com/science/article/pii/0039602895011870>.
- [149] Henry, C. R. Surface studies of supported model catalysts. *Surface Science Reports* **31**, 231–325 (1998). URL <http://www.sciencedirect.com/science/article/pii/S0167572998000028>.
- [150] Ashworth, T., Pang, C., Wincott, P., Vaughan, D. & Thornton, G. Imaging in situ cleaved MgO(100) with non-contact atomic force microscopy. *Applied Surface Science* **210**, 2–5 (2003). URL <http://www.sciencedirect.com/science/article/pii/S0169433202014691>.
- [151] Barth, C., Claes, C. & Henry, C. R. Surface preparation of hard ionic crystals by ultrahigh vacuum cleavage. *Rev. Sci. Instrum.* **76**, 083907 (2005). URL <http://dx.doi.org/10.1063/1.2001669>.
- [152] Kubo, T. & Nozoye, H. Morphology and structure of Mg–Ti–O spinel(100) epitaxially grown on MgO(100): effect of solid state reactions. *Thin Solid Films* **394**, 150–157 (2001). URL <http://www.sciencedirect.com/science/article/pii/S0040609001010112>.
- [153] Barth, C. & Henry, C. R. Atomic resolution imaging of the (001) surface of UHV cleaved MgO by dynamic scanning force microscopy. *Phys. Rev. Lett.* **91**, 196102– (2003). URL <https://link.aps.org/doi/10.1103/PhysRevLett.91.196102>.

- [154] Barth, C. & Henry, C. R. Kelvin probe force microscopy on MgO(001) surfaces and supported pd nanoclusters. *J. Phys. Chem. C* **113**, 247–253 (2009). URL <https://doi.org/10.1021/jp807340k>.
- [155] Barth, C., Foster, A. S., Henry, C. R. & Shluger, A. L. Recent trends in surface characterization and chemistry with high-resolution scanning force methods. *Adv. Mater.* **23**, 477–501 (2010). URL <https://doi.org/10.1002/adma.201002270>.
- [156] Newman, R. & Chrenko, R. M. Optical properties of nickel oxide. *Phys. Rev.* **114**, 1507–1513 (1959). URL <https://doi.org/10.1103/PhysRev.114.1507>.
- [157] Adler, D. & Feinleib, J. Electrical and optical properties of narrow-band materials. *Phys. Rev. B* **2**, 3112–3134 (1970). URL <https://doi.org/10.1103/PhysRevB.2.3112>.
- [158] Sawatzky, G. A. & Allen, J. W. Magnitude and origin of the band gap in NiO. *Phys. Rev. Lett.* **53**, 2339–2342 (1984). URL <https://doi.org/10.1103/PhysRevLett.53.2339>.
- [159] Hüfner, S. Electronic structure of NiO and related 3d-transition-metal compounds. *Advances in Physics* **43**, 183–356 (1994). URL <https://doi.org/10.1080/00018739400101495>.
- [160] Boschloo, G. & Hagfeldt, A. Spectroelectrochemistry of nanostructured NiO. *J. Phys. Chem. B* **105**, 3039–3044 (2001). URL <http://dx.doi.org/10.1021/jp003499s>.
- [161] Freund, S. *et al.* Comparing a porphyrin- and a coumarin-based dye adsorbed on NiO(001). *Beilstein Journal of Nanotechnology* **10**, 874–881 (2019). URL <http://dx.doi.org/10.3762/bjnano.10.88>.
- [162] Prauzner-Bechcicki, J. S. *et al.* High-resolution STM studies of terephthalic acid molecules on rutile TiO₂(110)-(1×1) surfaces. *J. Phys. Chem. C* **113**, 9309–9315 (2009). URL <https://doi.org/10.1021/jp901184t>.
- [163] Zasada, F. *et al.* Chemical functionalization of the TiO₂(110)-(1×1) surface by deposition of terephthalic acid molecules. a density functional theory and scanning tunneling microscopy study. *J. Phys. Chem. C* **115**, 4134–4144 (2011). URL <https://doi.org/10.1021/jp111014r>.
- [164] Schütte, J. *et al.* Imaging perylene derivatives on rutile TiO₂(110) by noncontact atomic force microscopy. *Phys. Rev. B* **79**, 045428 (2009). URL <https://doi.org/10.1103/PhysRevB.79.045428>.
- [165] Loske, F. *et al.* Growth of ordered C₆₀ islands on TiO₂(110). *Nanotechnology* **20**, 065606 (2009). URL <http://stacks.iop.org/0957-4484/20/i=6/a=065606>.
- [166] Loske, F. & Kühnle, A. Manipulation of C₆₀ islands on the rutile TiO₂ (110) surface using noncontact atomic force microscopy. *Appl. Phys. Lett.* **95**, 043110 (2009). URL <http://dx.doi.org/10.1063/1.3184784>.
- [167] Pawlak, R. *et al.* Hydroxyl-induced partial charge states of single porphyrins on titania rutile. *J. Phys. Chem. C* **121**, 3607–3614 (2017). URL <http://dx.doi.org/10.1021/acs.jpcc.6b11873>.

Bibliography

- [168] Valden, M., Lai, X. & Goodman, D. W. Onset of catalytic activity of gold clusters on titania with the appearance of nonmetallic properties. *Science* **281**, 1647–1650 (1998). URL <http://science.sciencemag.org/content/281/5383/1647.abstract>.
- [169] Wahlström, E. *et al.* Bonding of gold nanoclusters to oxygen vacancies on rutile TiO₂(110). *Phys. Rev. Lett.* **90**, 026101 (2003). URL <https://link.aps.org/doi/10.1103/PhysRevLett.90.026101>.
- [170] Matthey, D. *et al.* Enhanced bonding of gold nanoparticles on oxidized TiO₂(110). *Science* **315**, 1692–1696 (2007). URL <http://science.sciencemag.org/content/315/5819/1692.abstract>.
- [171] Bonanni, S., Ait-Mansour, K., Harbich, W. & Brune, H. Effect of the TiO₂ reduction state on the catalytic CO oxidation on deposited size-selected Pt cluster. *J. Am. Chem. Soc.* **134**, 3445–3450 (2012). URL <https://doi.org/10.1021/ja2098854>.
- [172] Bonanni, S., Ait-Mansour, K., Harbich, W. & Brune, H. Reaction-induced cluster ripening and initial size-dependent reaction rates for CO oxidation on Pt_n/TiO₂(110)–(1×1). *J. Am. Chem. Soc.* **136**, 8702–8707 (2014). URL <https://doi.org/10.1021/ja502867r>.
- [173] Haas, G. *et al.* Nucleation and growth of supported clusters at defect sites: Pd/MgO(001). *Phys. Rev. B* **61**, 11105–11108 (2000). URL <https://link.aps.org/doi/10.1103/PhysRevB.61.11105>.
- [174] Pakarinen, O. H., Barth, C., Foster, A. S. & Henry, C. R. Imaging the real shape of nanoclusters in scanning force microscopy. *Journal of Applied Physics* **103**, 054313– (2008). URL <https://doi.org/10.1063/1.2841700>.
- [175] Custance, O., Perez, R. & Morita, S. Atomic force microscopy as a tool for atom manipulation. *Nat. Nanotechnol.* **4**, 803–810 (2009). URL <http://dx.Doi.org/10.1038/nnano.2009.347>.
- [176] Schwarz, A. *et al.* Determining adsorption geometry, bonding, and translational pathways of a metal-organic complex on an oxide surface: Co-salen on NiO(001). *J. Phys. Chem. C* **117**, 1105–1112 (2013). URL <http://dx.Doi.org/10.1021/jp311702j>.
- [177] Farnsworth, H. E. & Madden, H. H. Mechanism of chemisorption, place exchange, and oxidation on a (100) nickel surface. *J. Appl. Phys.* **32**, 1933–1937 (1961). URL <http://dx.Doi.org/10.1063/1.1728265>.
- [178] Germer, L. H. & MacRae, A. U. Oxygen-nickel structures on the (110) face of clean nickel. *J. Appl. Phys.* **33**, 2923–2932 (1962). URL <http://dx.Doi.org/10.1063/1.1728537>.
- [179] Netzer, F. P. & Prutton, M. LEED and electron spectroscopic observations on NiO (100). *J. Phys. C: Solid State* **8**, 2401–2412 (1975). URL <http://stacks.iop.org/0022-3719/8/i=15/a=014>.
- [180] Narusawa, T., Gibson, W. M. & Törnqvist, E. Relaxation of Ni(111) surface by oxygen adsorption. *Phys. Rev. Lett.* **47**, 417–420 (1981). URL <https://doi.org/10.1103/PhysRevLett.47.417>.

- [181] Bäumer, M. Influence of the defects of a thin NiO(100) film on the adsorption of NO. *J. Vac. Sci. Technol. A* **10**, 2407–2411 (1992). URL <http://dx.Doi.org/10.1116/1.577975>.
- [182] Cappus, D. *et al.* Hydroxyl groups on oxide surfaces: NiO(100), NiO(111) and Cr₂O₃(111). *Chem. Phys.* **177**, 533–546 (1993). URL <http://www.sciencedirect.com/science/article/pii/0301010493800314>.
- [183] Öfner, H. & Zaera, F. Surface defect characterization in oxygen-dosed nickel surfaces and in NiO thin films by CO adsorption-desorption experiments. *J. Phys. Chem. B* **101**, 9069–9076 (1997). URL <http://dx.Doi.org/10.1021/jp971854h>.
- [184] Carson, G. A., Nassir, M. H., Wulser, K. W. & Langell, M. A. Fuchs-kliewer hreel phonon spectrum of single crystal NiO(100) and of ni(100)/NiO(111) and Ni(100)/NiO(100) thin films. *Surf. Sci. Spectra* **5**, 229–234 (1998). URL <http://dx.Doi.org/10.1116/1.1247842>.
- [185] Schulze, M., Reissner, R., Lorenz, M., Radke, U. & Schnurnberger, W. Photoelectron study of electrochemically oxidized nickel and water adsorption on defined NiO surface layers. *Electrochim. Acta* **44**, 3969–3976 (1999). URL <http://www.sciencedirect.com/science/article/pii/S0013468699001723>.
- [186] Stöhr, J. *et al.* Images of the antiferromagnetic structure of a NiO(100) surface by means of x-ray magnetic linear dichroism spectromicroscopy. *Phys. Rev. Lett.* **83**, 1862–1865 (1999). URL <https://doi.org/10.1103/PhysRevLett.83.1862>.
- [187] Wollschläger, J., Erdös, D., Goldbach, H., Höpken, R. & Schröder, K. M. Growth of NiO and MgO films on Ag(100). *Thin Solid Films* **400**, 1–8 (2001). URL <http://www.sciencedirect.com/science/article/pii/S0040609001014821>.
- [188] Caffio, M. *et al.* Ultrathin nickel oxide films grown on Ag(001): a study by XPS, LEIS and LEED intensity analysis. *Surf. Sci.* **531**, 368–374 (2003). URL [http://dx.Doi.org/10.1016/S0039-6028\(03\)00544-2](http://dx.Doi.org/10.1016/S0039-6028(03)00544-2).
- [189] Finazzi, M. *et al.* Magnetic anisotropy of NiO epitaxial thin films on Fe(001). *Phys. Rev. B* **69**, 014410 (2004). URL <http://dx.Doi.org/10.1103/PhysRevB.69.014410>.
- [190] Giovanardi, C., di Bona, A. & Valeri, S. Oxygen-dosage effect on the structure and composition of ultrathin NiO layers reactively grown on Ag(001). *Phys. Rev. B* **69**, 075418 (2004). URL <http://dx.Doi.org/10.1103/PhysRevB.69.075418>.
- [191] Caffio, M., Atrei, A., Cortigiani, B. & Rovida, G. STM study of the nanostructures prepared by deposition of NiO on Ag(001). *J. Phys.: Condens. Matter* **18**, 2379–2384 (2006). URL <http://stacks.iop.org/0953-8984/18/i=8/a=003>.
- [192] Steurer, W., Surnev, S., Fortunelli, A. & Netzer, F. P. Scanning tunneling microscopy imaging of NiO(100)(1×1) islands embedded in Ag(100). *Surf. Sci.* **606**, 803–807 (2012). URL <http://www.sciencedirect.com/science/article/pii/S0039602812000283>.
- [193] Barlow, S. & Raval, R. Complex organic molecules at metal surfaces: bonding, organisation and chirality. *Surf. Sci. Rep.* **50**, 201–341 (2003). URL <http://www.sciencedirect.com/science/article/pii/S0167572903000153>.

Bibliography

- [194] Nony, L. *et al.* Dipole-driven self-organization of zwitterionic molecules on alkali halide surfaces. *Beilstein Journal of Nanotechnology* **3**, 285–293 (2012). URL <https://www.beilstein-journals.org/bjnano/articles/3/32>.
- [195] Momper, R., Nalbach, M., Lichtenstein, K., Bechstein, R. & Kühnle, A. Stabilization of polar step edges on calcite (10.4) by the adsorption of congo red. *Langmuir* **31**, 7283–7287 (2015). URL <https://doi.org/10.1021/acs.langmuir.5b01043>.
- [196] Hoffmann, R., Kantorovich, L. N., Baratoff, A., Hug, H. J. & Güntherodt, H.-J. Sublattice identification in scanning force microscopy on alkali halide surfaces. *Phys. Rev. Lett.* **92**, 146103 (2004). URL <https://doi.org/10.1103/PhysRevLett.92.146103>.
- [197] Kantorovich, L. N., Shluger, A. L. & Stoneham, A. M. Recognition of surface species in atomic force microscopy: Optical properties of a Cr^{3+} defect at the $\text{MgO}(001)$ surface. *Phys. Rev. B* **63**, 184111 (2001). URL <https://doi.org/10.1103/PhysRevB.63.184111>.
- [198] Foster, A. & Shluger, A. Spin-contrast in non-contact SFM on oxide surfaces: theoretical modelling of $\text{NiO}(001)$ surface. *Surface Science* **490**, 211–219 (2001). URL <http://www.sciencedirect.com/science/article/pii/S0039602801013346>.
- [199] Teobaldi, G. *et al.* Chemical resolution at ionic crystal surfaces using dynamic atomic force microscopy with metallic tips. *Phys. Rev. Lett.* **106**, 216102 (2011). URL <https://doi.org/10.1103/PhysRevLett.106.216102>.
- [200] Yurtsever, A., Sugimoto, Y., Abe, M. & Morita, S. Nc-AFM imaging of the $\text{TiO}_2(110)-(1\times 1)$ surface at low temperature. *Nanotechnology* **21**, 165702 (2010). URL <http://stacks.iop.org/0957-4484/21/i=16/a=165702>.
- [201] Gross, L. *et al.* Investigating atomic contrast in atomic force microscopy and Kelvin probe force microscopy on ionic systems using functionalized tips. *Phys. Rev. B* **90**, 155455 (2014). URL <https://link.aps.org/doi/10.1103/PhysRevB.90.155455>.
- [202] Rahe, P. *et al.* Transition of molecule orientation during adsorption of terephthalic acid on rutile $\text{TiO}_2(110)$. *J. Phys. Chem. C* **113**, 17471–17478 (2009). URL <http://dx.Doi.org/10.1021/jp9052117>.
- [203] Rahe, P. *et al.* Tuning molecular self-assembly on bulk insulator surfaces by anchoring of the organic building blocks. *Adv. Mater.* **25**, 3948–3956 (2013). URL <https://Doi.org/10.1002/adma.201300604>.
- [204] Such, B. *et al.* Functionalized truxenes: Adsorption and diffusion of single molecules on the $\text{KBr}(001)$ surface. *ACS Nano* **4**, 3429–3439 (2010). URL <http://dx.Doi.org/10.1021/nn100424g>.
- [205] Chen, W., Tegenkamp, C., Pfnür, H. & Bredow, T. Tailoring band gaps of insulators by adsorption at surface defects: Benzoic acids on NaCl surfaces. *Phys. Rev. B* **79**, 235419 (2009). URL <https://doi.org/10.1103/PhysRevB.79.235419>.
- [206] Hinaut, A. *et al.* An nc-AFM and KPFM study of the adsorption of a triphenylene derivative on $\text{KBr}(001)$. *Beilstein J. Nanotechnol.* **3**, 221–229 (2012). URL <http://dx.Doi.org/10.3762/bjnano.3.25>.

- [207] Nony, L. *et al.* Observation of individual molecules trapped on a nanostructured insulator. *Nano Lett.* **4**, 2185–2189 (2004). URL <http://dx.Doi.org/10.1021/nl048693v>.
- [208] Mativetsky, J. M., Burke, S. A., Fostner, S. & Grutter, P. Nanoscale pits as templates for building a molecular device. *Small* **3**, 818–821 (2007). URL <https://Doi.org/10.1002/sml.200600699>.
- [209] Naldoni, A. *et al.* Effect of nature and location of defects on bandgap narrowing in black TiO₂ nanoparticles. *J. Am. Chem. Soc.* **134**, 7600–7603 (2012). URL <https://Doi.org/10.1021/ja3012676>.
- [210] Batzill, M., Morales, E. H. & Diebold, U. Influence of nitrogen doping on the defect formation and surface properties of TiO₂ rutile and anatase. *Phys. Rev. Lett.* **96**, 026103 (2006). URL <https://doi.org/10.1103/PhysRevLett.96.026103>.
- [211] Atkinson, A. & Taylor, R. I. The self-diffusion of Ni in NiO and its relevance to the oxidation of Ni. *Journal of Materials Science* **13**, 427–432 (1978). URL <https://doi.org/10.1007/BF00647789>.
- [212] Atkinson, A., Taylor, R. I. & Goode, P. D. Transport processes in the oxidation of Ni studied using tracers in growing NiO scales. *Oxidation of Metals* **13**, 519–543 (1979). URL <https://doi.org/10.1007/BF00812776>.
- [213] Atkinson, A. & Taylor, R. I. The diffusion of ⁶³Ni along grain boundaries in nickel oxide. *Philosophical Magazine A* **43**, 979–998 (1981). URL <https://doi.org/10.1080/01418618108239506>.
- [214] Barbier, F., Monty, C. & Déchamps, M. On the grain boundary diffusion of Co in NiO bicrystals. *Philosophical Magazine A* **58**, 475–490 (1988). URL <https://doi.org/10.1080/01418618808210425>.
- [215] Ikeda, M., Koide, N., Han, L., Sasahara, A. & Onishi, H. Scanning tunneling microscopy study of black dye and deoxycholic acid adsorbed on a rutile TiO₂(110). *Langmuir* **24**, 8056–8060 (2008). URL <http://dx.Doi.org/10.1021/la8010019>.
- [216] Setvin, M. *et al.* A multitechnique study of CO adsorption on the TiO₂ anatase (101) surface. *J. Phys. Chem. C* **119**, 21044–21052 (2015). URL <http://dx.Doi.org/10.1021/acs.jpcc.5b07999>.
- [217] Wood, C. J. *et al.* A comprehensive comparison of dye-sensitized NiO photocathodes for solar energy conversion. *Phys. Chem. Chem. Phys.* **18**, 10727–10738 (2016). URL <http://dx.Doi.org/10.1039/C5CP05326A>.
- [218] Imahori, H. *et al.* Photoinduced charge carrier dynamics of Zn–porphyrin–TiO₂ electrodes: The key role of charge recombination for solar cell performance. *J. Phys. Chem. A* **115**, 3679–3690 (2011). URL <https://Doi.org/10.1021/jp103747t>.
- [219] Morandeira, A., Boschloo, G., Hagfeldt, A. & Hammarström, L. Coumarin 343–NiO films as nanostructured photocathodes in dye-sensitized solar cells: Ultrafast electron transfer, effect of the I₃[−]/I[−] redox couple and mechanism of photocurrent generation. *J. Phys. Chem. C* **112**, 9530–9537 (2008). URL <https://Doi.org/10.1021/jp800760q>.

Bibliography

- [220] Weckesser, J., De Vita, A., Barth, J. V., Cai, C. & Kern, K. Mesoscopic correlation of supramolecular chirality in one-dimensional hydrogen-bonded assemblies. *Phys. Rev. Lett.* **87**, 096101 (2001). URL <https://doi.org/10.1103/PhysRevLett.87.096101>.
- [221] Chen, Q. & Richardson, N. V. Enantiomeric interactions between nucleic acid bases and amino acids on solid surfaces. *Nat Mater* **2**, 324–328 (2003). URL <http://dx.Doi.org/10.1038/nmat878>.
- [222] Böhringer, M., Schneider, W.-D. & Berndt, R. Real space observation of a chiral phase transition in a two-dimensional organic layer. *Angew. Chem. Int. Ed.* **39**, 792–795 (2000). URL [http://dx.Doi.org/10.1002/\(SICI\)1521-3773\(20000218\)39:4<792::AID-ANIE792>3.0.CO;2-2](http://dx.Doi.org/10.1002/(SICI)1521-3773(20000218)39:4<792::AID-ANIE792>3.0.CO;2-2).
- [223] Brian France, C. & Parkinson, B. A. Naphtho[2,3-*a*]pyrene forms chiral domains on Au(111). *J. Am. Chem. Soc.* **125**, 12712–12713 (2003). URL <http://dx.Doi.org/10.1021/ja037056o>.
- [224] Weigelt, S. *et al.* Chiral switching by spontaneous conformational change in adsorbed organic molecules. *Nat Mater* **5**, 112–117 (2006). URL <http://dx.Doi.org/10.1038/nmat1558>.
- [225] Sadewasser, S. & Glatzel, T. *Kelvin Probe Force Microscopy: Measuring and compensating electrostatic forces* (Springer Series in Surface Science, 2011).
- [226] Malzner, F., Housecroft, C. E. & Constable, E. C. The versatile SALSAC approach to heteroleptic copper(i) dye assembly in dye-sensitized solar cells. *Inorganics* **6**, 57 (2018). URL <http://www.mdpi.com/2304-6740/6/2/57>.
- [227] Schönhofer, E. *et al.* Surfaces-as-ligands, surfaces-as-complexes strategies for copper(i) dye-sensitized solar cells. *Dyes and Pigments* **115**, 154–165 (2015). URL <http://www.sciencedirect.com/science/article/pii/S0143720814004823>.
- [228] Bozic-Weber, B. *et al.* The intramolecular aryl embrace: from light emission to light absorption. *Dalton Trans.* **40**, 12584–12594 (2011). URL <http://dx.Doi.org/10.1039/C1DT11052G>.
- [229] Malzner, F. J., Prescimone, A., Constable, E. C., Housecroft, C. E. & Willgert, M. Exploring simple ancillary ligands in copper-based dye-sensitized solar cells: effects of a heteroatom switch and of co-sensitization. *J. Mater. Chem. A* **5**, 4671–4685 (2017). URL <http://dx.Doi.org/10.1039/C6TA10947K>.
- [230] Zimmerli, L. *et al.* Formation of molecular wires on nanostructured KBr. *Journal of Physics: Conference Series* **61**, 1357–1360 (2007). URL <http://stacks.iop.org/1742-6596/61/i=1/a=268>.
- [231] Kunstmann, T. *et al.* Dynamic force microscopy study of 3,4,9,10-perylenetetracarboxylic dianhydride on KBr(001). *Phys. Rev. B* **71**, 121403 (2005). URL <http://dx.Doi.org/10.1103/PhysRevB.71.121403>.
- [232] Burke, S. A., Topple, J. M. & Grütter, P. Molecular dewetting on insulators. *J. Phys.: Condens. Matter* **21**, 423101 (2009). URL <http://stacks.iop.org/0953-8984/21/i=42/a=423101>.

- [233] Kawai, S. *et al.* Organometallic bonding in an ullmann-type on-surface chemical reaction studied by high-resolution atomic force microscopy. *Small* **12**, 5303–5311 (2016). URL <https://doi.org/10.1002/smll.201601216>.
- [234] Kocić, N. *et al.* Control of reactivity and regioselectivity for on-surface dehydrogenative aryl-aryl bond formation. *J. Am. Chem. Soc.* **138**, 5585–5593 (2016). URL <https://doi.org/10.1021/jacs.5b13461>.
- [235] Zint, S. *et al.* Imaging successive intermediate states of the on-surface Ullmann reaction on Cu(111): Role of the metal coordination. *ACS Nano* **11**, 4183–4190 (2017). URL <https://doi.org/10.1021/acsnano.7b01109>.
- [236] Pawlak, R. *et al.* Design and characterization of an electrically powered single molecule on gold. *ACS Nano* **11**, 9930–9940 (2017). URL <https://doi.org/10.1021/acsnano.7b03955>.
- [237] Shchyrba, A. *et al.* Chirality transfer in 1d self-assemblies: Influence of H-bonding vs metal coordination between dicyano[7]helicene enantiomers. *J. Am. Chem. Soc.* **135**, 15270–15273 (2013). URL <https://doi.org/10.1021/ja407315f>.
- [238] Meier, T. *et al.* Donor-acceptor properties of a single-molecule altered by on-surface complex formation. *ACS Nano* **11**, 8413–8420 (2017). URL <https://doi.org/10.1021/acsnano.7b03954>.
- [239] Vera, F. *et al.* Preparation and characterization of eosin B- and erythrosin J-sensitized nanostructured NiO thin film photocathodes. *Thin Solid Films* **490**, 182 – 188 (2005). URL <http://www.sciencedirect.com/science/article/pii/S0040609005004220>.
- [240] Qin, P. *et al.* Design of an organic chromophore for p-type dye-sensitized solar cells. *Journal of the American Chemical Society* **130**, 8570–8571 (2008). URL <http://dx.doi.org/10.1021/ja8001474>.
- [241] Qin, P. *et al.* High incident photon-to-current conversion efficiency of p-type dye-sensitized solar cells based on NiO and organic chromophores. *Adv. Mater.* **21**, 2993–2996 (2009). URL <http://dx.doi.org/10.1002/adma.200802461>.
- [242] Qin, P. *et al.* Synthesis and mechanistic studies of organic chromophores with different energy levels for p-type dye-sensitized solar cells. *The Journal of Physical Chemistry C* **114**, 4738–4748 (2010). URL <https://doi.org/10.1021/jp911091n>. <https://doi.org/10.1021/jp911091n>.
- [243] Li, L. *et al.* Double-layered NiO photocathodes for p-type DSSCs with record IPCE. *Advanced Materials* **22**, 1759–1762 (2010). URL <https://doi.org/10.1002/adma.200903151>. <https://onlinelibrary.wiley.com/doi/pdf/10.1002/adma.200903151>.
- [244] Satterley, C. J. *et al.* Electrospray deposition of fullerenes in ultra-high vacuum: in situ scanning tunneling microscopy and photoemission spectroscopy. *Nanotechnology* **18**, 455304 (2007). URL <http://stacks.iop.org/0957-4484/18/i=45/a=455304>.
- [245] Mayor, L. C. *et al.* Adsorption of a Ru(ii) dye complex on the Au(111) surface: Photoemission and scanning tunneling microscopy. *J. Chem. Phys.* **130**, 164704 (2009). URL <http://dx.doi.org/10.1063/1.3122685>.

Bibliography

- [246] Hauptmann, N., Hamann, C., Tang, H. & Berndt, R. Soft-landing electrospray deposition of the ruthenium dye N3 on Au(111). *J. Phys. Chem. C* **117**, 9734–9738 (2013). URL <http://dx.Doi.org/10.1021/jp311420d>.
- [247] O’Shea, J. N. *et al.* Hydrogen-bond induced surface core-level shift in isonicotinic acid. *J. Phys. Chem. B* **105**, 1917–1920 (2001). URL <https://doi.org/10.1021/jp003675x>.
- [248] Mayor, L. C. *et al.* Photoemission, resonant photoemission, and x-ray absorption of a Ru(ii) complex adsorbed on rutile TiO₂(110) prepared by in situ electrospray deposition. *J. Chem. Phys.* **129**, hin (2008). URL <http://dx.Doi.org/10.1063/1.2975339>.
- [249] Weston, M., Britton, A. J. & O’Shea, J. N. Charge transfer dynamics of model charge transfer centers of a multicenter water splitting dye complex on rutile TiO₂(110). *The Journal of Chemical Physics* **134**, 054705– (2011). URL <https://Doi.org/10.1063/1.3549573>.
- [250] Weston, M., Reade, T. J., Handrup, K., Champness, N. R. & O’Shea, J. N. Adsorption of dipyrin-based dye complexes on a rutile TiO₂(110) surface. *J. Phys. Chem. C* **116**, 18184–18192 (2012). URL <https://doi.org/10.1021/jp3025864>.
- [251] Kroto, H. W., Allaf, A. W. & Balm, S. P. C₆₀: Buckminsterfullerene. *Chem. Rev.* **91**, 1213–1235 (1991). URL <https://pubs.acs.org/doi/abs/10.1021/cr00006a005>.
- [252] Lu, X., Grobis, M., Khoo, K. H., Louie, S. G. & Crommie, M. F. Charge transfer and screening in individual C₆₀ molecules on metal substrates: A scanning tunneling spectroscopy and theoretical study. *Phys. Rev. B* **70**, 115418 (2004). URL <http://dx.Doi.org/10.1103/PhysRevB.70.115418>.
- [253] Schull, G., Néel, N., Becker, M., Kröger, J. & Berndt, R. Spatially resolved conductance of oriented C₆₀. *New Journal of Physics* **10**, 065012 (2008). URL <http://stacks.iop.org/1367-2630/10/i=6/a=065012>.
- [254] Samuely, T. *et al.* Self-assembly of individually addressable complexes of C₆₀ and phthalocyanines on a metal surface: Structural and electronic investigations. *J. Phys. Chem. C* **113**, 19373–19375 (2009). URL <https://doi.org/10.1021/jp908086p>.
- [255] Pawlak, R., Kawai, S., Fremy, S., Glatzel, T. & Meyer, E. Atomic-scale mechanical properties of orientated C₆₀ molecules revealed by noncontact atomic force microscopy. *ACS Nano* **5**, 6349–6354 (2011). URL <http://dx.Doi.org/10.1021/nn201462g>.
- [256] Pawlak, R., Kawai, S., Fremy, S., Glatzel, T. & Meyer, E. High-resolution imaging of C₆₀ molecules using tuning-fork-based non-contact atomic force microscopy. *J. Phys.: Condens. Matter* **24**, 084005 (2012). URL <http://stacks.iop.org/0953-8984/24/i=8/a=084005>.
- [257] Gross, L. *et al.* Bond-order discrimination by atomic force microscopy. *Science* **337**, 1326–1329 (2012). URL <http://science.sciencemag.org/content/337/6100/1326>.
- [258] Hashizume, T. *et al.* Intramolecular structures and of C₆₀ and molecules adsorbed and on the Cu(111) and (1×1) and surface. *Phys. Rev. Lett.* **71**, 2959–2962 (1993). URL <https://journals.aps.org/prl/abstract/10.1103/PhysRevLett.71.2959>.

- [259] Altman, E. I. & Colton, R. J. Determination of the orientation of C₆₀ adsorbed on Au(111) and Ag(111). *Phys. Rev. B* **48**, 18244–18249 (1993). URL <https://doi.org/10.1103/PhysRevB.48.18244>.
- [260] Mativetsky, J. M., Burke, S. A., Hoffmann, R., Sun, Y. & Grutter, P. Molecular resolution imaging of C₆₀ on Au(111) by non-contact atomic force microscopy. *Nanotechnology* **15**, S40–S43 (2004). URL <http://stacks.iop.org/0957-4484/15/i=2/a=009>.
- [261] Kobayashi, K., Yamada, H., Horiuchi, T. & Matsushige, K. Investigations of C₆₀ molecules deposited on Si(111) by noncontact atomic force microscopy. *Appl. Surf. Sci.* **140**, 281 – 286 (1999). URL <http://www.sciencedirect.com/science/article/pii/S0169433298005418>.
- [262] Sanvitto, D., De Seta, M. & Evangelisti, F. Growth of thin C₆₀ films on hydrogenated Si(100) surfaces. *Surf. Sci.* **452**, 191–197 (2000). URL <http://www.sciencedirect.com/science/article/pii/S0039602800003216>.
- [263] Lüthi, R. *et al.* Sled-type motion on the nanometer scale: Determination of dissipation and cohesive energies of C₆₀. *Science* **266**, 1979–1981 (1994). URL <http://www.sciencemag.org/content/266/5193/1979>.
- [264] Burke, S., Mativetsky, J., Hoffmann, R. & Grütter, P. Nucleation and submonolayer growth of C₆₀ on KBr. *Phys. Rev. Lett.* **94**, 096102 (2005). URL <http://dx.Doi.org/10.1103/PhysRevLett.94.096102>.
- [265] Burke, S., Mativetsky, J., Fostner, S. & Grütter, P. C₆₀ on alkali halides: Epitaxy and morphology studied by noncontact AFM. *Phys. Rev. B* **76**, 035419 (2007). URL <http://dx.Doi.org/10.1103/PhysRevB.76.035419>.
- [266] Loske, F., Lübke, J., Schütte, J., Reichling, M. & Kühnle, A. Quantitative description of C₆₀ diffusion on an insulating surface. *Phys. Rev. B* **82**, 155428 (2010). URL <http://dx.Doi.org/10.1103/PhysRevB.82.155428>.
- [267] Loske, F., Reichling, M. & Kühnle, A. Steering molecular island morphology on an insulator surface by exploiting sequential deposition. *Chem. Commun.* **47**, 10386–10388 (2011). URL <http://dx.Doi.org/10.1039/C1CC12996A>.
- [268] Loske, F., Reichling, M. & Kühnle, A. Deposition sequence determines morphology of C₆₀ and 3,4,9,10-perylenetetracarboxylic diimide islands on CaF₂(111). *Jpn. J. Appl. Phys.* **50**, 08LB07 (2011). URL <http://stacks.iop.org/1347-4065/50/i=8S3/a=08LB07>.
- [269] Körner, M. *et al.* Second-layer induced island morphologies in thin-film growth of fullerenes. *Phys. Rev. Lett.* **107**, 016101 (2011). URL <http://dx.Doi.org/10.1103/PhysRevLett.107.016101>.
- [270] Rahe, P., Lindner, R., Kittelmann, M., Nimmrich, M. & Kühnle, A. From dewetting to wetting molecular layers: C₆₀ on CaCO₃(10 $\bar{1}$ 4) as a case study. *Phys. Chem. Chem. Phys.* **14**, 6544–6548 (2012). URL <http://dx.Doi.org/10.1039/C2CP40172J>.
- [271] Freund, S. *et al.* Morphology change of C₆₀ islands on organic crystals observed by atomic force microscopy. *ACS Nano* **10**, 5782–5788 (2016). URL <http://dx.Doi.org/10.1021/acsnano.5b07971>.

Bibliography

- [272] Beton, P. H., Dunn, A. W. & Moriarty, P. Manipulation of C₆₀ molecules on a Si surface. *Appl. Phys. Lett.* **67**, 1075–1077 (1995). URL [http://dx.Doi.org/10.1063/1.114469](http://dx.doi.org/10.1063/1.114469).
- [273] Dunn, A. W. C₆₀ manipulation and cluster formation using a scanning tunneling microscope. *J. Vac. Sci. Technol. B* **14**, 1596–1599 (1996). URL <http://dx.Doi.org/10.1116/1.589197>.
- [274] Moriarty, P., Ma, Y., Upward, M. & Beton, P. Translation, rotation and removal of C₆₀ on Si(100)–(2×1) using anisotropic molecular manipulation. *Surface Science* **407**, 27–35 (1998). URL <http://www.sciencedirect.com/science/article/pii/S003960289800082X>.
- [275] Saywell, A. *et al.* Electrospray deposition of C₆₀ on a hydrogen-bonded supramolecular network. *J. Phys. Chem. C* **112**, 7706–7709 (2008). URL <https://doi.org/10.1021/jp7119944>.
- [276] Červenka, J. & Flipse, C. F. J. Fullerene monolayer formation by spray coating. *Nanotechnology* **21**, 065302 (2010). URL <http://stacks.iop.org/0957-4484/21/i=6/a=065302>.
- [277] Scherb, S. *UHV AFM and STM studies of electrospray deposited graphene-like molecules*. Master’s thesis, University of Basel, Faculty of Science (2018).

List of Figures

i.1	Principle of DSSC	2
1.1	Schematic representation of a STM	6
1.2	Schematic representation of a nc-AFM	7
1.3	Interaction forces	8
1.4	Oscillation modes and multimodal AFM	10
1.5	Multipass AFM	12
1.6	Contact potential difference	13
1.7	Schematic representation of an FM-KPFM	14
1.8	Average CPD difference determination	15
2.1	Experimental set-up	18
2.2	The microscope	19
2.3	Measurement control	20
2.4	The cantilevers	21
2.5	Cleaver set-up	22
2.6	Dye precursor and dye molecules	24
2.7	Electrospray set-up	26
3.1	Preparation methods of NiO samples	32
3.2	The surface of TiO ₂ (110)	33
3.3	The surface of MgO(001)	34
3.4	The surface of NiO(001)	35
3.5	Porphyrin molecules adsorbed on TiO ₂ (110)	36
3.6	Palladium clusters formed on MgO(001)	37
3.7	Co-Salen molecules adsorbed on NiO(001)	38
4.1	Large scale imaging of NiO(001)	40
4.2	Atomic resolution on NiO(001)	41
4.3	Preparation process induces tunable line defects	43
4.4	Atomic resolution on line defects	44

List of Figures

5.1	Chemical structure of Cu–TCPP and C343	48
5.2	Cu–TCPP adsorbed on NiO(001)	49
5.3	Submolecular resolution on a Cu–TCPP island	50
5.4	Molecular orientations of type 1 and 2 islands	51
5.5	C343 adsorbed on NiO(001)	52
5.6	C343 islands on NiO(001)	54
5.7	CPD on Cu–TCPP adsorbed on NiO	56
5.8	CPD on C343 adsorbed on NiO	57
6.1	On–surface reaction	60
6.2	Annealing effect on the binding energy of DCPDM(bpy) to NiO(001)	61
6.3	Single DCPDM(bpy) molecules on NiO(001) at RT	62
6.4	Windmill cluster on NiO(001) at RT	63
6.5	Annealing effect on the morphology of assemblies	64
6.6	DCPDM(bpy) islands on NiO(001) at RT	65
6.7	Successive Fe and DCPDM(bpy) depositions	66
6.8	Single Fe–DCPDM(bpy) molecules on NiO(001) at RT	67
6.9	The transoid configurations of DCPDM(bpy) imaged at LT	68
6.10	The cisoid configurations of Fe–DCPDM(bpy) imaged at LT	69
6.11	Effect of annealing and metal coordination	71
7.1	Structures of P1, Ru(bpy) ₂ (H1) and Ru(bpy) ₂ (H2)	74
7.2	Chemical structure of C ₆₀	75
7.3	Comparison between sublimation and spray deposition for the functionalization of NiO(001) with C ₆₀ molecules	76
7.4	The reference dye molecule P1	78
7.5	Ru(bpy) ₂ (H1) adsorbed on NiO	79
7.6	Ru(bpy) ₂ (H2) adsorbed on NiO	80

List of Tables

5.1	Parameters measured and calculated for Cu-TCPP islands types. . . .	51
5.2	Parameters measured and calculated for the C343 island	54
5.3	Comparison between Cu-TCPP and C343 adsorbed on NiO(001) . . .	57
6.1	Effect of Fe and annealing on the conformation of DCPDMbpy	71

Nomenclature

Symbols

Latin letters

A	Amplitude
A_1	Oscillation amplitude of the eigenmode
A_2	Oscillation amplitude of the second flexural mode
A_{TR}	Oscillation amplitude of the torsional mode
A_H	Hamaker constant
a, b	Lattice parameters
C	Capacitance of plate capacitor
D	Molecular density
E	Energy
E_{bond}	Bonding energy
E_F	Fermi energy
$E_{F,T}$	Fermi energy of the tip
$E_{F,S}$	Fermi energy of the sample
e	Elementary charge
e^-	Electron
F	Force
F_{chem}	Chemical force between tip and sample
F_{elec}	Electrostatic force
F_i	Interaction force
F_{TOT}	Total tip-sample force
F_{vdW}	Van der Waals force
f	Frequency
f_1	Eigenfrequency
f_2	Second flexural frequency
f_{TR}	Torsional frequency

Nomenclature

h	Height
h_{step}	Step height
h_{defect}	Defect height
I_t	Tunneling current
p	Dipole moment
Q	Quality factor
R	Radius of curvature of the tip
U	Potential difference between tip and sample
V_{AC}	Alternative current voltage
V_{BIAS}	Bias voltage
V_{CPD}	Voltage compensating the contact potential difference
V_{DC}	Direct current voltage
x	Coordinate of one horizontal axis in the sample surface plane
y	Coordinate of one horizontal axis in the sample surface plane
z	Coordinate of the vertical axis between tip and sample
z_{offset}	Offset distance

Greek letters

α, β	Opposite chiralities
Δf	Frequency shift
$\Delta\phi$	Work function difference
Δp	Dipole moment density difference
ΔV_{CPD}	Average CPD difference
$\delta+$	Positive partial charge
$\delta-$	Negative partial charge
ϵ_0	Vacuum permittivity
θ	Angle between the lattice vectors
κ	Decay length of bounding interaction
ρ	Angle along which the molecular rows are aligned with respect to the [010] direction
σ	Equilibrium distance
ϕ	Work function
ϕ_T	Work function of the tip
ϕ_S	Work function of the sample
φ_{clear}	Clearance angle
φ_{cut}	Cutting angle
ω	Angular frequency of the oscillation

Abbreviations

AC	Alternative current
AFM	Atomic force microscopy/microscope
AM	Amplitude-modulation
BE	Binding energy
bpy	2,2'-bipyridine
C343	Coumarin 343
CB	Conduction band
CPD	Contact potential difference
Cu-TCPP	Copper(II)meso-tetra(4-carboxyphenyl)porphyrin
DC	Direct current
DCPDM(bpy)	4,4'-di(4-carboxyphenyl)-6,6'-dimethyl-2,2'-bipyridine
DSSC	Dye sensitized solar cell
ESD	Electrospray deposition
Fe-DCPDM(bpy)	Iron coordinated 4,4'-di(4-carboxyphenyl)-6,6'-dimethyl-2,2'-bipyridine
FFT	Fast Fourier transform
FM	Frequency-modulation
FTO	Fluorin doped tin oxide
HOMO	Highest occupied molecular orbital
H1	4-(2-phenylpyridin-4-yl)phenyl)phosphonic acid
H2	4-(2-phenylpyridin-4-yl)phenyl)carboxylic acid
ITO	Indium tin oxide
KPFM	Kelvin Probe Force Microscopy
LUMO	Highest unoccupied molecular orbital
LT	Low temperature
M-DCPDM(bpy)	Metal coordinated 4,4'-di(4-carboxyphenyl)-6,6'-dimethyl-2,2'-bipyridine
ML	Monolayer
nc	Non contact
P1	4-(Bis-{4-[5-(2,2-dicyano-vinyl)-thiophene-2-yl]-phenyl}-amino)-benzoic acid
PLL	Phase locked loop
QMB	Quartz micro balance
QPD	Quadrant photo diode
RT	Room temperature
Ru(bpy) ₂ (H1)	Bis(2,2'-bipyridine)-[4-(2-phenylpyridin-4-yl)phenyl)phosphonic acid]ruthenium
Ru(bpy) ₂ (H2)	Bis(2,2'-bipyridine)-[4-(2-phenylpyridin-4-yl)phenyl)carboxylic acid]ruthenium
SALSAC	Surface-as-ligand surface-as-complex

Nomenclature

SLD	Supralum diode
SPM	Scanning probe microscopy/microscope
STM	Scanning tunneling microscopy/microscope
TCO	Transparent conductive oxides
UHV	Ultra-high vacuum
VB	Valence band
XPS	X-ray photoelectron spectroscopy
2D	Two-dimensional
3D	Three-dimensional

Acknowledgements

BEFORE starting to write down these acknowledgements, I would like to apologise in advance because I already know that it will be impossible to cite an exhaustive list of all the persons who contributed directly or indirectly to this work (otherwise this thesis will be thicker than a dictionary). However, even if I will have to abbreviate the roll, I know that I won't succeed to keep it short... Sorry for that!

First of all, I would like to thank Prof. Ernst Meyer who created such a nice working environment in his research group. As I started my master thesis under his supervision, I did not intend to stay for a PhD, but I quickly changed my mind and never regretted my choice. In a way, I probably took the best decision of my life when I decided to stay, not only because of all what I learned in the lab but also in terms of personal development. And I have to admit that, if it would be possible, I would even sign for a second PhD in his group!

Second, my grateful thanks go to Dr. Thilo Glatzel, without whom, my PhD adventure would not have been possible. He led the project I was working on with a lot of enthusiasm, constantly finding new ideas and was a real support during my entire PhD. Besides this, Thilo also gave me the chance to participate to several outreach activities in parallel to my research, especially to the kids@science weeks, which was for me a lot of fun! Thank you also for that!

Because, this thesis is the result of a fruitful collaboration between our team and the group of Prof. Catherine Housecroft and Prof. Edwin Constable, I would like to thank all my colleagues from the Chemistry department of the University of Basel. In particular, I am grateful to Prof. Catherine Housecroft, who co-led the project, hosted me so many times in her office to answer my stupid questions about chemistry and also corrected so carefully my paper drafts. I would like to thank as well Prof. Edwin Constable for his productive remarks during our monthly meetings and for his constant presence throughout the paper writing process despite his busy calendar. My special thanks go finally to Nathalie Marinakis who was my official molecule supplier during my entire PhD!

For having introduced me to the field of nc-AFM, I thank Dr. Antoine Hinaut. He

Acknowledgements

was always around when I needed advices or help in the lab. He also proof read all my paper drafts and this thesis. The major part of the experimental skills I acquired during my master and PhD, I owe you. Thank you also for the organisation of the BBQs, even if half of them were taking place under the rain!

Since all the present work would not have been possible without administrative and technical support, I further would like to acknowledge Germaine Weaver, Barbara Kammermann, Astrid Kalt as well as Beatrice Erismann but also Roberto Maffioli, Andreas Tonin, Michael Steinacher, Marco Martina, Sascha Martin and the teams of the electronic and mechanical workshop. I really appreciated to work with all of you!

In addition, I also would like to thank all the actual and former members of the group for the good atmosphere which was always prevailing since I started: Dr. Res Jöhr, for all the time spent together in the lab; Zhao Liu, Sebastian Scherb and Mauro Spreiter, for forming such a great new team in the RT lab; Carl Drechsel, Philipp D'Astolfo and Dr. Gui Vilhena (I hope you do not mind if I shorted your name, but seriously...?), for the good ambience in our office; Roland Steiner, for his precious expertise when technical help was needed but also for the overdrive (!); Yves Pellemont for his priceless engineering support; Dr. Laurent Marot, for the security mastering (sorry, I could not resist!); Prof. Alexis Baratoff, for being always ready to share his incredible knowledge about physics in general; Dr. Marcin Kisiel, Dr. Lucas Moser and Dr. Rémy Pawlak, the three members of the, self-proclaimed, "project Manhattan office", for their support, help and valuable advices but also their sense of humour, which is even more striking when they practice it as a team; and last but not least the girls crew formed by Marwa Ben Yaala and Dilek Yildiz, for all the moments we shared and for the delicious sweets they were bringing from Tunisia and Turkey (I don't forget Plan B!).

My special thank goes also, of course, to Dr. Tobias Meier who was my PhD mate from the beginning on. We passed through the PhD together, sharing our experiences and doubts but also tons of cookies during our legendary 4 o'clock breaks. It was a real pleasure to work with you during these four years and I have to admit that it feels strange to finish the PhD without you sitting just next to me in the office. I already miss you!

To Olha Popova (alias unicorn queen, lama rider) who, literally, was my sunshine in the physics department, I want to say thank you for letting me discover who is actually hidden behind the smile and loud chatting. You are an amazing person, don't doubt it (OO).

Even if I spend most of my time during these past four years with my colleagues, my family also deserves a heartfelt thank you. They always believed in me, and even if it was not always easy to fulfil their expectations, I tried to do my best. What I accomplished till today, I also owe you! I grew up as a single child, but thanks to all of you (sorry, it would be impossible to cite you all), and because it has always been a principle in our family to raise kids like if they were members of a pack of wolves, I never felt lonely.

I am especially grateful to my cousins, for the great times we had and we still have each time we are together. Julien, thank you for never having gave up on me, even during the worst times. It feels good to always have someone on your side, even if

you are wrong. Thank you for that! Max, thank you for our childhood, I am missing these times we spent together really a lot. I am still hoping that, one day, we will find again what we have lost. Anji, my twin sister, thank you for all our quarrels and reconciliations, thank you for all these nights we spent lying top to tail speaking about everything and nothing. Without you being you I would not be me. Lucas, thank you for being the one and only in this crowd understanding what I am doing. It is really nice to have someone with whom I can discuss about science without getting him bored. Robot, thank you for your jokes, your legendary good mood (except in the early morning), for our stars observation evenings and for all these bottles of wine we emptied together. I will never forget all these moments! Marinou, thank you some much for all what we shared since more than twenty years. I still remember you as a baby, and I am so proud of the person you became. Sophinsky, thank you for having been the child you were and for becoming the young woman you are. I miss you sometimes, but I know that you will stay my lovely “adaktiv Schwester” forever. Nath, thank you for having kept the same smiling face since the day you were born. To prove how much I care about you, let me simply add: “Leo is the greatest”. I hope you appreciate ;)

A big thank goes to Sam, who recently became, officially, a member of the family. Thank you for always being here and also for being at the origin of the two cutest faces in the world. Emmoune and Mano, please do not grow up too fast!

To Mimi, who kindly agreed to proofread my thesis, even if experimental physics is not her favourite topic, I would like to express all my gratitude not only for her corrections but also for being available whatever I need since forever. Thank you for that!

I also want to sincerely thank BBO, who was an incredible support during my entire PhD. Without realizing it, you helped me to keep my head above water so many times. Being always so optimistic and spontaneous, you taught me that the world is a real nice place where it feels good to live. I am looking forward for our future adventures.

And finally, thank you to my parents who invested so much time and love in me. It is not easy to express in words how much I am grateful for all what you did for me, but I will try to do my best... Mam, thank you for everything, from the stories you were reading to me each evening when I was a child, till these moments you were listening to me repeating my physics lessons for my exams, even if you did not understand a single word. Papou, thank you for all, from these funny Saturday mornings we spent together, till our philosophical discussions about life in general. Thank you so much to you both for having taught me to always give my best and to aim as high as possible. All what I achieved, from my first steps till this PhD thesis, I did to make you proud... I hope you are!

List of publications & communications

Peer-reviewed journal publications

1. **Freund, S.**; Hinaut, A.; Marinakis, N; Constable, E. C.; Meyer, E.; Housecroft, C. E. and Glatzel, Th. Comparing a porphyrin- and a coumarin-based dye adsorbed on NiO(001). *Beilstein Journal of Nanotechnology* **10**, 874-881 (2019). DOI: [10.3762/bjnano.10.88](https://doi.org/10.3762/bjnano.10.88).
2. **Freund, S.**; Pawlak, R.; Moser, L.; Hinaut, A.; Steiner, R.; Marinakis, N; Constable, E. C.; Meyer, E.; Housecroft, C. E. and Glatzel, Th. Transoid-to-Cisoid Conformation Changes of Single Molecules on Surfaces Triggered by Metal Coordination. *ACS Omega* **3**, 12851-12856 (2018). DOI: [10.1021/acsomega.8b01792](https://doi.org/10.1021/acsomega.8b01792)
3. Hinaut, A.; Meier, T.; Pawlak, R.; **Freund, S.**; Jöhr, R.; Glatzel, Th.; Decurtins, S.; Müllen, K.; Narita, A.; Liu, S.-X. and Meyer, E. Electrospray Deposition of Structurally Complex Molecules Revealed by Atomic Force Microscopy. *Nanoscale* **10**, 1337 (2018). DOI: [10.1039/C7NR06261C](https://doi.org/10.1039/C7NR06261C)
4. **Freund, S.**; Hinaut, A.; Marinakis, N; Constable, E. C.; Meyer, E.; Housecroft, C. E. and Glatzel, Th. Anchoring of a Dye Precursor on NiO(001) Studied by Non-Contact Atomic Force Microscopy. *Beilstein Journal of Nanotechnology* **9**, 242-249 (2017). DOI: [10.3762/bjnano.9.26](https://doi.org/10.3762/bjnano.9.26)
5. Hinaut, A.; Eren, B.; Steiner, R.; **Freund, S.**; Jöhr, R.; Glatzel, Th.; Meyer, E. and Kawai, S. Nanostructuring of an Alkali Halide Surface by Low Temperature Plasma Exposure. *Phys. Chem. Chem. Phys.* **19**, 16251-16256 (2017). DOI: [10.1039/C7CP02592K](https://doi.org/10.1039/C7CP02592K)
6. **Freund, S.**; Hinaut, A.; Pawlak, R; Liu, X.-S.; Decurtins, S.; Meyer, E. and Glatzel, Th. Morphology Change of C₆₀ Islands on Organic Crystals Observed by Atomic Force Microscopy. *ACS Nano* **10**, 5782-5788 (2016). DOI: [10.3762/bjnano.9.26](https://doi.org/10.3762/bjnano.9.26)

Presentations

1. Anchoring of a dye precursor on p-type NiO(100) studied by RT nc-AFM. **Freund, S.**; Hinaut, A.; Marinakis, N; Constable, E. C.; Meyer, E.; Housecroft, C. E. and Glatzel, Th. *DPG Spring Meeting*, 2018–03–14, Berlin, Germany.
2. Etude nc-AFM d'îlots de C₆₀ formés sur un cristal moléculaire organique. **Freund, S.**; Hinaut, A.; Pawlak, R; Liu, S.-X.; Decurtins, S.; Meyer, E. and Glatzel, Th. *Forum des Microscopies à Sonde Locale*, 2016–03–23, Montbéliard, France
3. nc-AFM study of C₆₀ islands on organic compound crystals. **Freund, S.**; Hinaut, A.; Pawlak, R; Liu, S.-X.; Decurtins, S.; Meyer, E. and Glatzel, Th. *DPG Spring Meeting*, 2015–03–19, Berlin, Germany.

Posters

1. Standard dye molecules adsorbed on NiO(001) studied by non-contact atomic force microscopy. **Freund, S.**; Hinaut, A.; Marinakis, N; Constable, E. C.; Meyer, E.; Housecroft, C. E. and Glatzel, Th. *SAOG*, 2018–02–01, Fribourg, Switzerland.
2. Anchoring of a dye precursor on p-type NiO(100) studied by RT nc-AFM. **Freund, S.**; Hinaut, A.; Marinakis, N; Constable, E. C.; Meyer, E.; Housecroft, C. E. and Glatzel, Th. *Beilstein Nanotechnologie Symposium*, 2017–11–21, Potsdam, Germany.
3. Anchoring of a dye precursor on p-type NiO(100) studied by RT nc-AFM. **Freund, S.**; Hinaut, A.; Marinakis, N; Constable, E. C.; Meyer, E.; Housecroft, C. E. and Glatzel, Th. *QMol*, 2017–09–11, Ascona, Switzerland.
4. Etude nc-AFM a température ambiante de l'ancrage d'un précurseur de pigments photosensibles sur le semi-conducteur de type p NiO(100). **Freund, S.**; Hinaut, A.; Marinakis, N; Constable, E. C.; Meyer, E.; Housecroft, C. E. and Glatzel, Th. *Forum des Microscopies à Sonde Locale*, 2017–03–20, Montpellier, France.
5. Anchoring of a dye precursor on p-type NiO(100) studied by RT nc-AFM. **Freund, S.**; Hinaut, A.; Marinakis, N; Constable, E. C.; Meyer, E.; Housecroft, C. E. and Glatzel, Th. *SAOG*, 2017–01–27, Fribourg, Switzerland.
6. Force microscopy study of C₆₀ islands on organic compound crystals. **Freund, S.**; Hinaut, A.; Pawlak, R; Liu, S.-X.; Decurtins, S.; Meyer, E. and Glatzel, Th. *611. WE-Heraeus-Seminar: Mechanisms of Tribology*, 2016–03–29, Bad Honnef, Germany.
7. nc-AFM study of C₆₀ islands on organic compound crystals. **Freund, S.**; Hinaut, A.; Pawlak, R; Liu, S.-X.; Decurtins, S.; Meyer, E. and Glatzel, Th. *18th International Conference on non contact Atomic Force Microscopy*, 2015–09–09, Cassis, France.

8. Force microscopy study of C₆₀ islands on organic compound crystals. **Freund, S.**; Hinaut, A.; Pawlak, R; Liu, S.-X.; Decurtins, S.; Meyer, E. and Glatzel, Th. *The International Conference on Understanding and Controlling Nano and Mesoscale Friction*, 2015-06-24, Istanbul, Turkey.
9. nc-AFM study of C₆₀ islands on organic compound crystals. **Freund, S.**; Hinaut, A.; Pawlak, R; Liu, S.-X.; Decurtins, S.; Meyer, E. and Glatzel, Th. *5th European Nanomanipulation Workshop*, 2014-06-18, Basel/Mulhouse, Switzerland/France.

Curriculum Vitae

Name: Sara Freund

Date of birth: 24 October 1989

Place of birth: Mulhouse, France

Education

2014 – 2018	PhD in Experimental Physics, University of Basel, Switzerland
2011 – 2014	Master in Nanoscience, University of Basel, Switzerland
2007 – 2010	Bachelor in Physics, University of Strasbourg, France
2004 – 2007	Baccalauréat Scientifique, High school J. Mermoz, Saint-Louis, France
1995 – 2007	Primary and Secondary school, Hégenheim, France

Teaching

2015 – 2018	Supervision of “Schweizer Jugend Forscht”: <ul style="list-style-type: none">– “girls@science”– “boys@science”
2014 – 2018	Teaching assistant for practical works: <ul style="list-style-type: none">– “Blockkurs – Photovoltaics”– “Fortgeschrittenenpraktikum – Solar cells”

Awards

2016	Best Poster Prize, WE-Heraeus-Seminar: Mechanisms of Tribology, Bad Honnef, Germany
2015	Best Master Thesis SNI Award, University of Basel, Switzerland